University of Guilan
Department of Physics

Universiteit Antwerpen
Faculteit Wetenschappen
Departement Fysica

Investigation of the effects of defects and impurities on nanostructures consisting of Group IV and V elements using First-principles calculations

---

Studie van de effecten van defecten en onzuiverheden op nanostructuren bestaande uit Groep IV en V elementen met behulp van First-principles berekeningen

Thesis submitted to achieve the degree of doctor of science by

Asadollah Bafekry

Supervisors:
Prof.dr. Saber Farjami Shayesteh
University of Guilan, Iran
Prof. dr. François Peeters
University of Antwerpen, Antwerpen, Belgium

Academic year 2019-2020

May 2020

DEDICATION

I dedicate my thesis to God who has been my guide during all my life. My faith in Him always empowered me with the courage to help me cross each hurdle that I came across as I did this thesis.
Also, I dedicate my thesis to my girl Yara and my loving parents who have made me stronger, better and more fulfilled than I could have ever imagined.

Members of the Jury:

Chairman
Dr. Jamal Mazloom , University of Guilan, Iran

Supervisors
Prof.dr. Saber Farjami Shayesteh, University of Guilan, Iran
Prof.dr. François Peeters, Universiteit Antwerpen, Belgium

Members
Prof.dr. Saber Farjami Shayesteh, University of Guilan, Iran
Prof.dr. Mehdi Neek-amal, Shahid Rajaee University, Iran
Prof.dr. Saeed Mahdavifar, University of Guilan, Iran
Dr. Hanif Hadipour, University of Guilan, Iran

Contact Information

Asadollah Bafekry
G.U. 205
Groenenborgerlaan 171
2020 Antwerpen
Belgium
bafekry.asad@gmail.com

ACKNOWLEDGEMENT

I would like to express my deepest appreciation to my supervisors Prof. Saber Farjami Shayesteh and Prof. François Peeters for their guidance and continuous encouragement during my Ph.D study. I consider it an honor to be their Ph.D student. Besides my supervisors, I'd like to thank Prof. Catherine Stampfl as my collaborator.

Asadollah Bafekry
Rasht, May 2020.

Contents

List of Figures

List of Tables

CHAPTER 1

Introduction

Over the last decade, two-dimensional materials (2DM) have attracted great attention from the scientific community owing to their applications in electronic devices. The first ever realized 2DM is graphene and, since 2007, it has intensively been explored to electronic device applications, in particular, transistors. While graphene transistors are still on the agenda, researchers have extended their work to 2DM beyond graphene and the number of 2DM under examination has literally exploded recently. Meanwhile, several hundreds of different 2DM have been added to 2D library up to date, a substantial part of them has been considered to be suitable for nanoelectronics. The intention of the present thesis is to shed more light on the merits and drawbacks of 2DM for nanoelectronic applications and to add useful investigations to the ongoing discussion on the prospects of two-dimensional electronic.

2DM have been extensively studied owing to their novel properties and technologically important applications. Especially, the discovery of graphene has stimulated importance of investigations to exploit its novel properties for nanoscale applications. In the post-silicon era, graphene has been widely investigated as the most promising building blocks for the electronic devices. However, its semi-metallic nature is limited its scope for applications. Semiconductors are known to be essential for the applications in nano devices such as transistors. Such a limitation associated with graphene has led to the exploration of 2DM beyond graphene.

1.1 Two-dimensional material (2DM)

2DM, normally referred to as single atomic thin layer materials, have become a central topic of research interest since the exfoliation of graphene in 2004. [7] In contrast to their bulk structures, 2DM have surfaces which enable their energy band structures to be sensitive to external perturbations and functionalization. This all-surface nature of 2DM makes them competitive for devices as described by Herbert-Kroemer in The interface is the device. [8] Research on 2D material-based devices not only has contributed to a deeper understanding of the physics of these novel layered materials but also has provided a great platform for the potential opportunities in many fields ranging from electronics to optoelectronics and even to energy and sensing applications.

In 1959, Richard Feynman gave an inspiring and influential lecture entitled ˝There is Plenty of Room at the Bottom˝. [9] In his talk, Feynman envisioned a scientific breakthrough in the field of physics with his questions ˝What could we do with layered structures with just the right layers? What would the properties of materials be if we could really arrange the atoms the way we want them?˝ Those Questions challenged scientists to manipulate and control materials on the atomic scale. It was not until 2004, 45 years later, that the University of Manchester physicists Andre K. Geim, Konstantin S. Novoselov, and collaborators experimentally exfoliated and identified graphene, a 2D single atomic layer of carbon. The history of research on graphene, however, can be traced back much further. As early as 1947, Philip Wallace calculated the band structure of this one-atom-thick crystal. [10]

15 years later, Hanns-Peter Boehm synthesized graphene flakes through reductions of graphene oxide dispersions. [11] Then, material scientists tried to produce this one-layer graphite with exfoliation methods or thin-film growth technologies. [12–14] Indeed, graphene was officially defined to introduce this single atomic carbon layer of graphite structure by the International Union of Pure and Applied Chemistry in 1995. [15] Based on the earlier studies of ultrathin graphite, along with the rise of other carbon nanomaterials (such as fullerene and carbon nanotubes), [15–17] scientists and engineers devoted more interests and energy into this new fascinating material to discover its remarkable science and its potential for practical applications. In recent years, various 2DM beyond graphene have attracted considerable attention to the research community, including insulators [e.g., hexagonal boron nitride (h-BN) and transition metal oxides], topological insulators (e.g., Bi_2Te_3), semiconductors [e.g.,MoS_2, WSe_2, and black phosphorus (BP)], metals (e.g.,TiS_2), superconductors (e.g., $NbSe_2$), and charge density waves (e.g., 1T-TaS_2 at low temperatures) (see in Fig. 1.1).

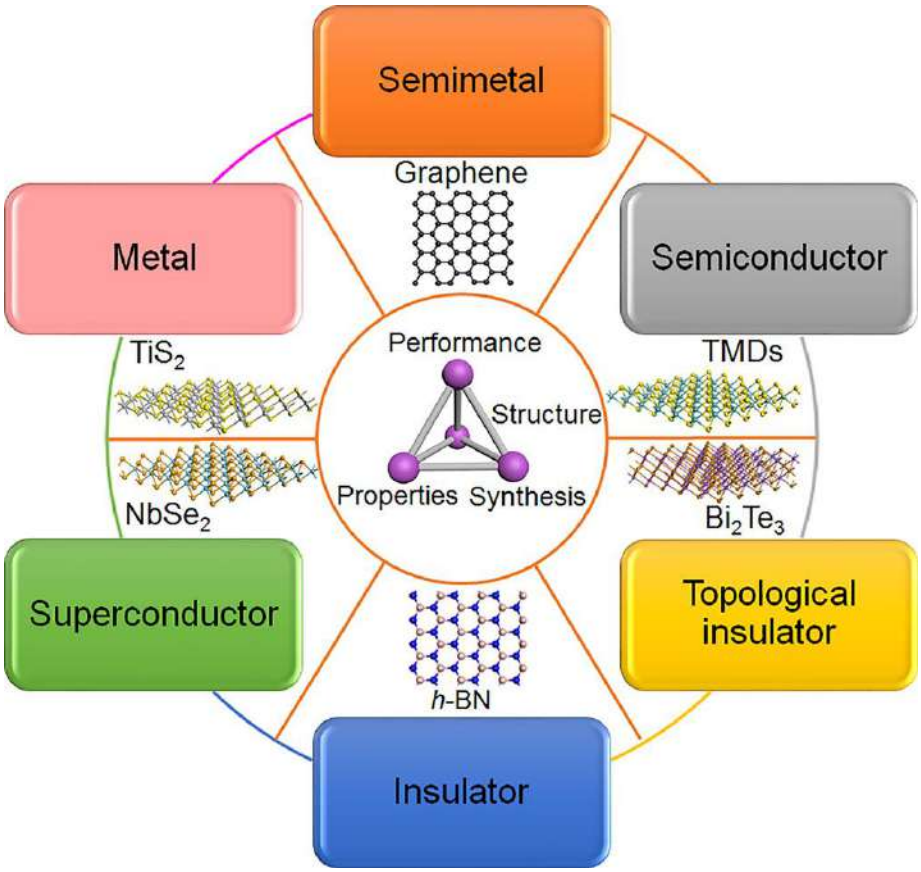

Figure 1.1: 2D material families. [1]

1.2 Crystal structures

The properties of materials are strongly affected by nanostructuring. For a better understanding, a brief introduction about crystalline structures of some typical 2D layered materials will be given in this part. There are more than 40 types of 2DM. [5, 18, 19]

On the basis of their chemical composition, those materials are divided into the following categories: TMDs in the form of MX_2 (M stands for transition metal, like Mo, W, Nb, Re, Ni and V, X stands for chalcogens, including S, Se and Te); TMCs with an MX stoichiometry (III-VI group, and IV-VI group compounds); layered insulator h-BN; single element materials like graphene, black phosphorus (BP), silicene and gemanene; V-VI group of topological insulators (TIs) as Bi_2Te_3, Sb_2Se_3 and Bi_2Se_3; transition metal oxides/hydroxides, such as MoO_3, V_2O_5, $Ni(OH)_2$ etc; as well as others (including metal-organic frames and mica etc).

TMDs have layered nature where the layers are weakly coupled while the atoms in the layer are covalently bonded. [5, 18–22] Variation in the stacking sequence along the out-of-plane direction leads to six different polytypes in bulk form. Among them, 1T (refers to trigonal) and 2H (refers to hexagonal) are usually the most stable states. In the 1T phase, metal atoms are octahedrally coordinated with six neighboring chalcogens, whereas the coordination in 2H is trigonal prismatic. [19] Fig. 1.2(a) shows the crystal structures of 1T and 2H type MoS_2 as an example. The studies on TMDs were date back to the 1970s. Up to now, comprehensive conclusions have been addressed. In general, the TMDs formed from groups IVB and VIB metals show semiconducting properties, whereas group VB exhibit metallic properties [23] Very similar structures were found for group III-VI group TMCs (MX, where M=Ga, In; X=S, Se). Fig. 1.2(b) gives the example of GaSe.

Unlike X-M-X layers in TMDs, hexagonal GaSe has a layered structure in which Se-Ga-Ga-Se atomic order is formed within the layer. According to the ab initio calculation method, one formula unit thickness of GaSe is about 0.75 nm. [24, 25] Unlike its analogues, GaTe has a relatively complicated structure which 1D-like anisotropic structure. As shown in Fig. 1.2(c), there are two kinds of Ga-Ga bonds: two-thirds are perpendicular to the layer and the others are parallel to the layer. As a consequence, a less symmetric monoclinic structure is induced.[26, 26] IV-VI group TMCs, including MX with M=Ge, Sn, Pb and X=S, Se, Te, have a distorted NaCl-type structure. Fig. 1.2(d) shows the crystal structure of GeS as an example the atoms are covalently bonded to three neighbors, forming armchair and zigzag conformations within a layer. Perpendicular to the layers direction, weak van der Waals forces link the layers together making up the 3D bulk materials .[27, 28]

Topological insulators (TIs) are materials with an insulating bulk state and a metallic state at the surface/edge. [29, 30] Holding this special property, TIs are promising for designing novel spintronic, electronic and optoelectronic devices. [31–33] Layered TIs, including Bi_2Te_3, Bi_2Se_3 and Sb_2Se_3, are of great interest for their large surface-to-volume ratio, which favors the manipulation of surface states. [34–37] All these layered TIs share the same structure, as shown in Fig. 1.2(e). Each layer consists of covalently bonded X (Se and Te)-M (Bi and Sb)-X-M-X sheets, and these quintuple layers (with a thickness of about 1 nm) are stacked together by the weak van der Waals forces. [38] Phosphorene is another single element layered material besides graphite (graphene). [39, 40] Its crystal structure is given in Fig. 1.2(f). In a layer, each phosphorous atom is covalently bonded with three neighbors forming a zigzag configuration. Weak van der Waals strength stacks each layer together to form a puckered honeycomb structure.

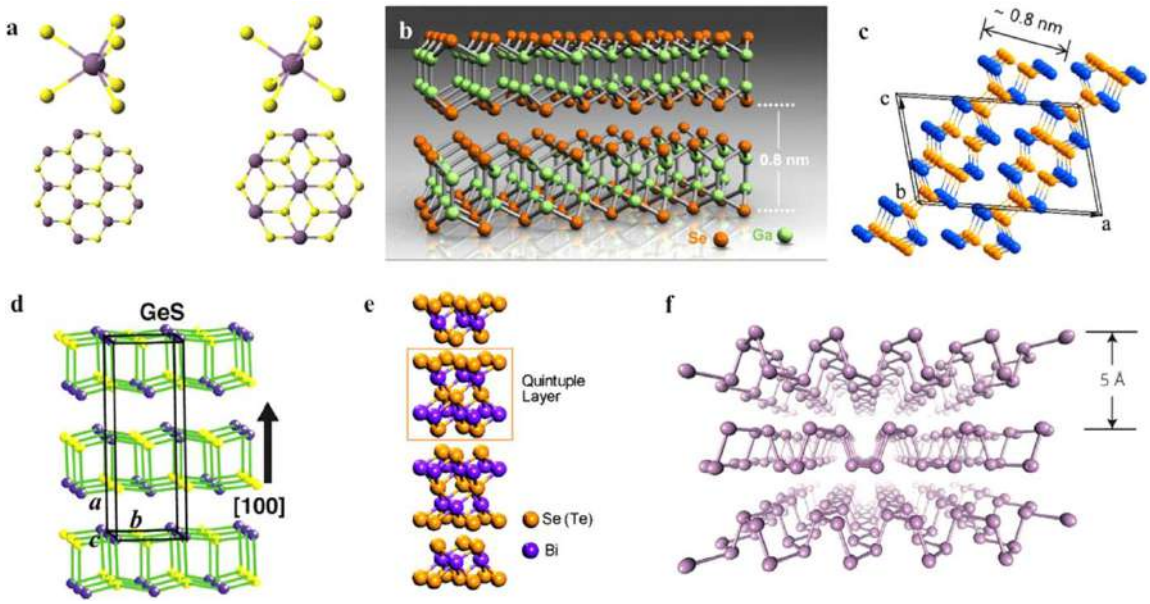

Figure 1.2: Atomic structures of 2D non-graphene materials. (a) 1T (right) and 2H (left) phases of MoS_2, respectively. In the upper diagram, the trigonal prismatic and octahedral coordination are shown. The lower panel shows the c-axis view of single-layer MoS_2. Atom colour: purple, Mo; yellow, S. (b) Two layers of GaSe, where the selenium and gallium atoms are represented by orange and green spheres, respectively. (c) Atomic structure of GaTe. Blue balls, Te; yellow balls, Ga. (d) Atomic lattice of GeS with a rhombohedra structure. (e) Atomic structures of Bi_2Se_3 and Bi_2Te_3. (f) Atomic structure of black phosphorus. [2]

1.3 Overview of 2DM

The successful isolation of graphene has intensively increased the attention to other stable 2DM. Not only experimental efforts but also theoretical predictions on the stability of novel 2DM have been widely done. For the latter, an Átlas of 2DM have been published including the prediction of more than 140 different 2DM. [3]

1.3.1 X-enes and X-anes

Single-layer crystals consisting of single elements, which are arranged in a honeycomb hexagonal lattice, are known as the single-layer X-enes. So far, graphene as well as its Si-, Ge-, and P-based counterparts silicene, germanene, and phosphorene [39, 41, 42] have been experimentally realized, and their properties have been investigated. [43] (see Fig. 1.3)

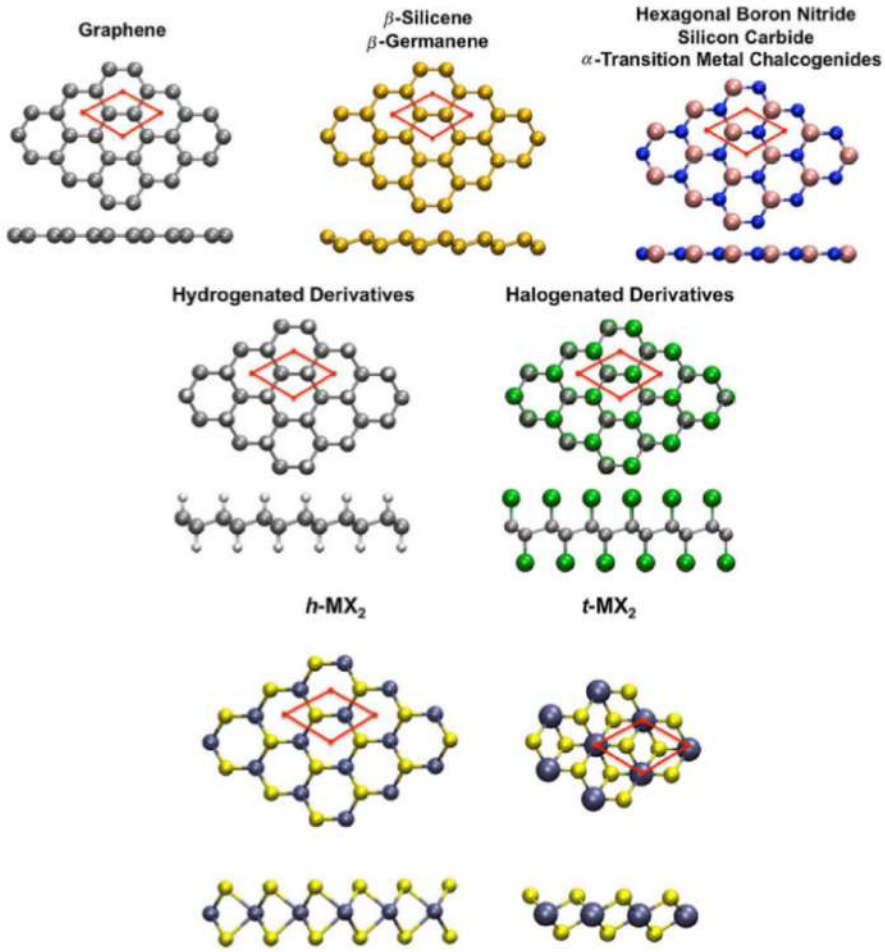

Figure 1.3: Structure of atomically thin 2D materials: graphene, silicene, germanene (and their derivatives), silicon carbide (SiC), hexagonal boron nitride (h-BN) and α-transition metal chalcogenides (TMC) (top). Ultrathin 2D materials such as transition metal dichalcogenides (TMD) (bottom). Unit cells are depicted in red. Colour code: Metals in ice blue, halides in green, chalcogenides in yellow, nitrogen in blue, carbon in grey, silicon and germanium in gold, boron in pink and hydrogen in white. [3]

The crystallographic structure of the X-anes, which are known as the hydrogenated structures of X-enes, is closely related to that of the X-enes. They also possess a hexagonal lattice of carbon (graphane), silicon (silicane), germanium (germanane), or tin (stanane) atoms. However, the lattice atoms are saturated by H atoms by the out-of-plane orbitals. Among them, graphane has been theoretically predicted[44] and then has been demonstrated to exist experimentally.[45] Recently, germanane has also been realized experi-

mentally.

Most relevant for electronic applications is the fact that graphane, silicane, and germanane possess sizeable band gaps. Here, the lattice atoms are now bonded to F atoms through the out-of-plane unoccupied orbitals. Fluorographene has already been produced experimentally and has been shown to exhibit a wide band gap, possibly even exceeding 3 eV. [46, 47] Theory has confirmed these results for fluorographene and furthermore has predicted a gap around 1 eV for fluorosilicene while fluorogermanene seems to be gapless .[3]

1.3.2 TMDs and SMCs

The transition metal dichalcogenides (TMDs) is an important group of 2DM which constitute a group of materials consisting of a transition metal M (elements of groups 4, 5, and 6 of the periodic table of elements) and a chalcogen X, i.e., sulfur (S), selenium (Se), or tellurium (Te) (see in Fig. 1.3). These M and X elements form covalently bonded 2D layers of the MX_2 type (e.g., MoS_2) with a hexagonal lattice. Single-layer TMDs consist of three atomic layers where the layer of M atoms is sandwiched between two layers of X atoms. Currently, more than 40 different types of TMDs have been either experimentally synthesized of theoretically predicted. Many of single-layer TMDs, i.e., MoS_2, WSe_2, and Hf-, Pd-, Pt-, and Zr-based TMDs, exhibit semiconducting behavior with band gaps of the order of 1-2 eV. [3, 21] Notably, TMDs can crystallize in different polytypes, namely 1T, 1Ť, 2H, and 3R, where T means trigonal, Ť distorted trigonal, H hexagonal, and R rhombohedral, and 1, 2, or 3 indicates the number of TMD layers in the unit cell.[48, 49] For example, while 2H polytypes are known to be semiconductors, their metastable counterparts, the 1T phases, are metals. [50]

1.3.3 MX-enes

There is a material class called the MAX family comprising more than 60 individual ternary layered materials (see Fig. 1.4). [51] These materials crystallize in a hexagonal lattice and have the composition $M_{n+1}AX_n$ where M is an early transition metal, A is a group 13 or 14 element, X is either carbon or nitrogen, and n is an integer equal to 1, 2, or 3. The bonds between the M and X atoms are much stronger than the M-A bonds so that the A atoms can easily be removed, e.g., by an acid treatment. By a subsequent sonication, single $M_{n+1}X_n$ layers, the so-called MX-enes, have been shown to be synthesized. As the first MX-ene, Ti_3C_2 has been successfully prepared from the MAX material Ti_3AlC_2, [52] soon followed by the experimental verification of five further MX-enes, [51] and the existence of even more MX-enes have been predicted. Furthermore, F_2, $(OH)_2$, and O_2 groups

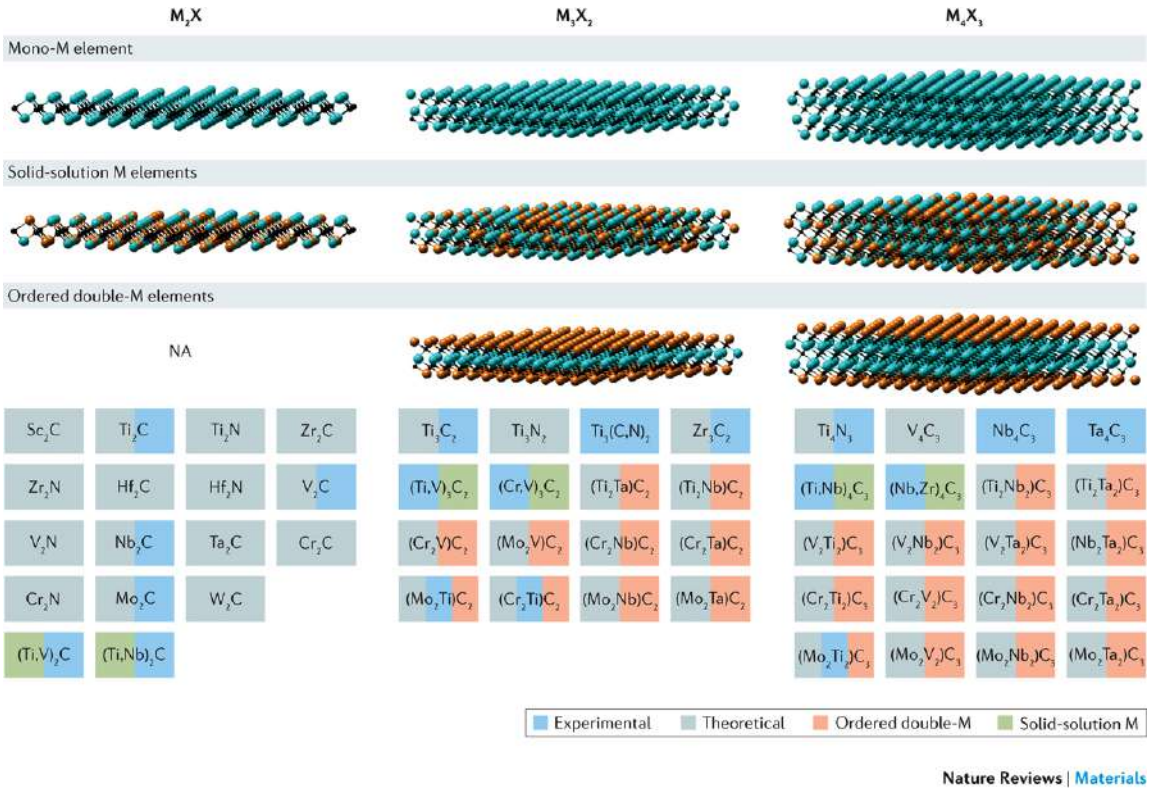

Figure 1.4: MXenes can have at least three different formulas: M_2X, M_3X_2 and M_4X_3, where M is an early transition metal and X is carbon and/or nitrogen. They can be made in three different forms: mono-M elements (for example, Ti_2C and Nb_4C_3); a solid solution of at least two different M elements (for example, $(Ti,V)_3C_2$ and $(Cr,V)_3C_2$); or ordered double-M elements, in which one transition metal occupies the perimeter layers and another fills the central M layers (for example, Mo_2TiC_2 and $Mo_2Ti_2C_3$, in which the outer M layers are Mo and the central M layers are Ti). Solid solutions on the X site produce carbonitrides. [4]

can attech to the pure MX-enes of the M_2X configuration, resulting in the formation of the modified MX-enes M_2XF_2, $M_2X(OH)_2$, and MXO_2. Several modified MX-enes have been predicted to be semiconductors with sizable band gaps. [53]

1.3.4 2D carbon nitride materials

Recently, a special class of 2DM, made from carbon and nitrogen atoms has attracted a lot of attention due to their outstanding physical and chemical properties. Layered nanomaterials solely composed of C and N atoms, with the ability of N atoms to take many different

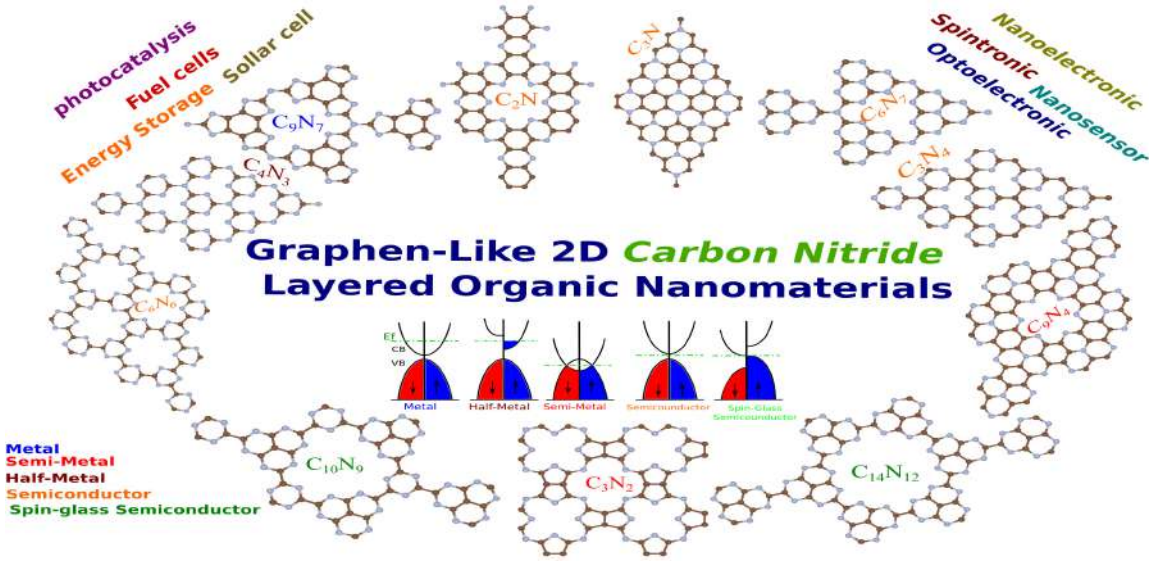

Figure 1.5: Schematic view of different carbon nitride nanosheets with their possible areas of applications. [4]

positions, enhance the possibilities to form strong covalent networks. These features allow to grow an extensive number of graphenic carbon-nitride lattices.

It is known that the strong C bonds give rise to the unique properties of graphene. Layered nanomaterials composed of C and N atoms with the ability of N to take many different positions, enhances the options to from strong covalent organic frameworks. These features allow to grow a number of graphenic carbon-nitride lattices. These two-dimensional carbon nitride (2DCN) show attractive band gap and surface-engineered applications in both energy- and environmental-related topics including photocatalysis for water splitting and hydrogen evolution. The strong C bonds give rise to the unique properties of graphene. Among the different classes of materials, 2D carbon nitrides (2DCN) have been among the most successful nanomaterials with inherent various different electronic character. Two-dimensional carbon nitride (2DCN) allotropes, show a common chemical formula C_nN_m, where n and m represent the number of C and N atoms in the primitive lattice, respectively.

2DCN nanomaterials are well-known to exhibit strong and stable components, owing to the formation of covalent bonds between the C-C and C-N bonds. For different compositions and configurations of the C and N atoms, these nanomaterials can exhibit diverse and promising electronic, optical, mechanical and thermal properties. 2DCN show attractive band gaps and offer surface engineering possibilities, and are well-known to have interesting application prospects in both energy- and environment-related topics, including catalysts, photocatalysis and hydrogen evolution. [54–58] A few decades ago, 2DCN with the

chemical formula C_3N_4, has been synthesized. [56] Unlike graphite, 2DCN show porous atomic lattices and more importantly are inherent semiconductors. [59] Very recently, 2D nitrogenated holey graphene with C_2N stoichiometry was experimentally fabricated via a wet-chemical reaction. [60] C_2N which contains an evenly distributed lattice of N and hole sites, makes it an excellent candidate as a nanofilter and an interesting structure for the adsorption of atoms and molecules [60, 61].

Recently, the first experimental realization of 2D polyaniline (PANI) with stoichiometric formula C_3N and a graphene-like structure is reported. [6] Theoretical studies showed that C_3N exhibits ultrahigh stiffness and thermal conductivity. [62] Furthermore, DFT calculations showed that the electronic properties of C_3N can be tuned by adsorption of atoms. [63] Like its C_2N counterparts, C_3N is also an intrinsic semiconductor according to recent theoretical studies. A C_3N nanosheet can show desirable properties for different applications, like; nanoelectronics, catalysis and hydrogen storage. [64–66] C_3N_4 showed semiconducting properties with the possibility to be a potential photo-catalyst for water splitting [67, 68]. This structure features intrinsic vacancies that are expected to produce a spin polarized state, while the electronic property of C_3N_4 will be drastically modified when atoms are substituted. The C_4N_3 is the counterpart of C_3N_4 that has been experimentally synthesized [69] and was identified to be half-metallic [70]. Metal-free magnetism and half-metallicity in C_4N_3 nanosheet and nanotubes [71–73] was recently predicted to be useful in spintronic devices. C_6N_6 is another 2DCN that has been explored in experiments [74, 75] and was investigated theoretically [76]. It was shown that C_6N_6 has topologically nontrivial electronic states and it can be tuned into a topological insulator by doping [77]. The successful synthesis and fabrication of different 2DCN motivated us to consider different approaches to tune the band gap [56, 60, 78]. Schematic view of 2DCN nanosheets including C_2N, C_3N, C_3N_2, C_3N_4, C_4N_3, C_6N_6, C_6N_8, C_9N_4, C_9N_7, $C_{10}N_9$ and $C_{14}N_{12}$ with its various possible applications, are shown in Fig. 1.5.

1.3.5 Further 2DM

By first-principles calculations, the phonon properties and band structures of entire classes of 2D IV-IV and III-V compounds and of many other 2DM have been investigated. It has been shown that a large body of these 2DM with both hexagonal and tetragonal lattice structures should be stable and show band gaps between 0.2 and 5 eV, respectively. [3, 79, 80] Although it is uncertain whether all these 2DM can be synthesized, at least part of them may become available for experiments in the future. More interestingly, these 2DM can be considered as Lego bricks. We can assemble these bricks together to design materials with completely different functionalities, known as van der Waals heterostructures as illustrated in Fig. 1.6.

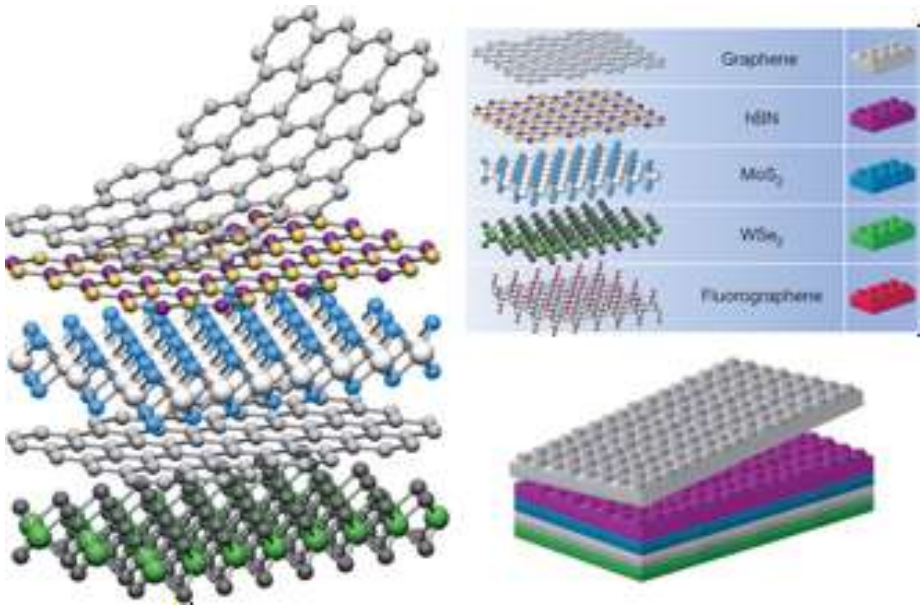

Figure 1.6: Building van der Waals heterostructures from 2D materials. [5]

1.4 Structural modifications of 2DM

In this part, we introduce the structural modifications of 2D layered materials. This modifications of structur, could strongly alter the physical properties of 2DM and affect the performance of their as electronic and magnetic devices. The structural modifications are such as different defects, dopants and impurities, thickness layers and strain, which are most important and play a key role in 2DM properties.

1.4.1 Defects

Defects in crystals is one of the most important structural properties of nanomaterials since it can modify their electronic and magnetic properties. For example, varipus defects can affect the electronic band structure, the thermal conductivity, and the mechanical propeties of 2DM. Most important lattice imperfections for 2DM are Point defects and line defects. These defects are generated at the synthesis process and chemical or physical post-treatment. [81, 82]

Stone-Wales defect. Stone-Wales type defect in graphene is formed such that two pentagons and two heptagons (55-77) occur due to rotation of two p-bonded carbon atoms by 90° (see Fig. 1.7(a)). [83] In Stone-Wales defect the total number of atoms remain the same and the defected structure does not involve any dangling bonds.

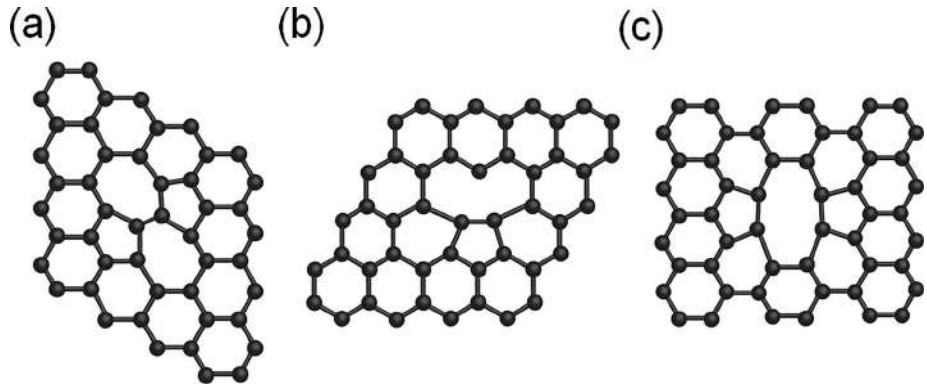

Figure 1.7: (a) Stone-Wales defect (55-77) in graphene. (b) Single vacancy defect (5-9) in graphene. (c) Double vacancy defect (5-8-5) in graphene. [1]

Vacancy defects. On the other hand, vacancy defects are created at the lattice sites where one or more atoms are missing. When an odd number of carbon atoms are missing in graphene, dangling bonds remain making the structure chemically active to many functional groups, such as hydroxyl and carboxyl. For instance, single vacancy in graphene results in the formation of a (5-9) defect (see Fig. 1.7(b)). [84]

Adatoms. In contrast to bulk crystals, interstitial defects are not thermodynamically favorable in 2DM due to prohibitively high energy in the single atomic plane structure. Instead, additional atoms tend towards the third dimension to form defects in 2DM. When the adatoms interact with a perfect carbon hexagon in graphene, physisorption or chemisorption occur depending on the adsorbed atom type.[85]

Substitutions. Foreign atoms can also be replaced with the intrinsic atoms in 2DM, leading to substitutional defects. Due to different atomic bond lengths, the substituted atom may optimize through the out-of-plane direction in the structure. [86] Importantly, the formed covalent bond is so strong that the substitutional impurities are considerably stable.

1.4.2 Dopants

Dopant atoms are desirable that they can adjust the Fermi-level and/or modify the electronic structure. Spatially controlled doping by ion implantation has been widely demonstrated in bulk semiconductors. However, alternative methods for doping of 2D materials should be considered since the ion implantation technique is difficult to be adopted in 2D systems. Substitutions and adatoms in 2DM are the two important defect engineering types over electrostatic doping. Substitutional doping of foreign atoms offers a control-

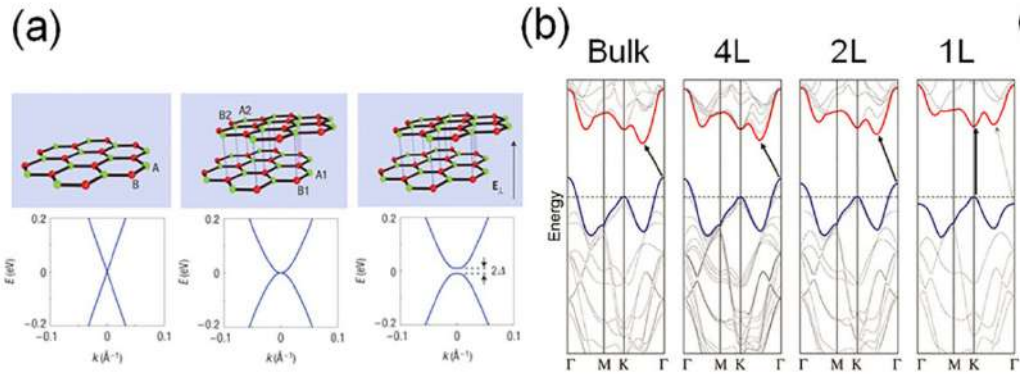

Figure 1.8: (a) Schematic diagrams of lattice structures and the corresponding band structures of monolayer graphene, bilayer graphene, and bilayer graphene under a vertical electrical field. The opened bandgap 2D can be tuned by the magnitude of the field. (b) Band structures of MoS_2 from the bulk to the monolayer (1L). The arrows show the transitions from valence band edge to the lowest energy conduction band edge. [1]

lable and stable doping method in 2DM. Typically, boron (B, called an acceptor), as a substitutional impurity atom replacing a carbon atom dopes graphene as p-type (hole is created in the valence band). Similarly, nitrogen (N) atoms (called a donor) are able to dope graphene as n-type (the electron is donated to the lattice in the conduction band). Another method for doping of 2DM has been achieved by the adsorption of inorganic or organic molecules on the surface. In general, adatoms, unlike substitution, do not disrupt strongly the electronic structure of graphene and the doping effect weakens or disappears if these molecules desorb from graphene. Similarly, molecules with electron donating groups lead to n-type graphene and molecules with electron accepting groups lead to p-type graphene. Alloying in 2DM can bring continuously tunable band gap by changing the composition, which is similar to bulk semiconductors. For example, graphene can be hybridized with separated-domain h-BN and this BNC alloy has tunable properties. [87] Moreover, the similar crystal structures and lattice constants between two different TMDs make the consequent 2D alloy materials chemically stable.

1.4.3 Number of layers

The band structure of a 2DM strongly depends on the number of layers because the vdW interaction plays a crucial role in the electronic properties of the 2D structure. For instance, in graphene, the energy dispersion near the Dirac point is linear, leading to its semimetallic features. However, the energy dispersion relation in the low-energy regime is parabolic

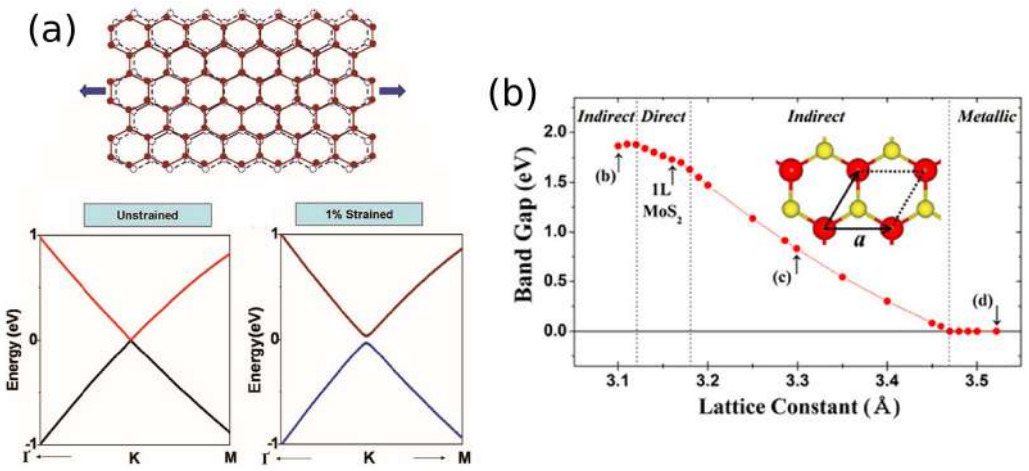

Figure 1.9: (a) Schematic of uniaxial tensile stress applied in graphene and the calculated band structure of 1% tensile strained graphene. An opened band gap can be clearly observed. (b) Band gap of monolayer MoS_2 as a function of applied strain. The direct band gap of pristine MoS_2 becomes indirect and even metallic when tensile strain is applied. [1]

due to interlayer coupling in bilayer graphene. [88] The band structure of TMD semiconductors are also highly dependent on the number of layers. Fig 1.8(b) shows the calculated band structure of representative MoS_2 with different number of layers from the bulk to the monolayer. [89]

1.4.4 Strain engineering

Strain engineering is an effective way to tune the electronic properties of semiconductors because energy band characteristics around the Fermi level are very sensitive to orbital coupling between neighboring atoms. 2DM have excellent elasticity which makes them suitable for strain engineering. [89, 90] Several ways have been demonstrated to introduce strain into 2DM : (1) Using a piezoelectric substrate to generate controllable biaxial strain by applying voltage between the sides of the substrate, which can be efficiently transferred to the 2DM. [91, 92] (2) Inducing controllable biaxial strain at a certain point of the 2DM by using an atomic force microscope tip. [90, 93] (3) Applying strain to 2DM via a patterned substrate. [94] Strain engineering offers an efficient and controllable way to open a band gap in graphene. The first-principles calculations have predicted that 1% of uniaxial strain creates a 300 meV band gap in graphene (see Fig 1.9(a)). [95] Strain-induced band gap engineering of 2D semiconductors is another interesting topic. Theoretical works have shown that compressive strain increases band gap while tensile strain results in a decrease

in the band gap in 2D TMD semiconductors. [96] Furthermore, a direct to indirect band gap transition in 2D TMDs can occur when strain is applied (see Fig 1.9(b)). [97]

1.5 Motivation of this thesis

In spite of the fact that 2DM hold great potential for a wide range of applications, for their real life applications, the tuning of their electronic properties are quite important. In recent years, several approaches have been developed for modifying the electronic and magnetic properties of 2DM. Defects are spontaneously generated during the growth of the 2D nanomaterials. It is well known that defects are difficult to avoid in materials especially in 2DM, which can dramatically affect the structure, its electronic and magnetic properties and the performance of 2DM-based devices. Defects are usually seen as detrimental to device performance. However they also can bring about new beneficial effects on the electronic structure and expand the potential applications of 2DM. Therefore, it is very important to understand the influence of these defects on their electronic and magnetic properties. Such understanding would also useful for controlling the defects. Recent advances in the fabrication of 2D carbon nitride (2DCN) structures have undoubtly enhanced the prospect for the experimental realization of novel nanosheets. In addition, the comprehensive insight provided by the extensive theoretical investigations have proven that 2DCN can serve as promising candidates for a wide range of applications.

The purpose of the present thesis is to investigate the structural, electronic and magnetic properties of nanostructures (nanosheet, nanoribbon and nanotube) of C_3N (polyaniline) by using first-principles calculations based on density functional theory (DFT). In Chapter 1, we introduce graphene and all kinds of two-dimensional materials, and discuss a variety of methods for modifying and adjusting the electronic and magnetic properties of two-dimensional materials and their properties and their applications. In the following, we give a brief overview of the density functional theory and the Kohn-Sham equations and computational code that will be used. In Chapter 2, we investigate the structural and electronic properties of C_3N nanosheet and examine the effects of adsorption of atoms and different molecules. Parameters calculated include adsorption energy and stable structure, charge analysis and others. In Chapter 3, we investigate the effects of chemical functionalization with hydrogen and oxygen atoms on C_3N nanosheet and examine their electronic properties. Here the effect of a variety of functionalization templates on the armchair and zigzag configuration are presented. At the end of this chapter, we will address the defects of hydrogen atoms in hydrogenated polyaniline nano-sheets. In Chapter 4, we study the band structure and density of polyaniline nanoparticles due to various defects and insertion of atomic impurities. In Chapter 5, we study the electronic properties of C_3N nanosheet

by changing the layers, applying electric field and mechanical strain.

1.6 Method of Calculations

1.6.1 Overview on Density Functional Theory

Density Functional Theory (DFT) [98]. is one of the most popular, powerful, versatile and successful quantum mechanical modeling methods used to investigate the electronic, magnetic, structural, and vibrational properties of materials. It was formulated by Hohenberg, Kohn, and Sham and aims to describe the ground state properties of many-electron systems in terms of the electronic charge density. Within this approach, the many body problem of interacting electrons in a static external potential is reduced such that one can tackle the problem by non-interacting electrons moving in an effective potential. It is being used for calculating the binding energy of molecules in chemistry and the electronic and phononic band structures of solids in physics. Since the past twenty years the success of DFT roots in the availability of accurate exchange-correlation functionals and sufficient computational resources. In this section, some of the basic ideas and practical methods related to DFT are introduced.

1.6.2 Formalism

A solid can be described as a collection of heavy positively charged particles (i.e., nuclei) and lighter negatively charged particles (i. e., electrons). Each nucleus has a charge Z.e, where Z is the atomic number and e is the electronic charge. A system with N nuclei thus leads to a problem of N+ZN interacting particles, which is a many body problem and demands a quantum mechanical approach. The many particle Hamiltonian for this system is

$$\hat{H}_{tot} = \hat{T}_e(\vec{r}_i) + \hat{T}_N(\vec{R}_\lambda) + \hat{V}_{ee}(\vec{r}_i, \vec{r}_j) + \hat{V}_{NN}(\vec{R}_\lambda, \vec{R}_\sigma) + \hat{V}_{eN}(\vec{r}_i, \vec{R}_\lambda), \qquad (1.1)$$

where $\hat{T}_e$ and $\hat{T}_N$ are the kinetic energy operators for the electrons and nuclei, respectively. The last three terms describe the electron-electron, nucleus-nucleus, and electron-nucleus Coulomb interactions. Computation of the energy and wavefunction of an average-size molecule is a formidable task that can be simplified by the Born-Oppenheimer approximation. [99] The nuclei are much heavier and therefore much slower than the electrons. As a result, the nuclei can be considered as effectively frozen at fixed positions, while the electrons are mobile. As a consequence, the kinetic energy of the nuclei is zero and the first term in equation (1.2) disappears. The potential term $\hat{V}_{NN}(\vec{R}_\lambda)$ also reduces to a constant and we are then left with the kinetic energy of the electrons, the potential energy due

to electron-electron interaction, and the potential energy of the electrons in the potential of the nuclei. Therefore, the Hamiltonian operator has only three terms: the kinetic energy of the electrons as well as the electron-electron ($\hat{V}_{ee}$) and the electron-nucleus interactions ($\hat{V}_{ext} = \hat{V}_{eN}$)

$$\hat{H}_{tot} = \hat{T}_e + \hat{V}_{ee} + \hat{V}_{ext} \tag{1.2}$$

These terms (in atomic units $m = \hbar = e^2 = 1$) are:

$$\hat{T}_e = -\frac{1}{2}\sum_{i=1} \nabla_i^2, \tag{1.3}$$

$$\hat{V}_{ee} = \frac{1}{2}\sum_{i\neq j} \frac{1}{|\vec{r}_i - \vec{r}_j|}, \tag{1.4}$$

$$\hat{V}_{ext} = -\sum_{i,j} \frac{Z_\lambda}{|\vec{r}_i - \vec{r}_\lambda|}, \tag{1.5}$$

Here $\vec{r}_i$ and $\vec{r}_j$ are the coordinates of electron i and j, respectively, and Z_λ is the charge of the nucleus at position R_λ. It is important to note that the kinetic and electron-electron terms depend only on the electron system. Information about the nuclei and their positions is entirely contained in $\hat{V}_{ext}$. The Hamiltonian within the Born-Oppenheimer approximation is much simpler than the original, but still far too difficult to solve. There are several methods to reduce equation (1.2) to an approximate but treatable form. A very important one is the Hartree-Fock method, which is used in quantum chemistry because it performs well for atoms and molecules. An alternative is DFT, which was established in 1964 and formulated in term of two theorems by Hohenberg and Kohn.

1.6.3 Hohenberg-Kohn Theorems

The conventional formulation of the two theorems of Hohenberg and Kohn is as follows [100]:

Theorem 1: The non-degenerate ground state electron density ρ_0 determines the external potential $\hat{V}_{ext}$. Thus the external potential is a well-defined functional of the ground state electron density $\hat{V}_{ext}[\rho_0]$.

Theorem 2: The ground state total energy functional $E_{\hat{V}_{ext}}[\rho_0]$ reaches its minimal value at the ground state electron density ρ_0 corresponding to $\hat{V}_{ext}$.

$$E[\rho] \geq E[\rho_0] \tag{1.6}$$

for every trial electron density ρ. The ground state total energy functional $E_{\hat{V}_{ext}}[\rho]$ can be written as

$$E_{V_{ext}}[\rho] = \langle\Psi(r)|\hat{T}_e + \hat{V}_{ee}|\Psi(r)\rangle + \langle\Psi(r)|\hat{V}_{ext}|\Psi(r)\rangle \tag{1.7}$$

$$= F_{HK}[\rho] + \int \rho V_{ext} d\vec{r} \tag{1.8}$$

where $F_{HK}[\rho]$ is universal for any many-electron system. We next explain the one-to-one correspondence $\rho \longleftrightarrow V_{ext}$, universality of $F_{HK}[\rho]$, and ground state total energy functional $E_{V_{ext}}[\rho]$.

First, the external potential correspond to a unique ground state many particle wave function, by the Schrodinger equation and the Hamiltonian given in equation (1.6). This wave function defines the corresponding electron density. Hence, an external potential gives a unique ground-state density corresponding to it. The first theorem of Hohenberg and Kohn demonstrates that the density contains as much information as the wave function. Thus, all observables can be written as a functional of the density, i.e., all their physical quantities can be recovered from the density only. From equation (1.7) one can see that $F_{HK}[\rho]$ does not contain any information on the nuclei and their position. Therefore, it is a universal functional for any many-electron system, implying that, in principle, there exists an expression for F_{HK} which can be used for every atom, molecule or solid. The ground state density corresponding to the external potential V_{ext} can be obtained by the second theorem only if an appropriate expression is known for $F_{HK}[\rho]$. The energy functional $E_{V_{ext}}[\rho]$ for the density ρ corresponding to the particular V_{ext} for any solid gives the ground state energy. For any other density ρ which is not the ground state density ρ, the energy will be higher, i.e. $E_{V_{ext}}[\rho] \geq E_{V_{ext}}[\rho]$.

1.6.4 The Kohn-Sham Equations

The Hohenberg-Kohn theorems show that it is possible to use the ground state density to calculate the physical properties of a system, but it does not tell us a way to find the ground state density. This difficulty is overcome by the Kohn-Sham equations [101]. The correlation energy is defined as part of the total energy absent in the Hartree-Fock solution. This motivates rewriting the total energy $E = T + V$ as

$$E_{V_{ext}}[\rho] = T_0[\rho] + V_H[\rho] + V_{xc}[\rho] + V_{ext}[\rho], \tag{1.9}$$

where T_0, V_H, and V_{xc} are the kinetic energy, Hartree potential, and exchange-correlation functional, respectively. The corresponding Hamiltonian is called the Kohn-Sham Hamiltonian $\hat{H}_{KS} = \hat{T}_0 + \hat{V}_H + \hat{V}_{xc} + \hat{V}_{ext}$. The exchange-correlation potential is given by

the functional derivative of the exact ground state density $\hat{V}_{xc} = \frac{\delta E_{xc}[\rho]}{\delta \rho}$. Finally, the Kohn-Sham equations can be written as:

$$H_{KS}\phi_i = \varepsilon_i \phi_i, \tag{1.10}$$

where the single particle wave functions ϕ_i fulfills $\sum_{i=1} \phi_i^* \phi_i = \rho$ and ε_i can be energy.The Kohn-Sham method is an exact description of the ground state properties of many-electron systems. However, the exchange-correlation functional is unknown and demands further approximations.

1.6.5 Exchange-Correlation Functional

The most widely used approximation to the exchange-correlation functional is the local density approximation (LDA). [100, 101] In this approximation the exchange-correlation energy is compared to the homogeneous electron gas,

$$E_{xc}^{LDA}[\rho] = \int \rho(\vec{r}) \varepsilon_{xc}^{hom}(\rho(\vec{r})) d^3 r, \tag{1.11}$$

where $\varepsilon_{xc}^{hom}(\rho(\vec{r}))$ is the exchange-correlation energy density. The many-electron system is divided into infinitesimally small regions located at positions $\vec{r}$, each containing a homogeneous interacting electron gas with a constant local density ρ. Particularly, the LDA is exact in the case of constant density, but (surprisingly) also works well in several realistic cases. Magnetic materials are modelled using the local spin density approximation, in which the electron density is divided into spin-up ($\rho \uparrow (\vec{r})$ and spin-down $\rho \downarrow (\vec{r})$) densities, with $\rho(\vec{r}) = \rho \uparrow (\vec{r}) + \rho \downarrow (\vec{r})$. Using the spin polarization $\zeta(\vec{r}) = \frac{\rho \uparrow (\vec{r}) + \rho \downarrow (\vec{r})}{\rho \uparrow (\vec{r}) + \rho \downarrow (\vec{r})}$ equation (1.10) takes the form

$$E_{xc}^{LDA}[\rho(\vec{r}), \zeta(\vec{r})] = \int \rho(\vec{r}) \varepsilon_{xc}^{hom}(\rho(\vec{r}), \zeta(\vec{r})) d^3 r \tag{1.12}$$

and the exchange-correlation functional becomes

$$V_{xc}[\rho(\vec{r}), \zeta(\vec{r})] = \frac{\delta E_{xc}^{LDA}[\rho(\vec{r}), \zeta(\vec{r})]}{/} \delta \rho(\vec{r}). \tag{1.13}$$

The LDA drastically fails for a rapid variation in the electron density, such as in molecules, at surfaces, and in strongly correlated electron systems. The well-known underestimation of the band gap in semiconductors and insulators, for example, results in a

major drawback as well as studying defects at semiconductor-oxide interfaces. To overcome this deficiency, various approximations have been proposed. Most widely used is the generalized gradient approximation (GGA) [102, 103], where the exchange-correlation functional depends on both the electron density and its gradient $|\nabla(\vec{r}))|$:

$$E_{xc}^{GGA}[\rho(\vec{r}), \zeta(\vec{r})] = \int \rho(\vec{r})\varepsilon_{xc}^{hom}(\rho(\vec{r}), \nabla(\vec{r}))d^3r, \tag{1.14}$$

$$E_{xc}^{GGA}[\rho\uparrow(\vec{r}) - \rho\downarrow(\vec{r})] = \int \rho(\vec{r})\varepsilon_{xc}(\rho\uparrow(\vec{r}), \rho\downarrow(\vec{r}), \nabla\rho\uparrow(\vec{r}), \nabla\rho\downarrow(\vec{r}))d^3r. \tag{1.15}$$

In many cases the GGA improves the total energy, structural parameters and binding energies of molecules. Many systems are not correctly described by both LDA and GGA, in particular strongly correlated systems. In these cases an extra parameter U, using the framework of the Hubbard model [104], can be added to the Hamiltonian. Resulting approximations are known LDA+U or GGA+U. In the recent years, hybrid functional methods are used for solids to accurately calculate band gaps, lattice parameters, bulk moduli, formation energies, and other related properties. However, hybrid functionals lead to huge computational demands.

CHAPTER 2

Adsorption of atom and molecule

2.1 Introduction

In spite of the fact that 2DM hold great potential for a wide usage of applications, it will be necessary to modulate their intrinsic properties to transfer them into real applications. In recent years, several approaches have been developed to modify the electronic and magnetic properties of 2DM. These methods involve substitutional doping, defect engineering, surface functionalization with adatoms, and application of an electric field. [105–110] From another perspective, the properties of 2DM can be modulated by strain engineering which does not involve any complicated chemical processing. [111, 112]

The adsorption of molecules is another important factor to affect the performance of nanosensors. Owing to the thin thickness and large surface-to-volume ratio, the electronic and magnetic properties of 2DM can be easily tuned by adsorbate molecules thus area should play an important role in sensing performance. Furthermore, the adsorption is an important and initial step in the activation of gas molecules. Detection of gas molecules is of great importance in both human health and environmental protection and the searching for suitable materials for gas sensing has important scientific significance [113, 114]. Types gas sensors may be useful for numerous applications, such as medical diagnosis, environmental monitoring and surveillance, agriculture production, military safety, emission control [114, 115]. The adsorption of molecules, has been extensively studied by first-principle calculations on graphene [116–121] and other 2DM [122–124].

Most recently, 2D polyaniline with stoichiometric formula C_3N and a graphene-like

structure in which nitrogen is uniformly distributed has been successfully synthesized. [6] C_3N is predicted to offer a variety of applications such as solar cell devices, electrolyte gating and doping of transistors and anode material. [125–127] The single layer C_3N, was first reported to be an indirect band-gap semiconductor and three possible planar structures were suggested. [128, 129] It exhibits ferromagnetic order at low temperatures when doped with hydrogen atoms. [130] The electronic structure of monolayer C_3N is give in Refs. [6, 128, 129, 131] Theoretical studies showed that C_3N exhibits ultrahigh stiffness and thermal conductivity. [62] Furthermore, DFT calculations showed that the electronic properties of C_3N can be tuned by adatom adsorption. [63, 64, 132, 133]

In this chapter we present an extensive analysis and consider adsorption of 27 adatoms such as, Al, alkali metal(AM) (Li, Na, K), alkaline earth metal (AEM) (Be, Mg and Ca) and 3d transition metal(TM) (Sc, Ti, V, Cr, Mn, Fe, Co, Ni, Cu and Zn) elements, and nonmetallic adatoms such as H, B, C, N, O, F, and P on the structural, electronic and magnetic properties of C_3N. Each adatom can be adsorbed at six most stable adsorption sites within a 2×2 supercell of C_3N. We found that H, O, S, F and Cl adatoms are adsorbed at stable T_C-site and B, C, Si, N, P and Cu preferentially at B_{CC}-site, while other adatoms at H_{CC}-site. In conclusion, while C_3N is a nonmagnetic semiconductor, its band gap can be modulated through adatom adsorption. In specific cases C_3N attains its magnetic properties and becomes metallic and the adsorbed adatoms give rise to donor or acceptor states in the band gap. Understanding the interaction between C3N and the adsorbate gas molecules, is important for to exploit the C3N gas sensors. In addition, to our best knowledge, gas sensing behavior, we have systemically investigated the adsorption of numerous gas molecules such as, atmospheric gas molecules (including H_2, O_2, CO_2 and H_2O) and common polluted gases (including CO, NO, NO_2, SO_2, H_2S, NH_3 and CH_4) on the C3N. These kinds of calculation results will help us to expand our understanding and could have practical interest in the difference applications such as gas sensors. Each molecule can adsorbed at difference configuration with multiple position and orientation as for these surfaces.

2.2 Computational method

We choose the OpenMX code [134, 135] for our calculations which is one of the fastest DFT codes. It can quickly perform structural optimization of molecular structures using atomic orbital basis (PAO) sets and pseudopotential method, which can simulate a wide range of properties of crystals and surfaces of materials such as semiconductors, ceramics, metals and minerals. In this paper, we performed first-principles total energy and electronic structure calculations, within the Perdew-Burke-Ernzerhof variant of the

generalized gradient approximation (PBE-GGA)[136] method, to deal with the exchange-correlation functionals. We used norm-conserving pseudopotentials [137], for carbon, nitrogen and adatoms. The wave functions are expanded in a linear combination of multiple pseudoatomic orbitals (LCPAOs) generated by using a confinement scheme [134, 135]. In the first step, the atomic structure positions in the C_3N and Ad/C_3N are optimized using OpenMX, which implements a quasi-Newton algorithm for atomic force relaxation. The geometries were fully relaxed with force convergence acting on each atom less than 1 meV/Å. The **k**-points for sampling over the Brillouin zone (BZ) integration were generated using the Monkhorst-Pack scheme [138]. For a primitive cell of hexagonal C_3N, a k-mesh grid of $15 \times 15 \times 1$ was used. After the convergence tests in OpenMX, we chose cutoffs of 250 Ry for C_3N, so that the total-energies converge below 1.0 meV/atom. With these parameters the resulting structures are found to be sufficiently relaxed to obtain various properties in the next steps of the calculation. The charge transfer was calculated using the Mulliken charge analysis [139].

Furthermore, we used the PW basis set with QUANTUM ESPRESSO [140] code, with kinetic energy cutoffs of 40 Ry and 320 Ry for the wave-functions and charge densities, with convergence in the total energy below 1.0 meV/atom. All atomic positions and lattice constants are optimized by using the conjugate gradient method, where the total energy and atomic forces are minimized. The convergence for total energy difference is less than 10^{-6} Ry between two steps, and the maximum force allowed on each atom is less than 10^{-3} a.u. between subsequent iterations. The Brillouin zone (BZ) is sampled by K-mesh grid of $23 \times 23 \times 1$ for primitive unit cell and scaled according to the size of the supercells. The large difference in the numbers of k-points in the PW and PAO basis sets is due to the different symmetrization treatments in the programs.

In addition calculations within SIESTA code [141] are performed where the eigenstates of the Kohn-Sham Hamiltonian are expressed as linear combinations of numerical atomic orbitals. A 200 Ry mesh cut-off is chosen and the self-consistent calculations are performed with a mixing rate of 0.1. Core electrons are replaced by norm-conserving, nonlocal Troullier-Martins pseudopotential. The convergence criterion for the density matrix is taken as 10^{-4} Ry. The C_3N are modeled as a periodic slab with a sufficiently large vacuum layer (20 Å) in order to avoid interaction between adjacent layers. In order to accurately describe the vdW interaction in the C_3N, we adopted the empirical correction method presented by Grimme (DFT-D2), which had been proven reliable for describing the long-range vdW interactions. [142]

In order to reveal whether the adsorbed adatoms can diffuse or migrate, we investigate the energy barriers for the displacement of the adatoms. The barrier is estimated through the Nudged Elastic Band (NEB) method [143]. In short, the NEB method allows for the determination of a minimum energy path (MEP) for the reaction pathway between two

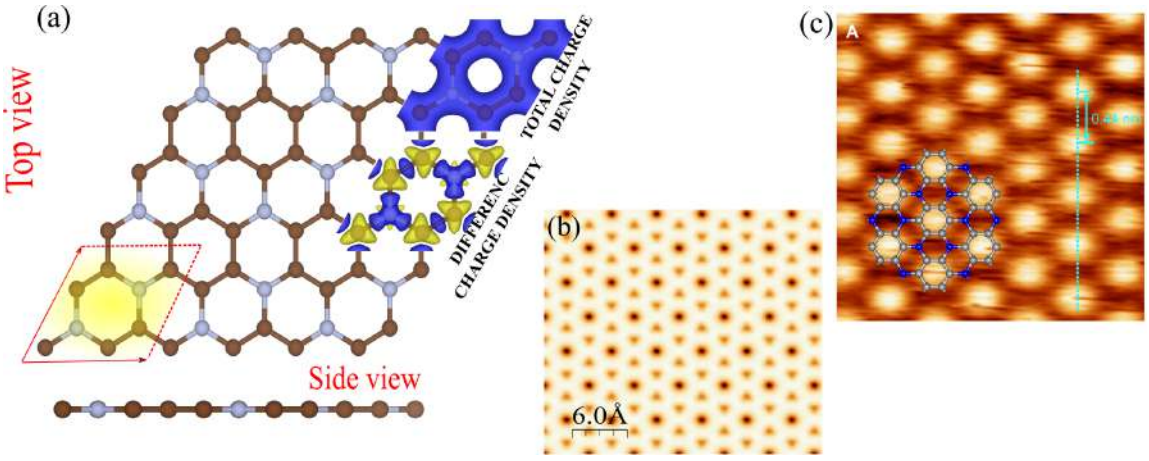

Figure 2.1: (a) Optimized atomic structure of C_3N, with its hexagonal primitive unit cell, indicated by a red parallelogram. The blue (brown) dots are N (C) atoms. The total and difference charge density isosurfaces are also shown in the same panel. (b) Simulated STM image and (b) STM image of C_3N structure. [6] Inset structure represents C_3N repeating unit cell.

optimized structures by the use of images connected by fictitious springs. Simulated scanning tunneling microscopy (STM) images were obtained using the Tersoff-Hamann theory [144] for STM images, as supplied with OpenMX code. The STM simulated images are given for bias of +2.0 V (unoccupied states) and were graphed using WSxM software [145].

2.3 Structure and electronic properties of monolayer C_3N

The honeycomb atomic structure of C_3N is a planar lattice which contains eight atoms (6 C and 2 N atoms) and can be regarded as a 2×2 supercell of graphene with two C substituted by two N atoms, as shown in Fig. 2.1(a). The optimized lattice constant of C_3N is 4.861 Å, which agrees well with the experimental value of 4.75 Å [6] and the C-C(d_{CC}) and C-N (d_{NC}) bond lengths are, 1.404 and 1.403 Å respectively, which agrees with previous theoretical calculations [62, 63, 128, 132]. The total and difference charge densities are shown in Fig. 2.1(a). Notice that a high charge density is found around the N atoms. The difference charge density is calculated by subtracting the charge densities of free C and N atoms from the charge density of C_3N. The high charge density around N atoms indicate a charge transfer from C to N atoms. The C-N bonds have covalent bond character. Bader charge was analysis performed with the QUANTUM ESPRESSO code. Our result shows that for C_3, each N atom gains about 0.6 electrons from the adjacent C

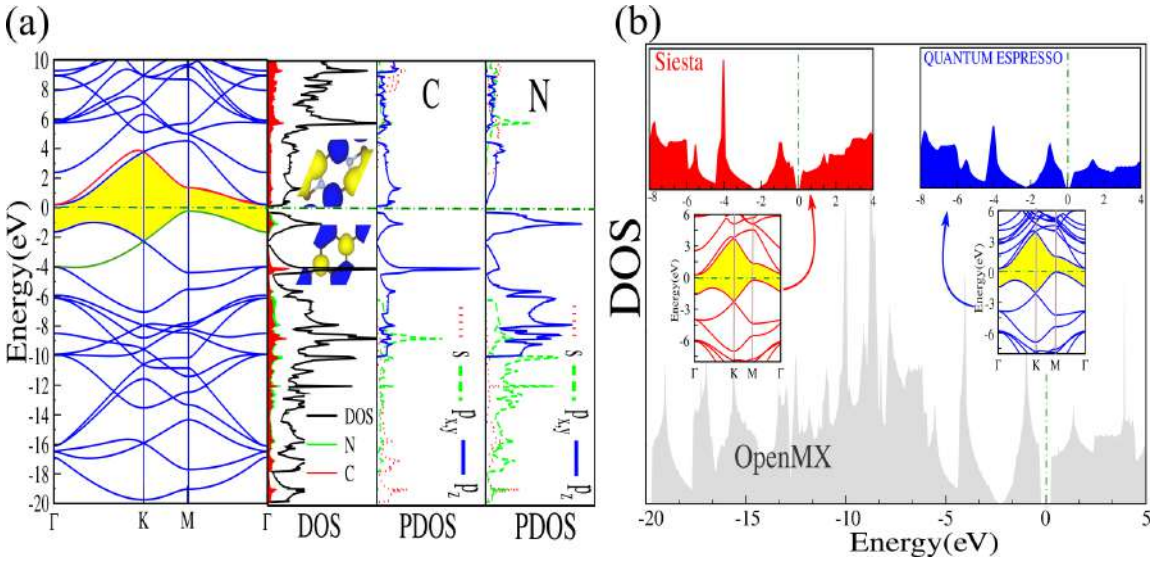

Figure 2.2: (a) Electronic band structure of C_3N with corresponding DOS and PDOS on C and N atoms. The zero of energy is set to the Fermi level (E_F). (b) The DOS and band structure (insets) of C_3N calculated with OpenMX, QUANTUM ESPRESSO and SIESTA codes.

atoms. The charge redistributions are due to the different electro-negativities of the atoms 2.0 (C) and 3.0 (N). First-principles DFT method was used to calculate the STM image which we show in Fig. 2.1(b). To produce the calculated STM image, the Kohn-Sham charge density was integrated from the Fermi level to 2 eV below the E_F. Inset structure represents C_3N repeating unit cell with carbon atom (gray ball) and nitrogen atom (blue ball). The STM image of C_3N structure is shown in Fig. 2.1(c) [6].

The electronic band structure, DOS and PDOS of C_3N, are shown in Fig. 2.2(a). The present GGA-PBE calculations demonstrate that C_3N is an indirect semiconductor with 0.4 eV band gap between the valence band maximum (VBM) at M point and the conduction band minimum (CBM) at Γ point. Our calculated gap value using GGA-PBE functional is in good agreement with previous results [6, 129, 131]. The energy band gap between CB and VB are dominated by the orbital character of C/N-p_z states as shown in Fig. 2.2(a), with red and green curves near E_F. Since in C_3N two C atoms are replaced by N, the p_z orbital band is fully occupied by the additional two electrons. In addition the higher electro-negativities and smaller atomic size of N as compared with C, result in a shorter partially covalent C-N bond. This leads to semiconducting behavior with band gap between the p_z states forming a Dirac-point, which is 2.25 eV below E_F. The DOS and PDOS of the C_3N, are similar to those of C_3N presented in Fig. 2.2(a). In addition the density of state (DOS) and Partial DOS were calculated using Gaussian smearing with

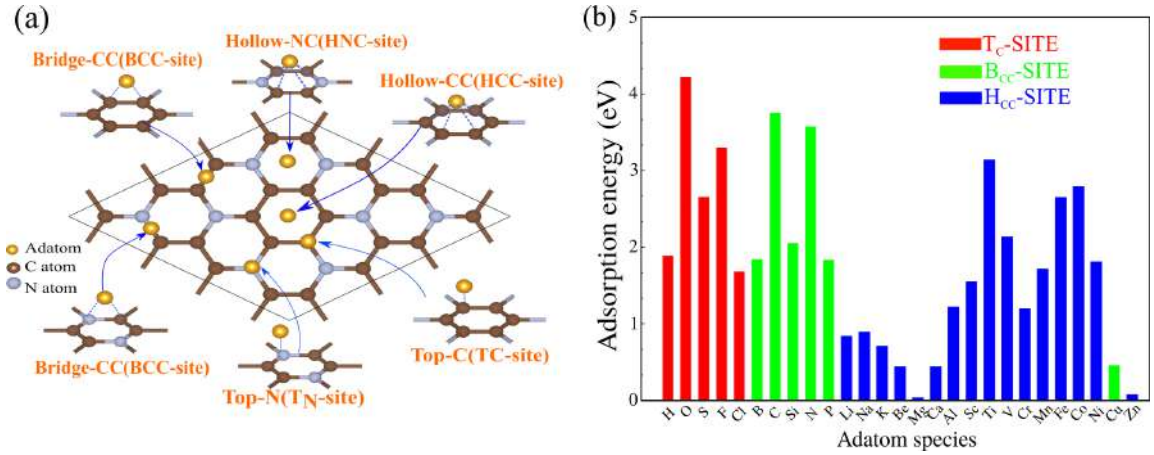

Figure 2.3: (a) Schematic view of possible adsorption sites of adatoms on C_3N. (b) Adsorption energy of different atoms on C_3N.

a width of 0.2 eV. From PDOS, we see that the VBM of C_3N is dominated by the N-p_z orbitals and the Dirac-Point is formed by N-p_z orbitals, whereas the CBM is prominent by C-p_z orbital states. The s-orbital states have a flat band and reflect heavy charge carriers. The C/N-p_z orbitals, open a gap in the C_3N as bonding and antibonding combinations.

The DOS and band structure calculations of pristine C_3N calculated with QUANTUM ESPRESSO (plane-wave basis set) [140] and SIESTA (atomic orbitals basis set)[141], are shown in Fig. 2(b). The unit cell parameters are the same for both cases. The plane-wave basis set takes two orders of magnitude more calculation time as compared to the atomic orbital basis set calculation. One can see from Fig. 2.2(b), that C_3N VB are identical and it is a semiconductor with an indirect band gap of ~ 0.4 eV using QUANTUM ESPRESSO and SIESTA, and is very similar to the OpenMX results.

2.4 Effect of adatom adsorption

Adsorption of adatom will affect the structural, electronic and magnetic properties of pristine C_3N. The minimum energy or most stable sites of various adsorbed adatom are obtained by placing the adatom to six prefable adsorption sites at an initiate height of ~ 2 Å from the surface of C_3N as schematically illustrated in Fig. 2.3(a). With fully structural optimizations, where all atoms are relaxed in all directions, we determine the most stable site as the minimum energy configuration among the six different sites. Calculations are performed using 2×2 supercell of C_3N. These six possible adsorption sites are; (1) the hollow site above the center of a hexagon with six C atoms (H_{CC}), (2) the hollow site

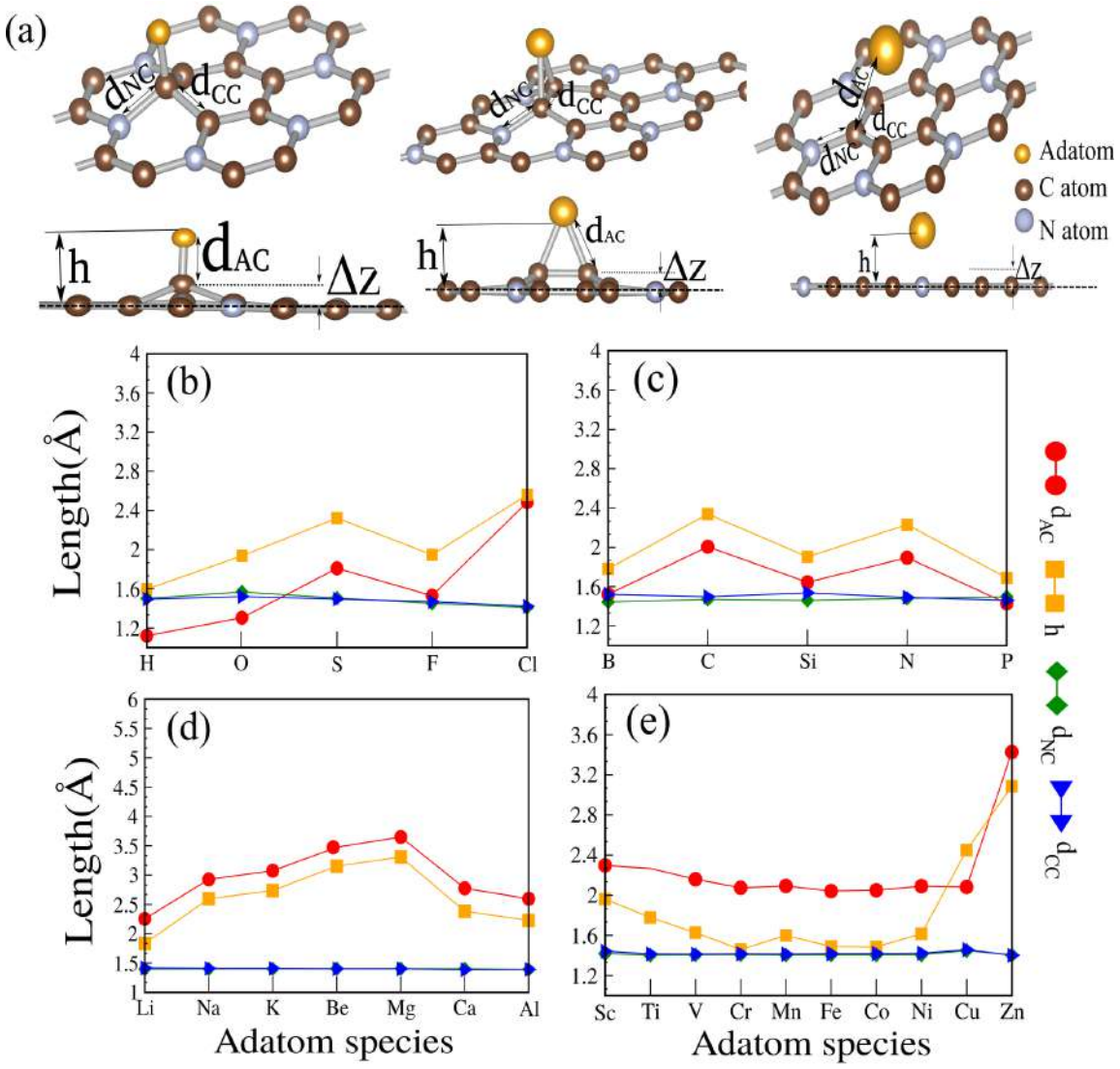

Figure 2.4: (a) Variation of structural parameters including bond lengths, height and buckling for different adatoms adsorbed on C_3N at the stable sites.

above the center of a hexagon composed of both C and N atoms (H_{NC}), (3) the bridge site above the middle of a C-C bond (B_{CC}), (4) the bridge site above the middle of a N-C bond (B_{NC}), (5) the top site above a C atom (T_C), and (6) the top site above a N atom (T_N) (see Fig. 2.3(a)). The adsorption energy for adatoms on C_3N is defined as

$E_a = E_{C_3N} + E_{Ad} - E_{Ad/C_3N}$, where E_{Ad/C_3N} is the total energy of the structure with adatom adsorption on C_3N, E_{C_3N} is total energy of pristine C_3N without adatom, and E_{Ad} is the total energy of an isolated adatom in vacuum. A positive value of the adsorption energy indicates that the adsorption of adatom to C_3N is favorable for a given geometry. The variation of adatoms adsorption energy adsorbed on C_3N, is shown in Fig. 2.3(b). Variation of structural parameters including bond lengths, height and buckling for different adatoms adsorbed on C_3N at the stable sites, are shown in Fig. 2.4.

The structural, electronic and magnetic parameters of Ad/C_3N at the stable adsorption sites involving the T_C, B_{CC} and H_{CC} sites are summarized in Table I. We present also the corresponding structural, electronic and magnetic parameters including bond length between adatom and its nearest atom (d_{AC}); the bond length between C-C atoms (d_{CC}); the bond length between N-C atoms (d_{NC}); the height of adatom from the C_3N plane(h); the buckling of C_3N defined by the difference between the largest and smallest Z coordinates of C atoms in C_3N (Δz); the adsorption energy of adatom, (E_a) and the magnetic moment per supercell (μ). The electronic state is specified as metal (M), half-metal (HM) or semiconductor (SC). The band gap of the system after adsorption (E_g); the charge transfer (ΔQ) between adatoms and C_3N are listed in Table I. The adsorption energy at stable T_C-site, is significantly larger with value in the range $E_a \sim 1.5 - 4.2eV$ with smaller $d_{AC} \sim$ 1.1-2.4 Å. While at stable B_{CC}-site, B, C, Si, N, P and Cu adatoms, possess adsorption energies in the range $\sim$ 1.8-3.7 eV with smaller $d_{AC} \sim$ 1.4-2.0 Å. The adsorption energy of Al, AMs (Li, Na and K) and AEMs (Be, Mg and Ca) adatoms at stable H_{CC}-site, in the range of 0.037 eV-0.89 eV and have a larger d_{AC}= 2.2-3.6 Å. For TM adatoms, the adsorption energy is larger than for Al, AM, AEMs and $d_{AC} \sim$ 2-3.5 Å. In the situation that the d_{AC} is long, the E_a tends to decrease and the adatoms show physical adsorption. In contrast, when d_{AC} is short, the E_a tends to increase and the adatom exhibit chemical adsorption. We found that adatom species at stable T_C and B_{CC} sites, causes the C atom to move out of plane and this geometrical transformation changes the structural parameters. The adsorption of adatom at stable T_C and B_{CC} sites, can result in considerable lattice deformations due to the relative stronger interaction between adatom and C_3N. Thus a buckling of $\Delta z \sim$ 0.5 Å of C_3N is occurs; the d_{CC} and d_{NC} with its first neighborâĂŹs are elongated to $\sim$ 1.50 Å, which compares with 1.40 Å for C_3N.

2.4.1 Adsorption of simple adatoms

The optimized atomic structures with corresponding, difference charge density of the C_3N with H, O, S, F, Cl, B, C, Si, N and P adatoms at stable sites is shown in Fig. 2.5. Now we study the effects of adatoms adsorbed to C_3N at stable T_C-site on electronic and magnetic properties by calculating band structure, DOS and PDOS (see Fig. 2.6). Here the anal-

Table 2.1: The structural, electronic and magnetic parameters of Ad/C_3N at the stable adsorption T_C, B_{CC} and H_{CC} adsorption sites shown in Fig. 3(a); The corresponding structural, electronic and magnetic parameters including bond length between adatom and its nearest atom (d_{AC}); the bond length between C-C atoms (d_{CC}); the bond length between N-C atoms (d_{NC}); the height of adatom from the C_3N plane(h); the buckling of C_3N defined by difference between the largest and smallest Z coordinates of C atoms in C_3N (ΔZ); the adsorption energy of adatom, (E_a); the magnetic moment per supercell (μ). Electronic states is specified as metal (M), half-metal (HM) or semiconductor (SC). The band gap the system after adsorption (E_g); the charge transfer (ΔQ) between adatoms and C_3N are also listed.

adatom	Site	E_a (eV)	d_{AC} (Å)	h (Å)	d_{NC} (Å)	d_{CC} (Å)	ΔZ (Å)	ΔQ (e)	$M_{tot}(\mu_B)$	E_g (eV)
H	T_C	1.891	1.121	1.597	1.503	1.495	0.509	0.02	0	M
O	T_C	4.22	1.305	1.937	1.569	1.522	0.640	-1.98	0	M
S	T_C	2.654	1.809	2.322	1.506	1.496	0.517	-0.73	0	M
F	T_C	3.297	1.530	1.948	1.452	1.469	0.439	-0.95	0	M
Cl	T_C	1.685	2.485	2.559	1.410	1.422	0.083	-0.37	0	M
B	B_{CC}	1.846	1.644	1.904	1.460	1.537	0.464	-1.15	0	M
C	B_{CC}	3.756	1.522	1.781	1.444	1.522	0.469	+0.23	0	M
Si	B_{CC}	2.054	2.006	2.339	1.470	1.498	0.479	+1.13	0	M
N	B_{CC}	3.575	1.430	1.690	1.497	1.461	0.469	-1.24	0	M
P	B_{CC}	1.836	1.895	2.230	1.481	1.491	0.493	+1.46	0	M
Li	H_{CC}	0.837	2.254	1.834	1.396	1.417	0.059	+0.95	0	M
Na	H_{CC}	0.89	2.927	2.597	1.400	1.409	0.031	+0.88	0	M
K	H_{CC}	0.71	3.074	2.737	1.401	1.409	0.004	+0.74	0	M
Be	H_{CC}	0.44	3.476	3.153	1.403	1.402	-0.027	+0.01	0	SC(0.43)
Mg	H_{CC}	0.037	3.650	3.309	1.404	1.402	-0.061	+0.23	0	SC(0.43)
Ca	H_{CC}	0.44	2.774	2.384	1.402	1.385	-0.008	+0.92	0	M
Al	H_{CC}	1.219	2.596	2.227	1.391	1.391	0.052	+1.34	0	SC(0.16)
Sc	H_{CC}	1.551	2.297	1.961	1.418	1.442	0.156	+1.12	1.10	M
Ti	H_{CC}	3.137	2.267	1.778	1.403	1.415	0.007	+0.98	2.56	M
V	H_{CC}	2.136	2.159	1.627	1.407	1.412	-0.005	+0.99	1.97	M
Cr	H_{CC}	1.201	2.074	1.459	1.408	1.416	-0.093	+0.76	0.00	SC(0.44)
Mn	H_{CC}	1.714	2.092	1.599	1.405	1.413	0.058	+0.55	3.50	M
Fe	H_{CC}	2.647	2.042	1.489	1.406	1.417	0.020	+0.73	2.00	SC(0.35)
Co	H_{CC}	2.790	2.050	1.485	1.406	1.419	0.008	+0.64	1	HM
Ni	H_{CC}	1.808	2.090	1.616	1.407	1.422	0.085	+0.59	0.00	SC(0.46)
Cu	B_{CC}	0.457	2.082	2.450	1.449	1.457	0.369	+0.05	0.09	M
Zn	H_{CC}	0.079	3.427	3.085	1.404	1.402	-0.042	+0.03	0.00	SC(0.4)

ysis of new states appearing around E_F is essential for a better insight of the electronic band structure. We found that the energy band dispersion of pristine C_3N with adsorption of adatom at stable T_C-site is strongly modified by the adatoms. The bonding between adatom and C_3N is covalent. The energy bands below and above E_F are mainly due to the adatom orbital states and appear as localized impurity states. The shape of Dirac-point in pristine C_3N and Ad/C_3N are shown in Fig. 2.6(a). In comparison with pristine C_3N, the shape of Dirac-point is greatly changed due to the strong disturbance of p_z states caused by the adatom. This illustrates that the interaction between adatom and C_3N may be determined by adatom p_z-orbital states rather than s states. From the DOS and PDOS shown in Fig. 2.6(b), we can see that the VBM of Ad/C_3N is due to the hybridization of s and $p_{x,y}$-adatoms as well as p_z-orbitals of the nearest C and N atoms. The main contribution to VBM comes from, for example H-s, O-$p_{x,y}$ and C and N-p_z orbitals hybridization, whereas p_z-orbital of O, S adatoms does not mix with surrounding C and N states. The CBM of both O and S is formed by hybridization of $p_{x,y}$ with $p_{x,y,z}$ orbital states of C_3N. The interaction of adatoms with C_3N induces metallic and semiconducting properties. For adatoms at stable T_C-site, the H and Cl/C_3N becomes a metal and the O, S, F/C_3N becomes a semiconductor with $E_g \sim$ 60-90 meV. As they mostly provide a p-type charge carrier by moving the E_F to the VB edge. We found that the Ad/C_3N at stable T_C-site exhibits a nonmagnetic ground state (see Table I).

Figs. 2.7(a,b) show the energy band structure with corresponding DOS and PDOS for

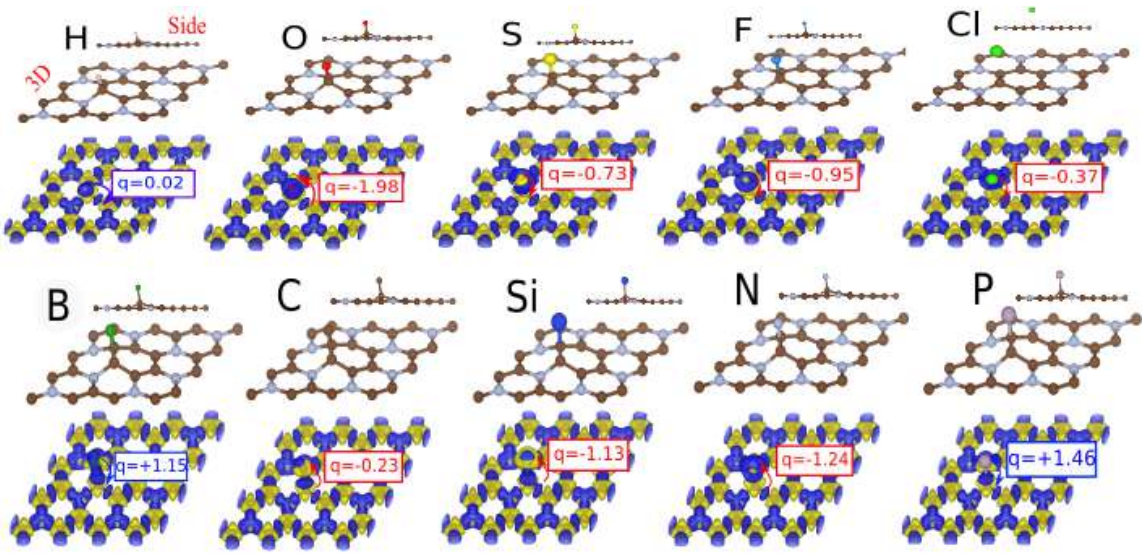

Figure 2.5: (a) Optimized atomic structures with corresponding, difference charge density of the C_3N with H, O, S, F, Cl, B, C, Si, N and P adatoms at stable sites.

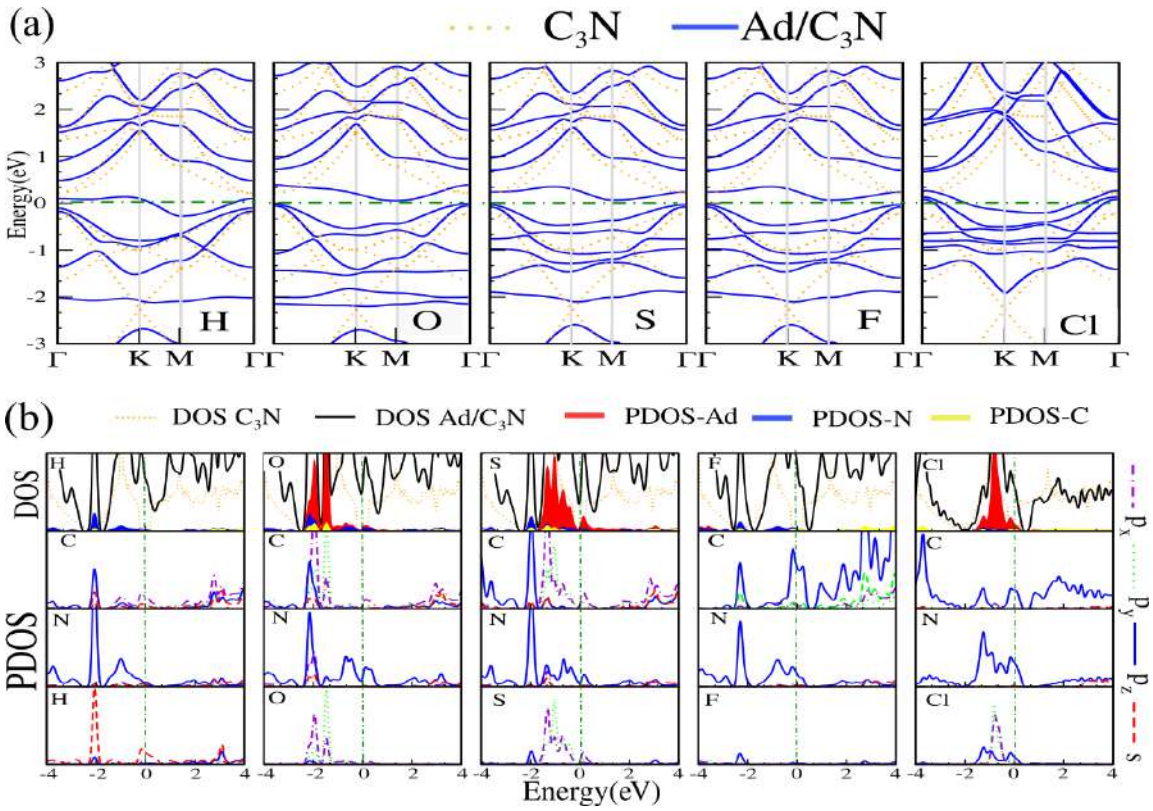

Figure 2.6: (a) Electronic band structure with corresponding, (b) DOS and PDOS of C_3N with H, O, S, F and Cl adatoms at stable T_C-site. The zero of the energy is set at E_F shown by the dashed green-point line.

Ad/C_3N (Ad= B, C, Si, N and P). The interaction of these adatoms with C_3N, eliminates the semiconducting band gap of pristine C_3N and induce metallic properties, and mostly provide a p-type charge carrier. From the DOS and PDOS shown in Fig. 2.7(b), we can see that the VBM of Ad/C_3N is due to the hybridization of $s, p_{x,y,z}$-adatoms orbitals with p_z-orbitals of the nearest C and N atoms. The main contribution to VBM comes from; for example B-s, B-p_z and C and N-p_z orbitals hybridization, whereas B-$p_{x,y}$ and C/N-p_z orbitals does not mix. The CBM of both B and N is formed by hybridization of B-p_x with N-p_z orbital states of C_3N.

2.4.2 Adsorption of alkali and alkaline-earth adatoms

In here, we study of adsorbed Al, AMs (Li, Na and K) and AEMs (Be, Mg and Ca) adatoms at stable H_{CC}-site. The optimized atomic structures with corresponding, difference charge

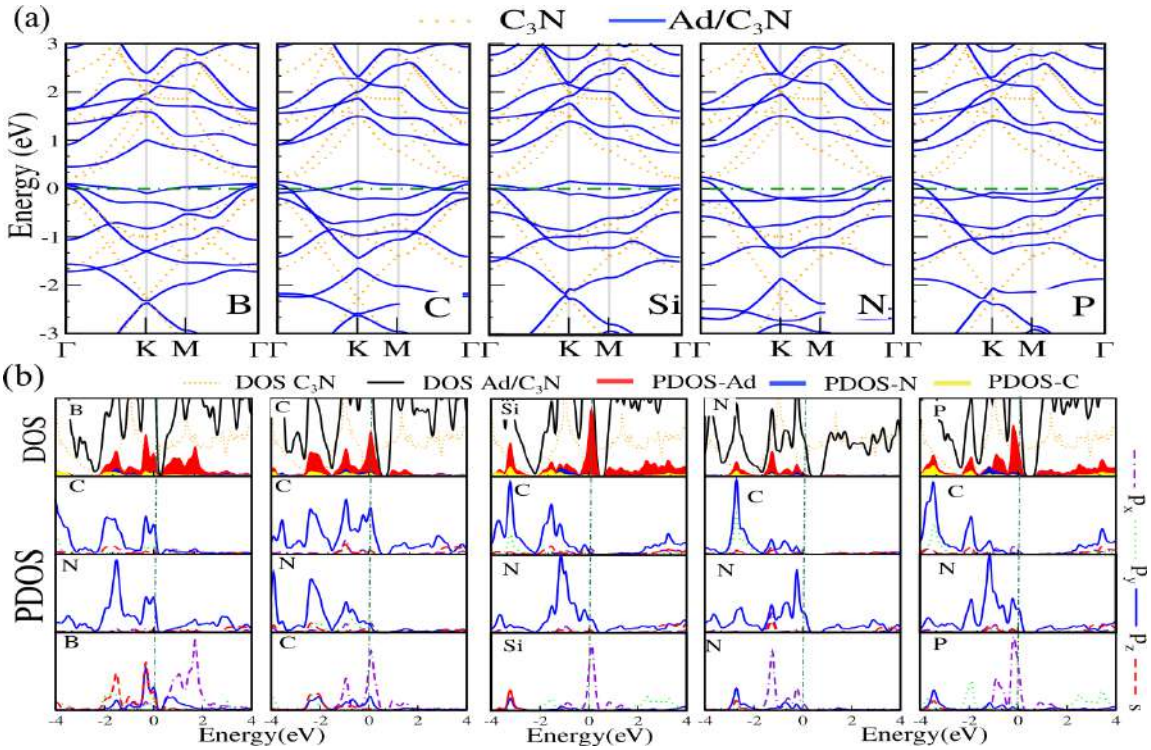

Figure 2.7: (a) Electronic band structure with corresponding, (b) DOS and PDOS of adsorbed B, C, Si, N and P adatoms at T_C-site. The zero of the energy is set at E_F shown by the dashed green-point line.

density of the C_3N with Li, Na, K, Be, Mg, Ca and Al adatoms at stable sites are shown in Fig. 2.8. These adatoms species are located above the hollow site above the center of a hexagon with six C atoms of C_3N at stable H_{CC}-site. In contrast H, O, S, F, C, Si, N and P which cause strongly distortions in the C_3N structure, adsorption of Li, Na, K, Be, Mg, Ca and Al adatoms to C_3N, due to the weaker interaction between adatoms and C_3N, does not yield any significant distortion. Accordingly, calculated adsorption energies range between 0.44 and 1.2 eV. The structure of the Ad/C_3N and the structural parameters of the adatoms adsorbed on C_3N are listed in Table I. The adatoms adsorbed on C_3N at H_{CC}-site have h=1.8-3.6 Å, and the adatoms do not shift neighboring C atoms and buckling is negligible. Among the adatoms, Na adatom binds most strongly to C_3N, which generates the shortest d_{AC}=2.25 Å and the smallest h=1.83 Å. It is also found that h increases from Li to K due to the increasing atomic radius. The transfer of charge between adatoms and the C_3N is $\sim$ 0.2-0.9 eV for Li, Na and K/C_3N, respectively, indicating an ionic bonding character between adatoms and its neighboring C atoms. Band structure

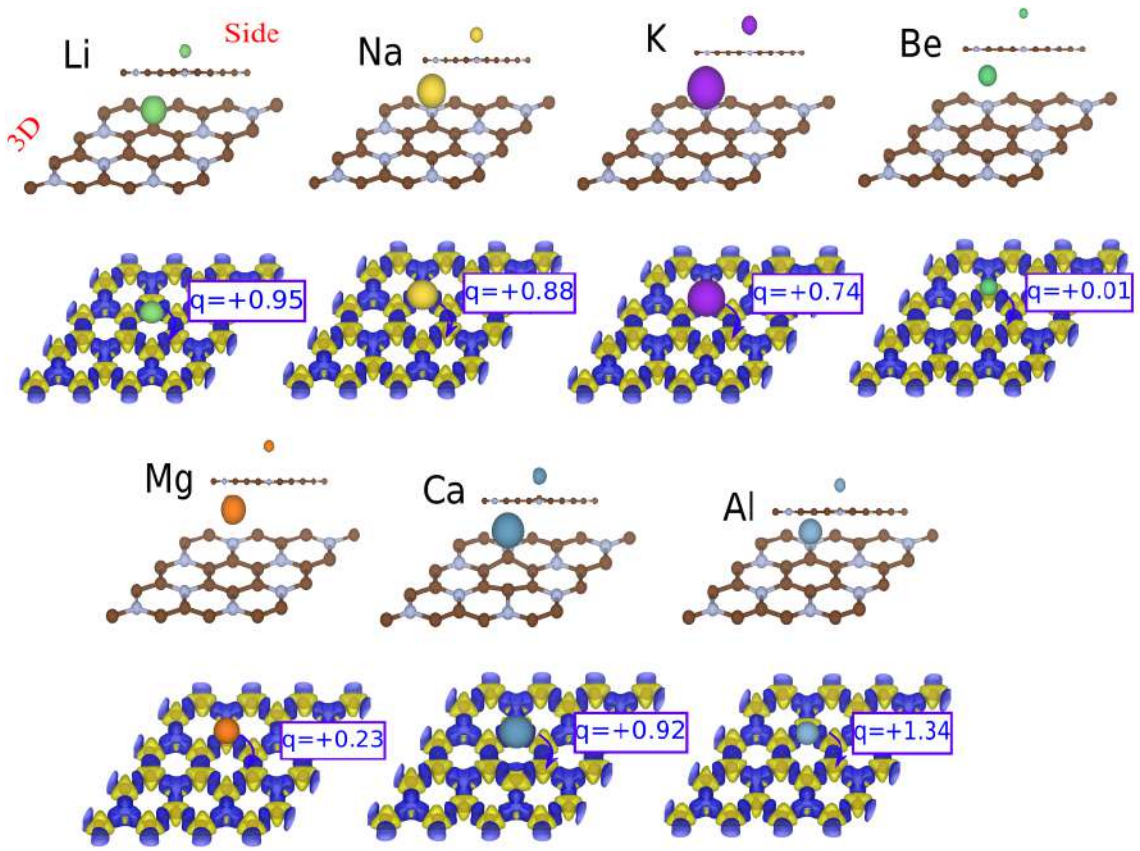

Figure 2.8: (a) Optimized atomic structures with corresponding, difference charge density of the C_3N with Li, Na, K, Be, Mg, Ca and Al adatoms at stable sites.

with corresponding DOS and PDOS for Ad/C_3N (Ad= Li, Na, K, Be, Mg, Ca and Al) at the stable H_{CC}-site are shown in Figs. 2.9(a,b). The adsorption of AEM adatoms, turns semiconductor C_3N metallic. In the case of Be, Mg and Ca, due to the donation of $\sim$ 0.8 eV charge from the AMs into the C_3N, it remains semiconducting with $E_g = 0.43$, 0.43 and 0.16 eV. Compared with the band structure of pristine C_3N, the AM adatoms adsorption bands concentrate mainly at the vicinity of 0.5 eV, which are formed by the hybridization between AM adatom s and C/N-p_z orbital states. Each isolated AMs has a net initial magnetic moment of 1 μ_B, and the $\uparrow$ and $\downarrow$ spin degeneracy is not broken upon charge transfer and therefore all the AMs and AEMs adsorption on C_3N are nonmagnetic. From the PDOS shown in Fig. 2.9(b), the VBM of Ad/C_3N is due to the hybridization of C-p_z orbital with the Li, Na, K, Be, Mg, Ca and Al adatoms s-orbital states around E_F. Due to the charge transfer, E_F is shifted, while $p_{x,y,z}$-orbital of adatoms does not mix with

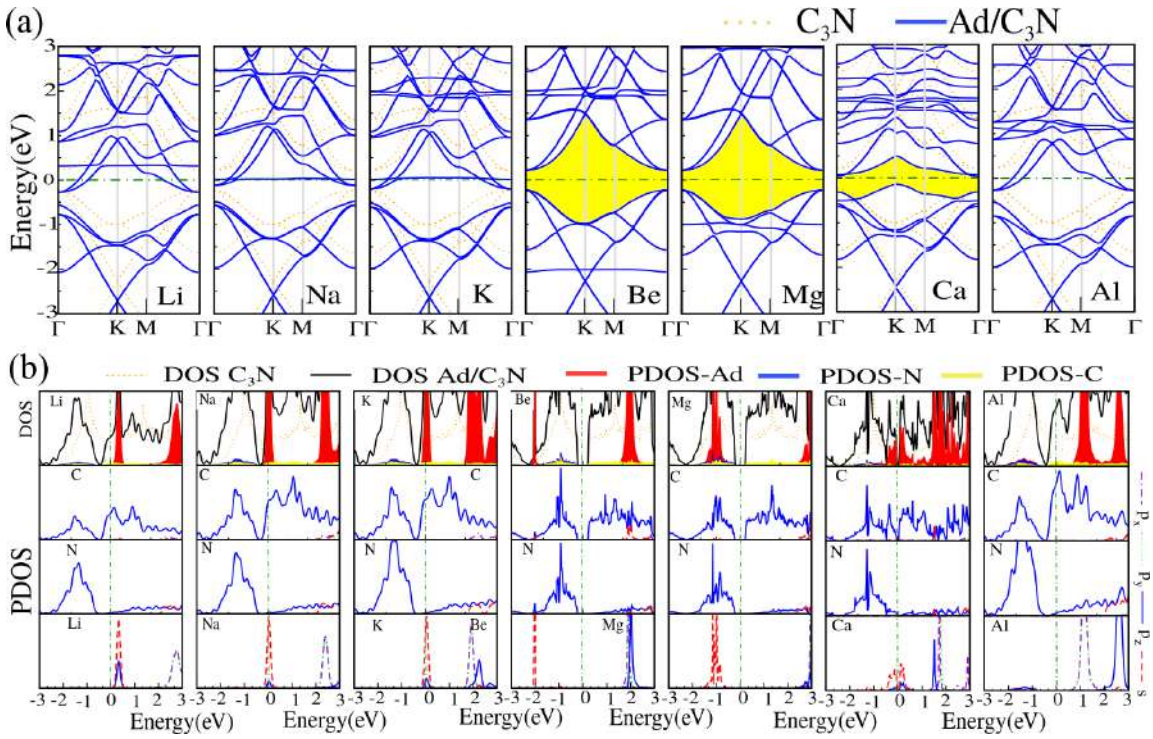

Figure 2.9: (a) Electronic band structures with corresponding, (b) DOS and PDOS of adsorbed Li, Na, K, Be, Mg, Ca and Al adatoms at stable H_{CC}-site. The zero of the energy is set at E_F shown by the dashed green-point line.

C states. The CBM of Ad/C_3N is due to the hybridization of C-p_z orbital with adatoms $p_{x,y,z}$-orbital states. For example, the CBM of Al is formed by hybridization of Al-p_{xy} and C-p_z orbital states of C_3N. Differing from Be and Mg, Ca/C_3N yield Ca states around E_F. While the VB originate mainly from the N-p_z orbital states, the CB is composed of C-p_z orbitals.

2.4.3 Adsorption of 3d-transition metal adatoms

The optimized atomic structures with corresponding, difference charge density of the C_3N with Sc, Ti, V, Cr, Mn, Fe, Co, Ni, Cu and Zn adatoms at stable sites are shown in Fig. 2.10. For the TMs/C_3N (TM=Sc, Ti, V, Cr, Mn, Fe, Co, Ni, Cu and Zn), adsorption energies are in the range of $\sim$ 0.08-3 eV (see Table I). Ti and Zn have largest and smallest adsorption energy among TMs adatoms on C_3N. The Zn adatom has the largest bond length of 3.4 Å. Top and side views of the structure of TMs/C_3N and the structural parameters including

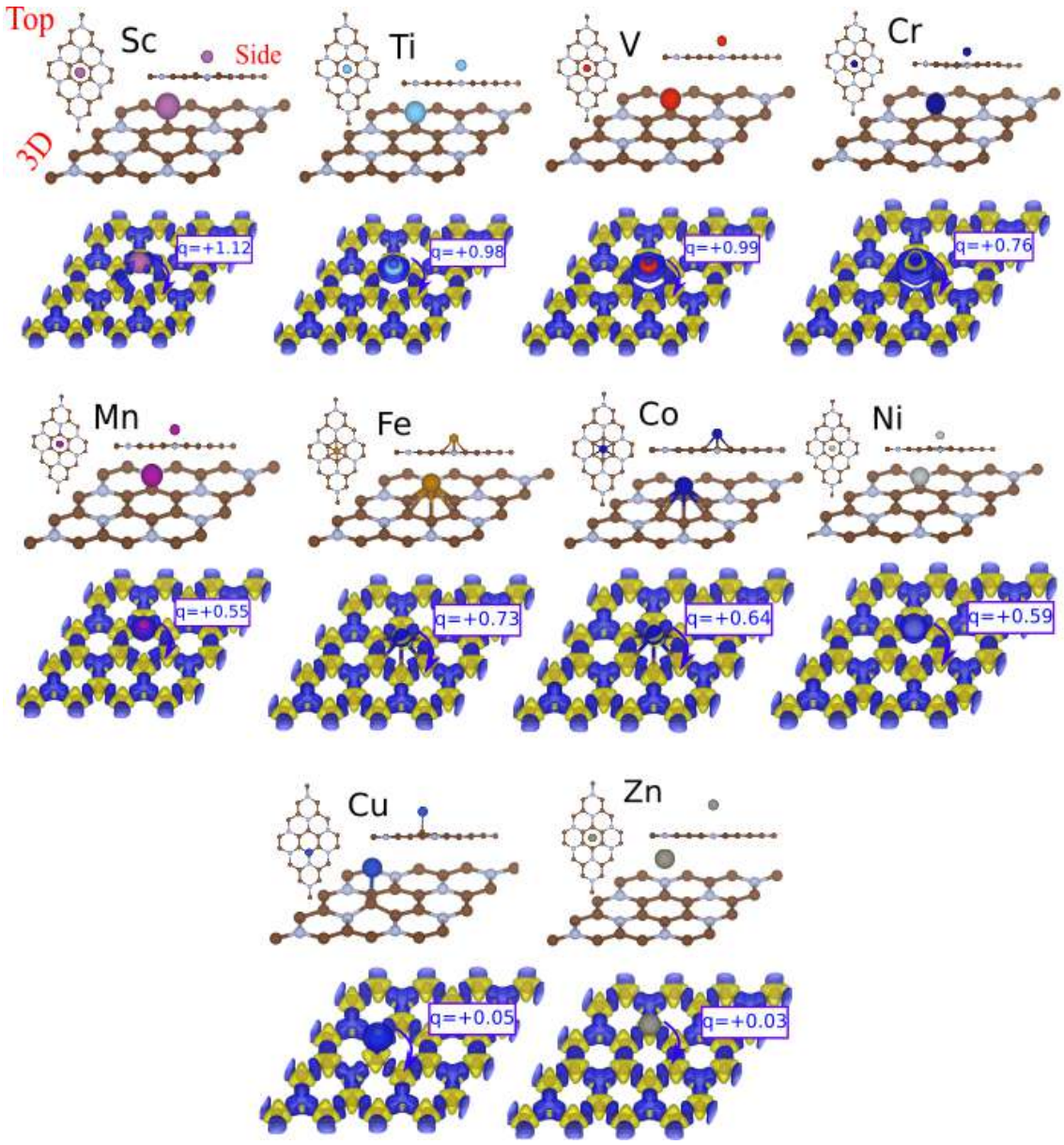

Figure 2.10: Optimized atomic structures with corresponding, difference charge density of the C_3N with Sc, Ti, V, Cr, Mn, Fe, Co, Ni, Cu and Zn adatoms at stable sites.

d_{AC}, d_{CC}, d_{NC}, h, Δz for adatoms are listed in Table 1. For TMs/C_3N, the adatoms height are also relative larger (about 2-3 Å), while the buckling of C atoms is relative small. For Ti/C_3N, a charge accumulation appears in the region between Ti and the neighboring C

atoms and shows a strong covalent bonding character in the formed d_{Ti-C}. Such strong covalent bonding is also found in most other TMs/C_3N. In addition, we also calculated the charge transfer between TM adatom and the C_3N. The corresponding results are listed in Table I, with some degree of ionic bonding for these structures. After optimization, it is the Fe and Co adatoms that bind to the six C with adatom height 1.5 Å for both and d_{Fe-C} and d_{Ni-C} is only 2 Å. We can see that for Cu/C_3N at the stable B_{CC}-site, d_{AC}= 2 Å, and the C atoms directly below Cu adatom undergoes a notable displacement towards the opposite direction, resulting in a buckling of 0.369 Å. However, the charge accumulation in the region between Zn and the neighboring C atoms is less for Zn/C_3N, and thus the d_{Zn-C} only display slightly covalent bonding character.

The band structure of TMs adatoms at stable site with corresponding spin-polarization DOS and PDOS, are shown in Figs. 2.11(a,b). Though the 3d-orbital have similar energy values with 4s-orbital states, is partially occupied, in addition the initial magnetic moments of isolated TMs are nonzero unless the 3d-orbital shell is completely occupied. As the 3d-orbital are near to the nucleus, TMs with their partially occupied 3d-orbital shells are relaxed to different stable sites on C_3N and we can expect a variety of electronic properties. We can see that in the Sc, Ti and V/C_3N energy bands split into $\uparrow$ and $\downarrow$ spin channels resulting in a ferromagnetic-metal, while the Cr/C_3N, becomes a direct semiconductor with 0.44 eV band gap. The Mn/C_3N exhibit a ferromagnetic-metal for both $\uparrow$ and $\downarrow$ spin channels (see Fig. 2.11(a)). The hybridized sp-orbital states of C and N are shown at the CB and lower energy of the VB (see Fig. 2.11(b)). For TMs adatoms, strong and weak hybridization between 3d and the C/N-p_z orbital states is found, while we found a strong as well as weak covalent bonding character between TM adatom and C_3N. The TMs adsorption induces magnetic moments in the C_3N yielding an exchange-splitting in 3d-orbital.

In the case of Ni, Cr, Zn and Cu exhibit no spin-splitting due to their nonmagnetic ground state (see Fig. 8(b)). While the isolated Sc, Ti and V adatoms, have initial magnetic moments of 1.0, 2.0 and 3.0 μ_B, respectively and when on C_3N exhibits a ferromagnetic-metal with 1.1, 2.56 and 2.0 μ_B magnetic moments, respectively for the Sc-4s and Sc-3d orbital states, spin-splitting can be found in the vicinity of E_F of the main 3d-orbital peaks located at the CBM zone. Metallic energy bands of the Sc/C_3N originate from the Sc-$d_{xy}(\uparrow)$ and C/N-p_z orbital states. For Ti, the spin-splitting is slightly larger than for Sc, resulting in strong bonding and the degeneracies of the Ti-3d orbital states are broken. Metallic state originate from the $Ti-3d_{x^2-y^2}(\uparrow)/4s(\uparrow)$ with C and N-$p_z(\downarrow)$ orbital states. In the V/C_3N, metallic energy bands originates from the $3d_{x^2-y^2}(\uparrow)/4s(\uparrow)$ with C-$p_z(\downarrow)$ and N-$p_z(\uparrow)$ orbitals, respectively. With adsorption of Mn, the degeneracy of $\uparrow$ and $\downarrow$ spin channels is shifted and induce 3.56 μ_B and both spin states have metallic character, that originates from the $4s(\uparrow)$ and $3d_{z^2}(\downarrow)/3d_{xy}$-orbital at E_F with 3.6 μ_B magnetic moment.

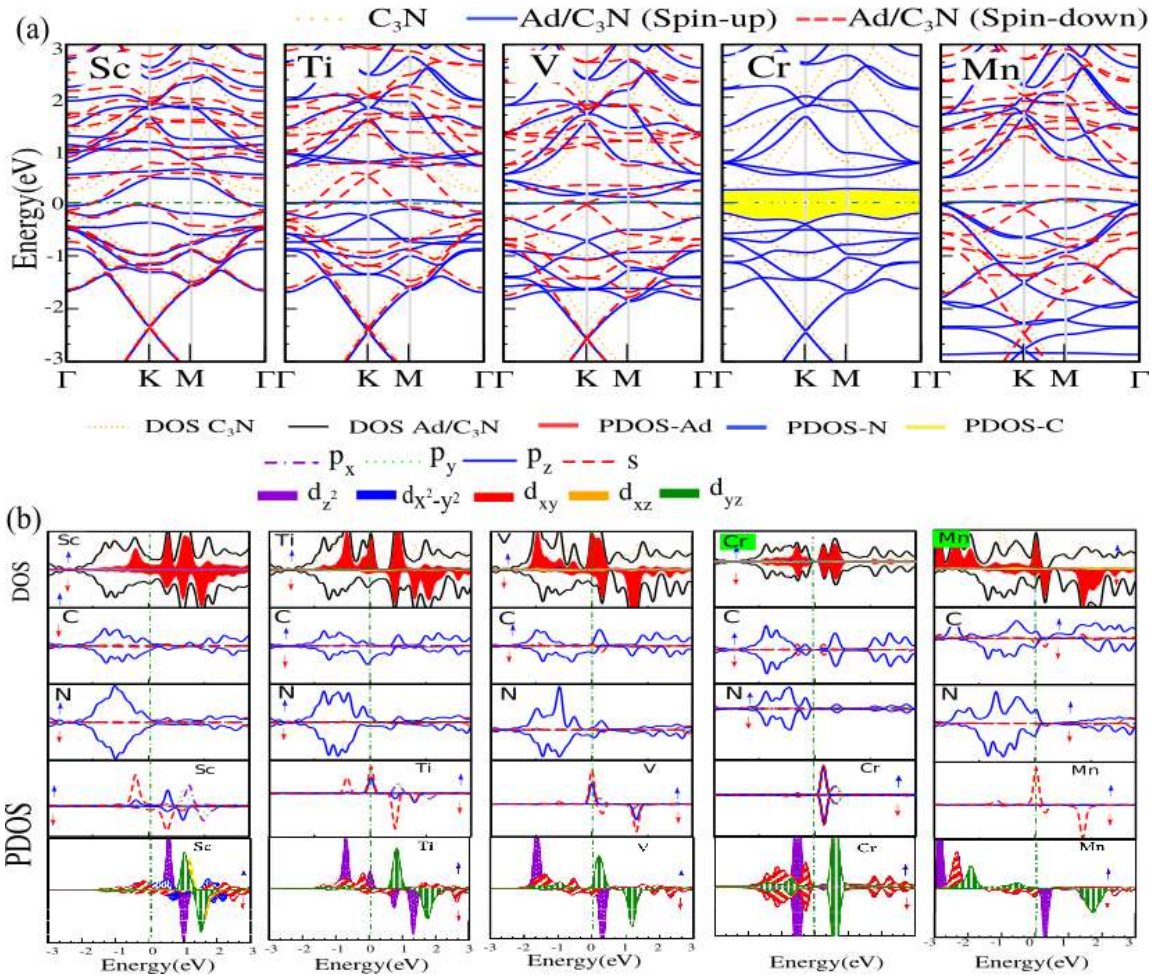

Figure 2.11: (a) Electronic band structures with corresponding, (b) DOS and PDOS of adsorbed Sc, Ti, V, Cr, Mn, Fe, Co, Ni, Cu and Zn adatoms at stable sites.

The Fe and Co have the smallest atomic size of the considered TMs, they are the most closely bonded one among all TM adatoms. The Fe/C_3N, exhibit a dilute-magnetic semiconductor with an indirect band gap of 0.35 and zero eV in the ↑ and ↓ spin channels, respectively. The bands around E_F mainly originate from the hybridization of Fe-4s(↑) orbital. For Co/C_3N, the configuration remains semiconducting with a direct band gap of $\sim$ 0.55 eV in the electron ↑ spin state, whereas the ↓ spin band shows a metallic behavior, thus the density of ↑ and ↓ spin channels exhibit a spin polarization at E_F and Co/C_3N becomes a half-metal. This suggests that the charge carriers within the vicinity of E_F are mobile,

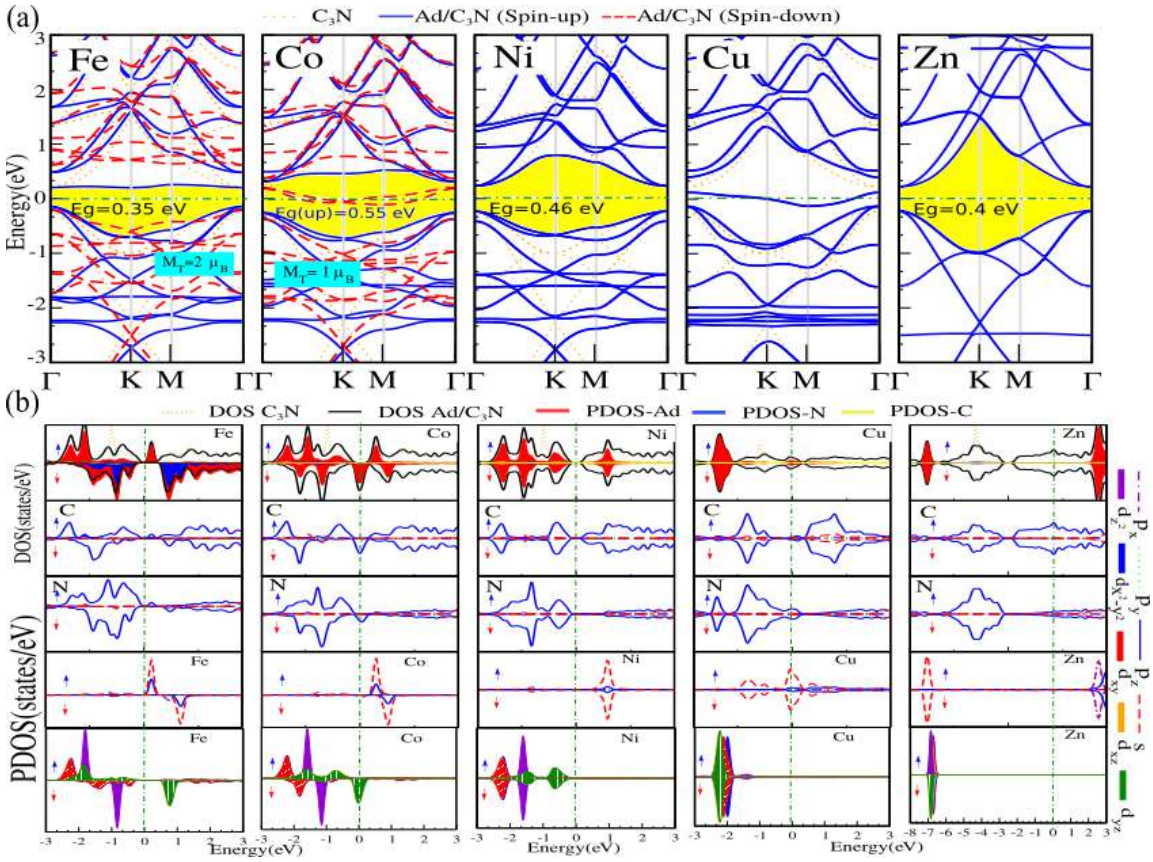

Figure 2.12: (a) Electronic band structure with corresponding, (b) DOS and PDOS of adsorbed Fe, Co, Ni, Cu and Zn adatoms at stable site. The zero of the energy is set at E_F shown by the dashed green-point line.

which is not only useful for conductive behavior but also for magnetic coupling. The bands around E_F mainly originate from the hybridization of $d_{xy,yz,xz}/d_{x^2-y^2}(\downarrow)$-orbitals and the C-$p_z(\downarrow)$ orbital states. In addition, the degeneracy of $\uparrow$ and $\downarrow$ spin states are broken and induces 2.0 and 1.0 μ_B magnetic moments, respectively. Note that the half-metal behavior in Co/C_3N can be quite important for application in spintronics. The Ni and Zn/C_3N, exhibit a direct semiconductor with 0.46 and 0.4 eV band gaps, respectively, while the Cu/C_3N, becomes a metal. For Ni, Zn and Cu/C_3N, we can see that the 4s and 3d-orbitals in the $\uparrow$ and $\downarrow$ spin states are completely occupied and there is no spin-splitting and the configuration is nonmagnetic (see Fig. 2.12(b)).

In order to know the spin state arrangement on each atom, the difference spin density of the Sc, Ti, V, Mn, Fe and Co/C_3N is shown in Fig. 2.13(a). The blue and yellow colors

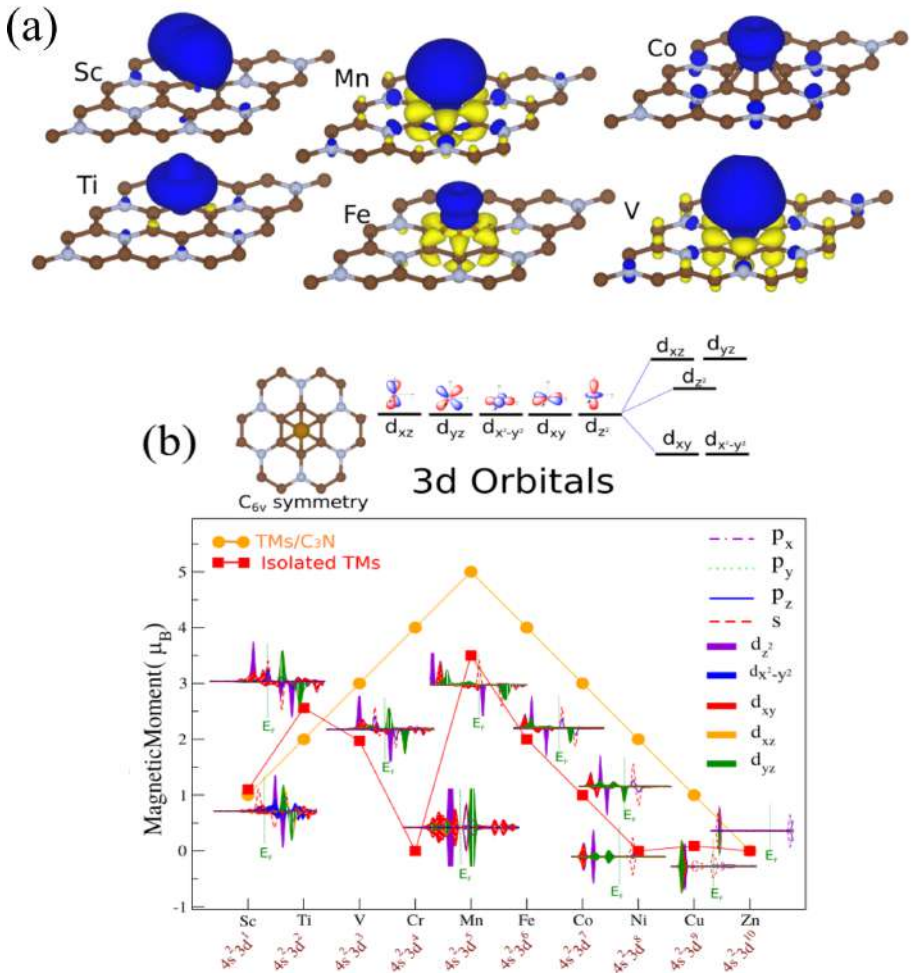

Figure 2.13: (a) Difference spin densities of TMs/C_3N (Ad= Fe, Co, Ni and Zn). The blue and yellow colors show the ↑ and ↓ spin states directions, respectively. (b) Magnetic moment of TMs/C_3N. The energy scheme of 3d-orbital states spin-splitting under hexagonal crystal field (top figure).

show the ↑ and ↓ spin states, respectively. The difference spin density of Sc and Ti/C_3N, show that the spin accumulates mainly around Sc and Ti adatom with its six C atom neighbors, thus displaying ferromagnetic interaction between them. We can see, a highly localized spin density around V and Mn/C_3N and its six C atom neighbors, thus indicating an anti-ferromagnetic interaction between them. The difference spin density of Co/C_3N, shows that the spin accumulates mainly around Co adatom and its six C atom neighbors, thus displaying FM interaction between them, while this is different for Fe/C_3N. We can see from right panel of Fig. 2.13(a), a highly localized difference spin density around Fe

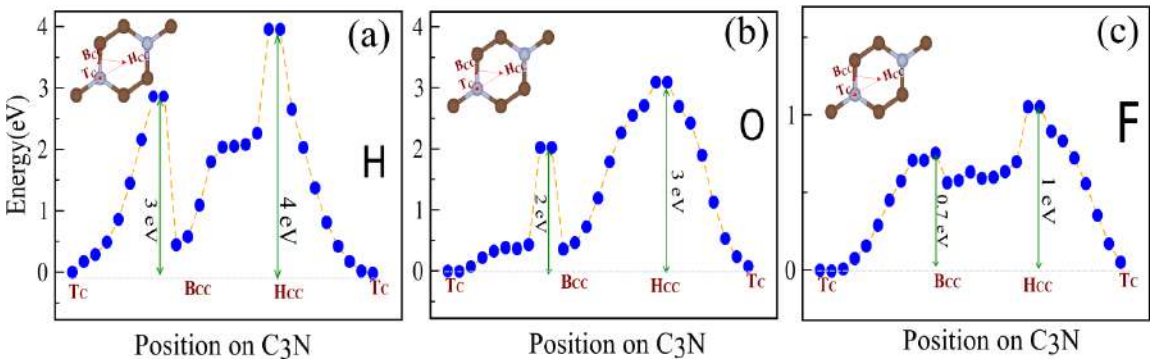

Figure 2.14: Total energy of an adsorbed adatoms at the symmetry points and motion along the symmetry ($T_C \longrightarrow B_{CC} \longrightarrow H_{CC} \longrightarrow T_C$) directions

adatom and its six C atom neighbors, indicating an anti-ferromagnetic interaction between them.

Adsorption of TMs adatoms on the C_3N can significantly modulate the magnetic and electronic properties. In here we analyze the spin-splitting of 3d-orbitals in the TMs/C_3N under hexagonal crystal field. The hexagon ring of C_3N is made of six C atoms as a stable H_{CC}-site, creating hexagonal crystal field, that can trap TMs adatoms. As a result the occupied asymmetrically $d_{xy}/d_{x^2-y^2}$-orbital, could break the hexagonal symmetry leading to a Jahn-Teller-type distortion [146], which cause TMs adatoms shift toward $d_{xy}/d_{x^2-y^2}$ orbitals. From Fig. 2.13(b), we see that the degenerate 3d-orbitals are broken into three energy levels, which consist of two-fold degenerate d_{xz}/d_{yz} and $d_{x^2-y^2}/d_{xy}$ with non-degenerate d_{z^2}-orbital. Due to the repulsive effect between $3d$-orbital electrons and the C-$p_{x,y}$ orbital states, the in-plane 3d-orbitals including $d_{xy}/d_{x^2-y^2}$-orbitals, have a relatively higher energy because of facing the C-$p_{x,y}$ orbitals, while the other orbitals are out of plane, such as d_{xz}, d_{yz} and d_{z^2}-orbitals that are located at lower energy.

2.4.4 Effect of atom diffusion

In order to reveal whether the adatoms adsorbed on C_3N can diffuse or migrate, we investigate as an example the energy barriers for the displacement of single H, O and F adatoms. The variation of total energy in the Ad/C_3N at the symmetry points and motion along the $T_C \longrightarrow B_{CC} \longrightarrow H_{CC} \longrightarrow T_C$ directions or the migration on a hexagon is shown in Fig. 2.14. By using these total energy curves we obtain the energy barriers that have to be overcome by the adsorbate in order to diffuse or migrate on the C_3N surface. The minimum energy barrier occurs at the B_{CC}-site between two adjacent T_C-sites. This analysis suggests that a diffusing adatom can take a path of minimum energy barrier following the

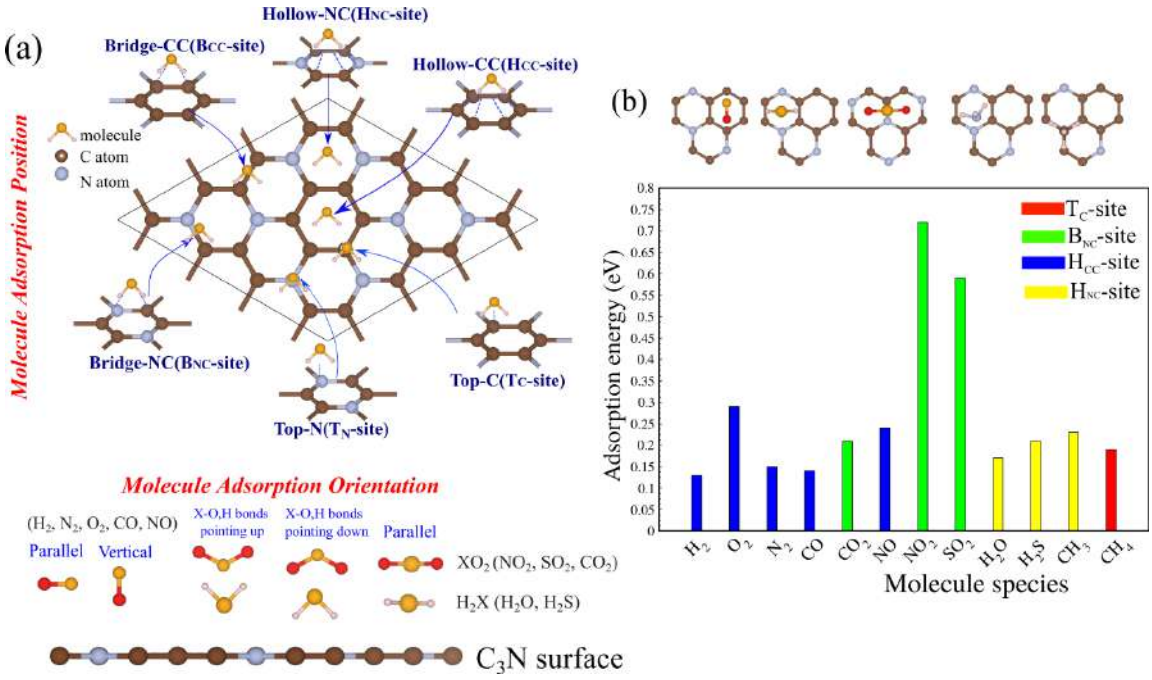

Figure 2.15: Schematic view of favorable adsorption (a) sites and (b) orientation of molecules including H_2,N_2, O_2, CO, CO_2, NO, NO_2, SO_2, H_2O, H_2S, NH_3 and CH_4 on the C_3N. (c) Top view of the final structure of C_3N adsorbed with various gas molecules corresponding to the stable sites. (d) Adsorption energy of molecules on C_3N at most stable site.

edges of the hexagon at one T_C-site to an other T_C-site through the barrier in the range of 1-4 eV at H_{CC}-site. This barrier energy is very large and does not allow adatoms to migrate on the surface of C_3N.

2.5 Adsorption of molecule

2.5.1 Introduction

Due to the thin thickness and large surface-to-volume ratio of two-dimensional materials (2DM), the electronic and magnetic properties can be tuned by adsorbate molecules. Furthermore, adsorption is a significant initial step in the activation of gas molecules. Detection of gas molecules is of great importance in both human health and environmental protection. [113, 114] The various types of gas sensors may be useful for numerous applications, such as in medical diagnosis, environmental monitoring and surveillance, agriculture production, military safety and emission control [114, 115]. The adsorption of

molecules has been extensively studied by first-principle calculations on graphene [116–121] and other 2DM [122–124].

In this section, we study systemically the adsorption of numerous gas molecules such as, atmospheric gas molecules (including H_2, O_2, CO_2 and H_2O) and common polluted gases (including CO, NO, NO_2, SO_2, H_2S, NH_3 and CH_4) on C_3N. These kinds of calculation results will help to expand our understanding of molecule-C_3N interaction and could be of practical interest in different applications.

2.5.2 Structural and energetic properties

Adsorption of gas molecules affects on the structural and electronic properties of 2DM. Schematic view of favorable adsorption sites of gas molecules including H_2, N_2, O_2, CO, CO_2, NO, NO_2, SO_2, H_2O, H_2S, NH_3O and CH_4O on C_3N are shown in Fig. 2.15(a). After structural optimization, the most stable site configuration among the six different sites are determined where all atoms are relaxed in all direction.

These six possible adsorption sites includes: (1) the hollow site above the center of a hexagon with six C atoms (H_{CC}), (2) the hollow site above the center of a hexagon with composed of both C and N atoms (H_{NC}), (3) the bridge site above the middle of a C-C bond (B_{CC}), (4) the bridge site above the middle of a N-C bond (B_{NC}), (5) the top site above a C atom (T_C), and (6) the top site above a N atom (T_N) (see Fig. 2.15(a)). Schematic view of favorable adsorbed molecule orientation on C_3N at stable sites, is shown in Fig. 2.15(b). In the first step, the molecule is placed above these adsorption sites, for each of which different orientations of molecules are assessed. Several typical orientations of the gas molecule either vertically or parallel to the C_3N surface are examined, and relative rotation of gas molecule to the C_3N surface is considered. For example, for the CO molecule, the molecular axis could be oriented parallel to the C_3N surface or perpendicular with the C or O atom pointing to the C_3N surface. While for the molecule SO_2, the molecular plane could be oriented parallel to the C_3N surface: the S-O bonds are towards the C_3N surface. The adsorption energy of the molecule on C_3N was determined as $E_a = E_{C_3N} + E_{Mol} - E_{Mol/C_3N}$, where E_{Mol/C_3N}, denote the total energy of the structure with the molecule adsorption on C_3N, E_{C_3N} denotes the total energy of the pristine C_3N without molecule, and E_{Mol} denote the total energy of isolated molecule in vacuum. The variation of adsorption energy for different molecules on C_3N at most stable site are shown in Fig. 2.15(b). The configuration will be considered as physisorbed when the adsorption energy is low and the nearest atomic distance between the adsorbed molecule and the support is much larger than the sum of the covalent radii of the corresponding atoms. The adsorption energies of corresponding gas molecules such as H_2, N_2, O_2, CO, CO_2, NO, H_2O, H_2S, NH_3 and CH_4 on C_3N are quite small, as compared with 0.72 eV and

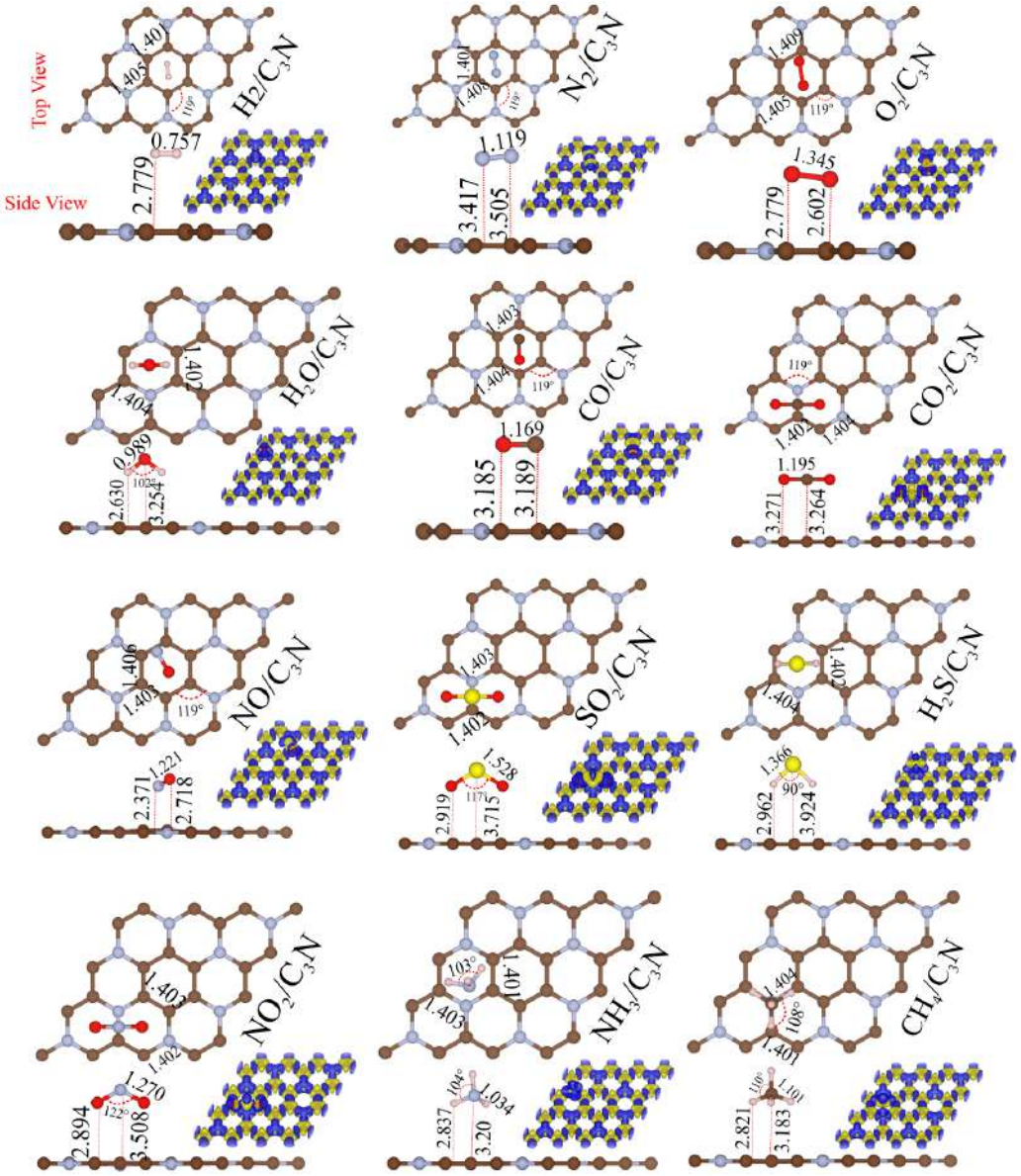

Figure 2.16: Optimized structures with corresponding structural parameter for adsorption of H_2, N_2, O_2, CO, CO_2, NO, NO_2, SO_2, H_2O, H_2S, NH_3 and CH_4 molecules on C_3N at the most stable site. Both, top and side views are shown. Difference charge density are indicated in the same panel. The blue and yellow regions represent charge accumulation and depletion, respectively.

0.59 eV for NO_2 and SO_2, respectively.

The optimized structures with corresponding structural parameter for adsorption of H_2,N_2, O_2, CO, CO_2, NO, NO_2, SO_2, H_2O, H_2S, NH_3 and CH_4 molecules on C_3N at most stable site were are also in Fig. 2.16. It can be seen that the stable adsorption site for H_2, N_2, O_2, CO and NO molecules is at H_{CC}-site, while CO_2 is adsorbed in B_{NC}-site. For H_2 and N_2, the H and N atoms points towards the C_3N surface and bond lengths are 0.757 (H-H) and 1.119 (N-N) Å. For O_2, O atom points toward the C_3N surface and O-O bond length is 1.345 Å, while the CO points parallel to the C_3N surface and C-O bond length is 1.345 Å. In CO_2, the C-O bond length is 1.195 Å. The N atom of NO molecule, points toward the surface and bond length of N-O is 1.221 Å. Also the closest distance between the lower atoms of the molecules with the C_3N surface is in the range of 2.371 Å (NO)- 3.564 Å (CO_2). The adsorption energy of H_2, N_2, O_2, CO, CO_2 and NO molecules is 0.13, 0.15, 0.29, 0.24, 0.21 and 0.24 eV respectively, which can be considered as physisorption which agrees with the relative large distance between these molecules and the C_3N surface. The stable adsorption site for NO_2 and SO_2 is B_{NC}-site, while the H_2O and H_2S molecules are adsorbed at H_{NC}-site. For NO_2 and SO_2, bond lengths were calculated as 1.270 Å (N-O) and 1.528 Å (S-O), while the bond angles are 122° (O-N-O) and 117° (O-S-O). The distance between the molecules and the C_3N surface are 2.894 (NO_2), 2.919 (SO_2), 2.630 (H_2O) and 2.962 Å (H_2S). The NO_2 and SO_2, have large adsorption energy of 0.72 eV and 0.59 eV, respectively, which can be considered as weak chemisorption. Whereas, H_2O and H_2S exhibit a small adsorption energy of, respectively, 0.17 and 0.21 eV and therefore can be considered as physisorption. It was found that the NH_3 and CH_4 molecules are located at stable adsorption site of H_{NC} and T_C, respectively. The N-H bond length is 1.304 Å and the H-N-H bond angle is 104°, while the distance between NH_3 with the C_3N surface is 2.837 Å. The closest distance of the most stable site between CH_4 molecule with the C_3N surface is 2.821 Å. The C-H bond lengths were 1.101 Å and the H-C-H bond angle is 110°. The NH_3 and CH_4/C_3N, had adsorption energy of 0.23 eV and 0.19 eV, respectively. To know the bonding character between molecules and C_3N, the difference charge densities indicated, in the same panel in Fig. 2.16. The blue and yellow regions represent the charge accumulation and depletion, respectively.

To know the bonding character between molecules and C_3N, the difference charge densities indicated, in the same panel in Fig. 2.16. The blue and yellow regions represent the charge accumulation and depletion, respectively. It can be seen that electrons were accumulated on the atoms of H_2,N_2, O_2, CO, CO_2 and NO molecules, whereas the depletion of electrons in its three nearest C neighbors of C_3N, which shows that there are small charge transfers from C_3N to these molecules. Difference charge density of these molecules indicates, that there is no formation of chemical bonds, hence we have physisorption rather than chemisorption. The charge transfer analysis showed weak electron

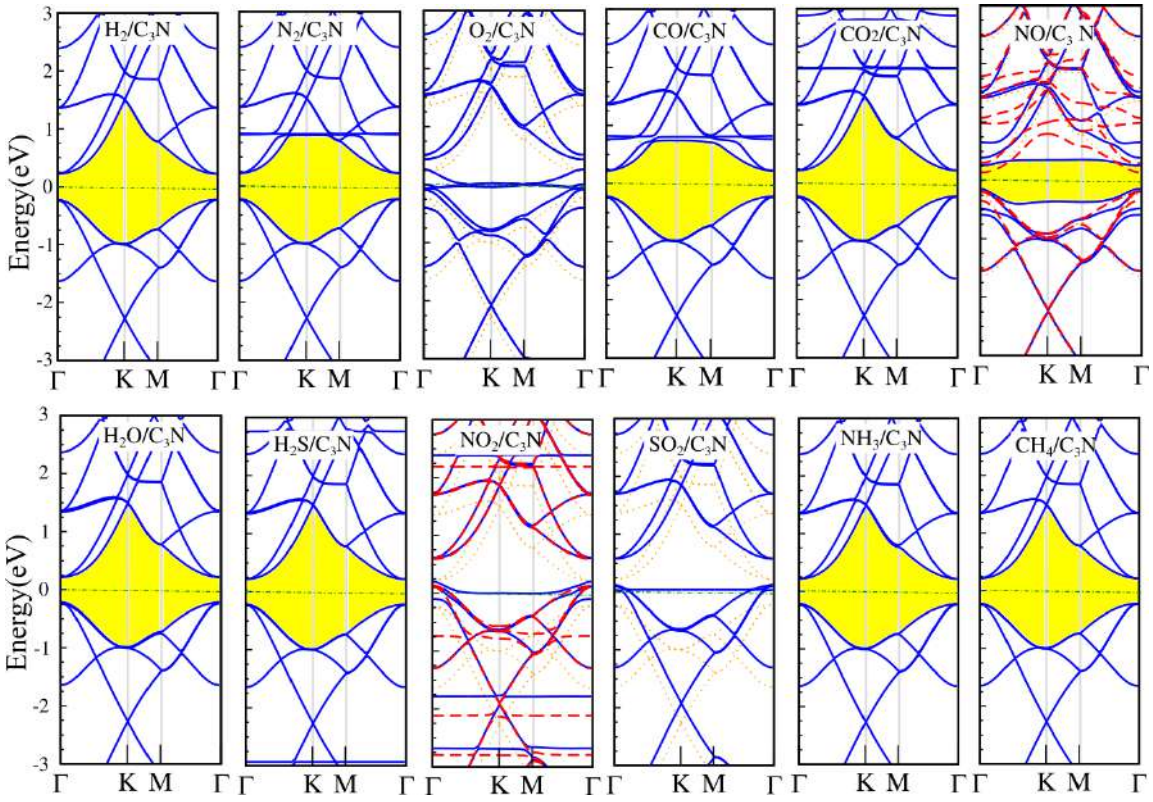

Figure 2.17: Electronic band structure for adsorption of H_2, N_2, O_2, CO, CO_2, NO, NO_2, SO_2, H_2O, H_2S, NH_3 and CH_4 molecules on C_3N at the most stable site. The zero of energy is set at E_F.

acceptors by gaining electrons of 0.01e (H_2), 0.01e (N_2), 0.19e (O_2), 0.14e (CO), 0.14e (NO), 0.01e (H_2O) and 0.02e (H_2S) from C_3N. Such a subtle charge transfer indicates that these molecules were physisorbed on C_3N through weak van der Waals interaction. The charge transfer calculations showed that NO_2 and SO_2 are strong electron acceptors by gaining 0.26 e and 0.23 e electrons from C_3N to NO_2 and SO_2, respectively. Such a large charge transfer shows that NO_2 and SO_2 is weak chemisorbed on C_3N. Moreover, the electrons were depleted on the atoms of CO_2, NH_3 and CH_4, whereas electrons are accumulated on C_3N, which shows there is charge transfer from these molecules to C_3N. Charge transfer analysis shows that CO_2, NH_3 and CH_4 act as weak electron donors by donating -0.002e, -0.002e and -0.004e to C_3N.

2.5.3 Electronic and magnetic properties

As shown in Fig. 2.17, H_2, N_2, CO, CO_2, H_2O, H_2S, NH_3 and CH_4/C_3N molecules can hardly change the band structure around E_F. We found that CO/C_3N becomes a semiconductor with band gap 0.4 eV. Furthermore, NO molecule causes modification to the electronic structure and result in induced impurity states around E_F. These impurity states mainly come from states of NO molecule. It is also observed that the $\uparrow$ and $\downarrow$ spin states for NO/C_3N exhibit a dilute-magnetic semiconductor character and induce 1 μ_B magnetic moment. The O_2 and SO_2 molecules modify the electronic state around E_F, giving rise to a vanishing band gap resulting in metallic characteristics with their Fermi levels crossing the electronic states. DOS of these structures is different from that of pristine C_3N, showing an impurity state around E_F. The NO_2 paramagnetic molecule can induce impurity states around E_F and these impurity states come mainly from states of NO_2. It becomes a ferromagnetic-metal and spin-splitting occurs in the $\uparrow$ and $\downarrow$ spin channels and with 0.6 μ_B magnetic moment.

The very weak interaction of H_2, N_2, CO, CO_2 and NO molecules with C_3N is also reflected by the sharp peaks in the PDOS (see Fig. 2.18). For these molecules, the HOMO and LUMO is fully filled and lies about 0.22 eV below and 0.21 eV above E_F, respectively. When these molecules weakly interact with C_3N, it occupies the HOMO state which moves below E_F. Therefore, the net gain of electrons from C_3N acts as an acceptor and the charge transfer are due to orbital overlap between the HOMO of these molecules with C_3N. The LUMO will mostly interact with the DOS above E_F which does not cause any adsorption therefore making HOMO a more important orbital and the charge transfer is consequently always to C_3N. The interaction between O_2 and C_3N is also reflected by the broad peaks in the PDOS. For O_2 molecule, the HOMO and LUMO are 0.05 eV below and 0.004 eV above E_F, respectively. These states induce a small charge transfer from C_3N to O_2. When O_2 molecule strongly interact with C_3N, its occupied HOMO state moves below E_F, increasing electrons in O_2 molecule. Therefore, it makes an acceptor and the charge transfer are due to orbital overlap between the HOMO of O_2 molecule and C_3N. For NO_2 molecule, the HOMO and LUMO of $\uparrow$ spin state are 0.097 eV below and 0.115 eV above E_F, respectively and also HOMO and LUMO of $\downarrow$ spin channel are 0.733 eV below and 0.106 eV above the E_F. For NO_2 molecule, a spin-splitting orbital is located above E_F that contributes to the LUMO state. NO_2 molecule can accept electrons from C_3N and the charge transfer occurs mainly through the orbital hybridization. From the difference spin density of NO and NO_2 molecules, it can be concluded that the magnetism originates mainly from these molecules and its C and N atom neighbors of C_3N. For H_2O and H_2S, HOMO state is completely located on the O atom, but the LUMO state is mostly located on the H atoms, while HOMO plays the prominent role and donates

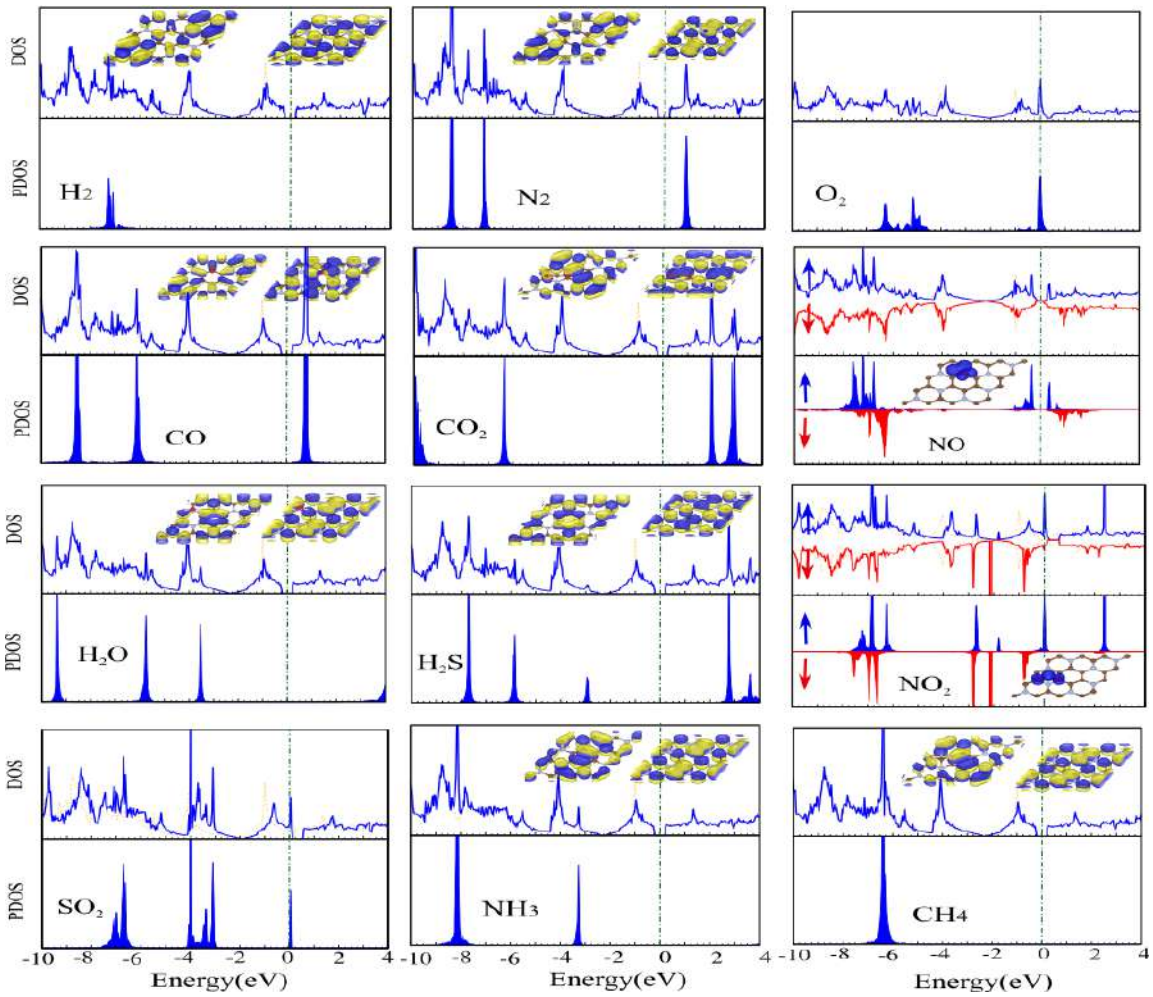

Figure 2.18: DOS and PDOS for adsorption of H_2, N_2, O_2, CO, CO_2, NO, NO_2, SO_2, H_2O, H_2S, NH_3 and CH_4 molecules on C_3N at the most stable site. Charge densities of HOMO and LUMO are shown in the insets. The blue and yellow regions represent charge accumulation and depletion, respectively.

electrons through a small mixing with C_3N orbitals above E_F. There is also a mixing with the orbitals below E_F, because they are closer in energy. These states induce a small charge transfer from C_3N to H_2O and H_2S. The HOMO and LUMO of NH_3 and CH_4 are located 0.21 eV below and 0.21 eV above E_F and these states induce a small charge transfer from these molecules to C_3N. The orbitals originally located above E_F contribute to the LUMO state. It is found that the HOMO is the only orbital that can have a significant overlap with the C_3N orbitals and thus can cause charge transfer. Therefore, these

molecules will act as a donor.

2.6 Summary and conclusions

In summary, based on first-principles calculations, we investigated the structural, electronic and magnetic properties of a novel 2D material, with stoichiometry C_3N that has been recently synthesized from carbonized organic single crystals. The C_3N is an indirect band-gap semiconductor. This study highlights that the adatom adsorption to C_3N is a favorable approach to modulate its properties which may have significant importance because of its basic relevance to applications in catalysis, batteries and nanoelectronics. These results will be very useful for theoretical and experimental studies that are considering the use of atoms and molecules as building blocks for making new nano devices. We investigated systematically the interaction between 27 different adatoms and the C_3N honeycomb structure. These adatoms lead to considerable modifications in the electronic structure, when the related adsorption energy is significant. Under these conditions, the band gap of C_3N can be reduced and the system becomes metal or semiconductor. We presented here the effect of charging, electric field and strain on the electronic and magnetic properties of C_3N and Ti, Mn and Fe/C_3N. Our results show that the band gap and magnetic moment considerable changes with charging, applied electric field and strain. In this way it is possible to tune the electronic and magnetic properties.

Two-dimensional polyaniline with structural unit C_3N is a semiconductor, which has attracted a lot of interest because of its unusual electronic, optoelectronic, thermal and mechanical properties useful for various applications. Understanding the interaction between C_3N and adsorbate gas molecules is important for the exploitation of C_3N in e.g. gas sensors. In summary, using first principle calculations, the adsorption of common atmospheric (H_2, N_2, O_2, CO H_2O and H_2S) and polluted (CO, CO_2, NO, NO_2, SO_2, NH_3 and CH_4) gas molecules on C_3N nanosheet was investigated. A detailed analysis of the optimized atomic structure and electronic properties of adsorption of different molecules was carried out. The results showed that O_2, NO, NO_2 and SO_2 are chemisorbed on C_3N. It was also found that the corresponding electronic structure of C_3N was modified. Adsorption of O_2 and SO_2 molecules, C_3N becomes a metal, while under NO_2 adsorption it turns into a dilute-magnetic semiconductor with 0.6 μ_B magnetic moment. Our computational results show that other molecules including H_2, N_2, CO, CO_2, H_2O, H_2S, NH_3 and CH_4 are physisorbed causing little distortion of C_3N. The amount of charge transfer upon adsorption of these gas molecules are found to be small. Our theoretical studies indicate that C_3N-based sensor has a high potential for O_2, NO, NO_2 and SO_2 detection due to the significant electronic structure changes with moderate adsorption energy.

CHAPTER 3

Functionalization and conformation of atom

3.1 Introduction

Functionalization with oxygen atoms [147], fluorine atoms [47, 148], and hydrogen atoms [149–153], alters the properties of graphene and, in some cases, causes a transition to a different kind of material: For example, full hydrogenation (a graphene layer with full coverage of hydrogen on each side) leads to a nonmagnetic, direct wide-gap semiconductor, as predicted in 2007 by Sofo *et al.* [44] from *ab initio* calculations, which was demonstrated experimentally by Elias *et al.* [154] two years later. Semi-hydrogenation (full coverage of hydrogen on one side), on the other hand, as predicted by Zhou *et al.* [155], produces the ferromagnetic, indirect narrow-gap semiconductor graphone. The predicted transition from graphene to graphone and graphane with increasing hydrogen coverage, demonstrates the decisive role of adsorbed hydrogen for determining the properties of the resulting graphene derivate. The inducing of a magnetic moment in the structure is particularly important for graphene-based spintronics [156, 157]. A number of studies have reported that hydrogenated graphene is magnetic for certain degrees of hydrogenation [158–161]. Optical spectra could be an effective approach of studying the exchange-split electronic band structure of magnetic hydrogenated graphene, and enable the determination of whether the ground state of hydrogenated graphene is magnetic. Functionalization by adsorbed atoms is an approach to tune the atomic, electronic, and magnetic structure of 2DMs; in particular, hydrogenation [68, 162–164]. By chemically modifing C_3N to its fully hydrogenated form (FH) C_3N, each C or N atom in will have an extra nonbonding

electron. Thus, fully hydrogenated C_3N may be expected to have similar properties to graphene, silicene, or germanene, for example, as becoming a Dirac material [165, 166].

In the present chapter, to exploit the application possibilities of C_3N, we performe extensive *ab initio* investigations into the effects of adatom adsorption for a range of coverages, and conformation (Ortho, Meta and Para) as well as nanoribbons and effect of strain, on the properties of C_3N. Our findings indicate that the band gap and magnetism can be modulated with these approaches. In particular, we study the atomic, electronic and magnetic structure of C_3N, semi/fully functionalized with H, O and F atoms. The functionalization, significantly modifies the electronic and magnetic properties, and results in interesting characteristics for C_3N, ranging from metallic, dilute-magnetic semiconducting and insulatoing characteristics. Moreover, we found that in semi and fully hydrogenated C_3N with H vacancy defects, a defect state is induced around the Fermi level, decreasing the band gap, and also interestingly, inducing magnetism in these structures.

We also investigate the adsorption of H adatoms on C_3N nanoribbons, and find that they can induce half-metallic, metallic, semiconducting, and ferromagnetic character. Furthermore, to provide visible guidance for experimental observations, simulated scanning tunneling microscopy (STM) images are calculated. All together our results show wide variety of emergent unique electronic and magnetic properties, which differ significantly from pristine C_3N. We expect that these thorough theoretical studies, and identified interesting phenomena will attract more experimental and theoretical studies and prove useful for engineering and design of new practical applications for C_3N in nanoelectronic, spinronic, catalysts, energy storage and optical device applications.

3.2 Effect of H and O atoms coverages

We have systematically investigated the structural and electronic properties of adsorption of H and O adatoms, for different coverages, on C_3N. It is interesting to note that H/C_3N structures induce metallic character, which can be continuously tuned by varying the H coverage from 3.1% to 12.5%.

The optimized structures, top and side views, of H atom adsorption on C_3N, with difference coverages, calculated using various sized a surface unit-cells, namely, 3.1%, 6.2%, 9.3% and 12.5%, are shown in Fig. 3.1(a). We consider the optimized configuration and electronic structure corresponding to the H atom adsorbed at the most stable T_C-site (on-top of the C-atom). For each coverage, we consider the top, bridge and hollow sites for 1H/C_3N (3.1%), the H atom locates preferentially on top of a C atom (C_H), with formation of a single covalent bond between C_H-H. The C_H-H bond length for a H atom is 1.12 Å, indicating that H is chemically adsorbed on C_3N. The C-C and C-N bonds are elongated

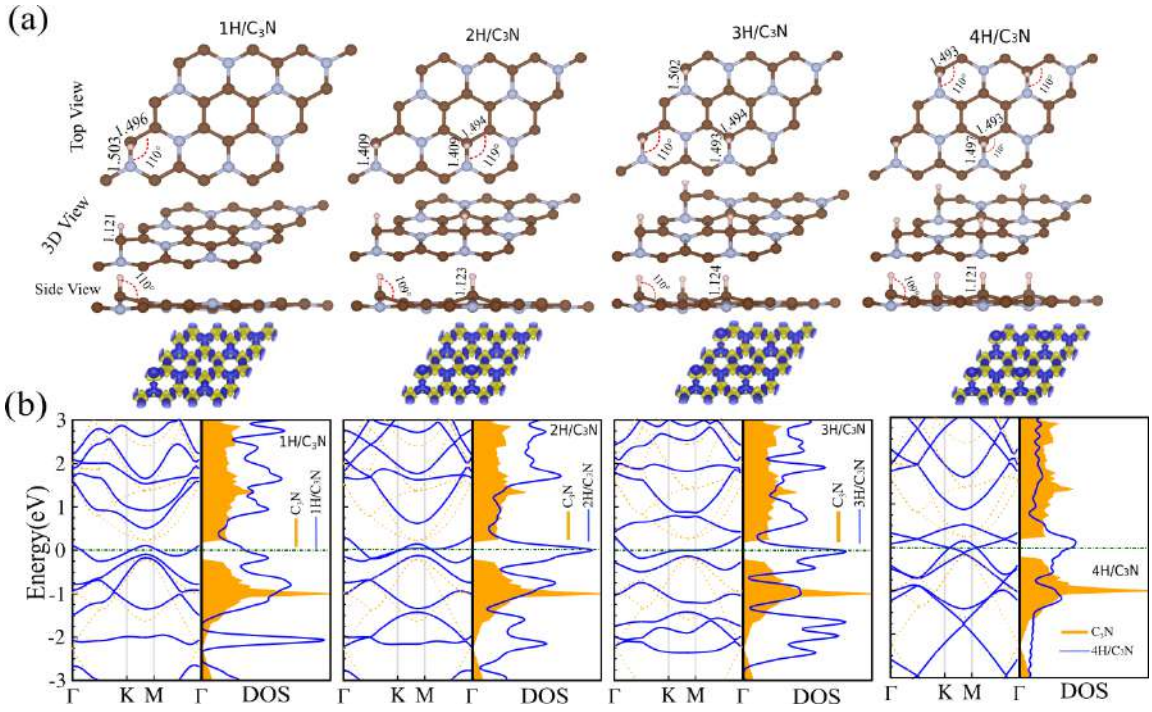

Figure 3.1: Optimized structures, electronic band structure and DOS of H/C_3N for difference coverages of H atoms. (a) Relaxed structure of 3.1% ($C_{32}N_8H_1$), 6.2% ($C_{32}N_8H_2$), 9.3% ($C_{32}N_8H_3$) and 12.5% ($C_{32}N_8H_4$). (b) The corresponding band structure and DOS. Difference charge densities are also shown. The blue and yellow regions represent the charge accumulation and depletion, respectively. The zero of energy is at E_F shown by the dashed green line.

to 1.5 Å in comparison with the C-C and C-N bond lengths (1.404 and 1.403 Å) in pure C_3N. The H-C_H-C angles are in the range of 105-110 °, displaying the characteristic of sp^3 hybridization. The C_H atom moves out of the base plane of C_3N. For 1H/C_3N (3.1%), nearest C atoms to H adatom, move from the C_3N plane in the upward direction and induce a buckling of 0.64 Å. As the coverage of H increases to two H atoms (7.14%), the surface distortion becomes more apparent and the bond lengths of C-C and C-N are changed significantly. We see clearly that these adatoms alter the atomic structure of C_3N as compared with that of pure C_3N. Increasing the hydrogen coverage a similar behavior is exhibited with a more distorted surface configuration.

The difference electron densities are presented in Fig. 3.1(b). It can be seen that there is a high charge density around the N and H atoms on C_3N. This high charge density around the H atom projecting toward the C-N and C-H bonds shows a charge transfer from the C to H atom, indicating a covalent bond. The corresponding electronic band structure and

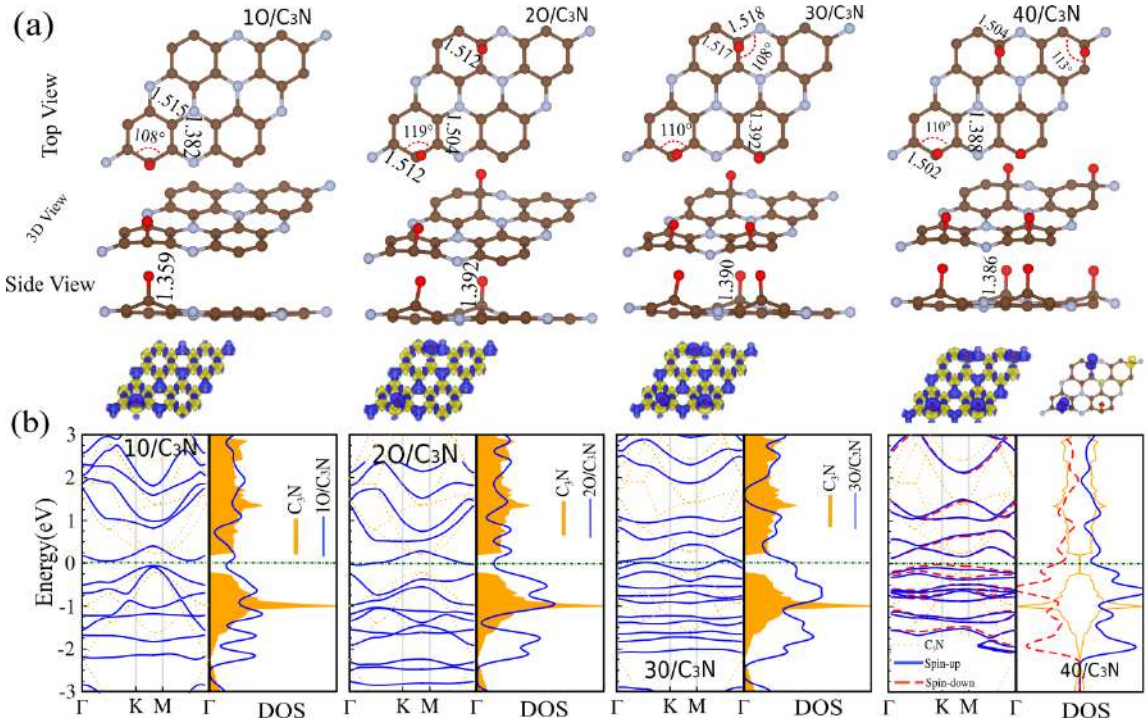

Figure 3.2: Optimized structures, electronic band structure and corresponding DOS of C_3N for difference coverages of O atoms. (a) The relaxed structure of 3.1%, 6.2%, 9.3% and 12.5%. (b) The corresponding band structures and DOS. Difference charge density are also shown. The blue and yellow regions represent the charge accumulation and depletion, respectively. The zero of energy is at E_F shown by the dashed green line.

DOS are also shown in Fig. 3.1(b). The electronic properties of C_3N strongly depends on adatom coverage. For 1H/C_3N (3.1%), there is a metallic behavior unlike pure C_3N. As the H coverage increases to 6.2%, the metallic behavior remains with an increased density of states at the Fermi level. For further increase of H coverages to 9.3%, there is still metallic character, while increasing the H coverage to 12.5%, we see from the electronic band structure that two non-trivial band gaps appear, with values of 30 and 65 meV, together with two Dirac-points around E_F. This results in a semiconductor-to-semimetal transition. For the coverages of 3.1, 6.2, 9.3 and 12.5%, there is no net spin (↑ minus ↓) i.e. no magnetic moment is induced. The tunable properties of functionalized C_3N with H atom coverage may have potential applications for the development of nanodevices.

Similar to H atom adsorption, we have considered four coverages of O adsorption at the most stable T_C-site on C_3N, as shown in Fig. 3.2. Coverages of homogeneously arranged O atoms are 3.1% ($C_{32}N_8O_1$), 6.2% ($C_{32}N_8O_2$), 9.3% ($C_{32}N_8O_3$) and 12.5%

($C_{32}N_8O_4$). We assume that the so-called epoxy group is formed at each adsorption site in these geometries. The optimized atomic structures of O/C_3N for the considered coverages are shown in Fig. 3.2(a). We find that the optimized lattice constant increases with O atom coverage due to charge transfer from C_3N to the O atoms (due to the large electronegativity of O), and the formation of epoxy groups at the C-N and C-C bonds. The C_O-O bond length for an O atom is 1.12 Å, indicating that O is chemically adsorbed on C_3N. The C-C and C-N bond lengths are elongated to 1.5 and 1.5 Å and the O-C_O-C angles are in the range of 110 °, displaying the characteristics of sp^3 hybridization. Similar to H adsorption, the C_O atom moves out of the base plane of C_3N, and induce a buckling of 0.64 Å. The corresponding band structures and DOS for the four considered O/C_3N systems with different O coverages are shown in Fig. 3.2(b). We see from the electronic band structures that the width of the energy band gap becomes narrow and decreases with increasing O/C ratio, reflecting the localization of electronic states that is, the decrease of interaction between C and N atoms in C_3N with the increase of O coverage. For 1O/C_3N (3.1%), we see a striking difference compared to pure C_3N, although also a very small indirect band gap. For 2O/C_3N (6.2%) the structure has a band gap of 0.12 eV, while 3O/C_3N (9.3%), becomes a metal. For the coverages of 3.1, 6.2 and 9.3%, there is no net spin in the ↑ minus ↓ channels. Interestingly, we see that 4O/C_3N, for 12.5% coverage, has an induced magnetic moment of 0.17 μ_B in the ground state. These result shows that the electronic and magnetic properties of C_3N depends on the O absorbed concentration.

3.2.1 Adsorption two H and O atoms

We next consider the adsorption of a second H or O atom on the opposite side of C_3N. Three two-side configurations are considered, including $H_t - H_b$, $O_t - O_b$ and $H_t - O_b$. The optimized structures, top and side views, are shown in Figs. 3.3(a-c). After optimization of the structures, we find that the stable structures have a very slight buckling. The structural parameters of the optimized structures, including the C-C and C-O bond lengths, are shown in Figs. 3.3(a-c). For all structures, the H and O atoms are located at the top site of a C atom, and form a single covalent bond between C_H-H and C_O-O. The C_H-H and C_O-O bond lengths are 1.118 ($H_t - H_b$), 1.355 ($O_t - O_b$) and 1.119/1.356 ($H_t - O_b$) Å, indicating that these atoms are chemically adsorbed on C_3N. For $H_t - H_b$, the C-C and C-N bonds are elongated to 1.502 and 1.504 Å and the H-C_H-C angle is 110 °, displaying the character of sp^3 hybridization. The C_H and C_O atoms move out of the base plane of C_3N and induce a buckling of 0.64 Å. In the case of, $H_t - O_b$, the C-C and C-N bonds is elongated to 1.502 and 1.504 Å showing the character of sp^3 hybridization. The C_H and C_O atoms move out of the base plane of C_3N and induce a buckling 0.64 Å. These results indicate that the stronger orbital hybridizations in C-O bonds significantly

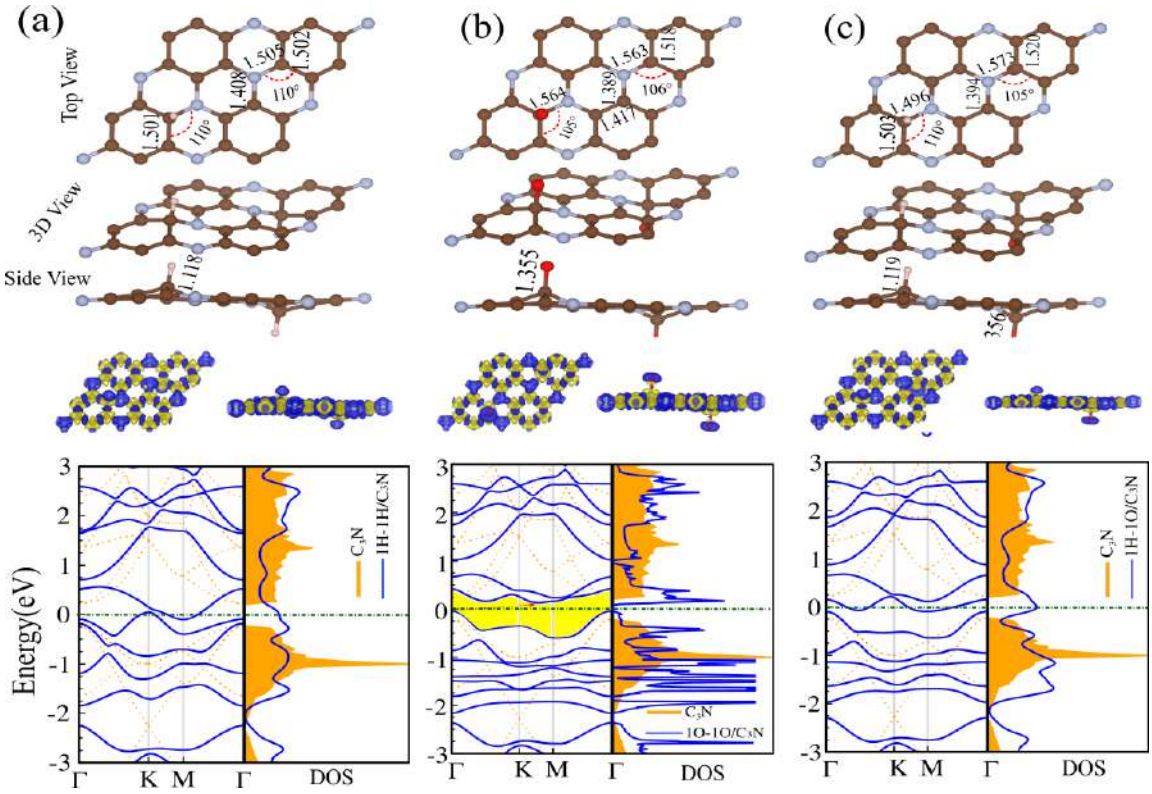

Figure 3.3: Optimized structures, electronic band structure and DOS of H and O atoms adsorbed on two sides of C_3N for (a) $H_t - H_b$, (b) $O_t - O_b$ and (c) $H_t - O_b$. Difference charge densities are also shown, and for (b), the charge density of the highest occupied and lowest unoccupied molecular orbitals (HOMO and LUMO) are shown as insets. The zero of energy is at E_F as shown by the dashed green line.

reduce their lengths and even weaken the C-C bonds. There exists a partial transformation from sp^2-type covalent bond character in pure C_3N into sp^3-type covalent bond character. The above-mentioned rich geometric structures lead to diverse electronic properties.

To gain insight into the bonding character, the difference electron charge density is shown in Figs. 3.3(a-c). The blue and yellow regions represent electron accumulation and depletion, respectively. It can be seen that electrons are accumulated on the H and O atoms, whereas the majority of electron depletion is on C_3N, which shows there is partial electron transfer from C_3N to the adsorbates, and the formation of chemical bonds. When H and O atoms are adsorbed on both sides of C_3N, the energy dispersion relations exhibit dramatic changes. The band structure and corresponding DOS for the different configurations of H and O atoms are shown in Figs. 3.3(a-c). The electronic properties of

these structures strongly depend on the type of the double H and O adsorption site. We can see that the $H_t - H_b$ geometry exhibits metallic characteristics with the Fermi level, E_F, crossing the bands, whereas the $O_t - O_b$ structure is a semiconductor with a indirect band gap of 0.2 eV, the VBM and CBM located at the Γ point. We see that in the case of $H_t - O_b$, the electronic states are particularly modified and the structure is a nonmagnetic metal. The strong interaction between H and O atoms is also reflected by the broad peaks in the PDOS.

3.3 Effect of H atom clusters: Ortho, Meta and Para configurations

To understand the formation of H clusters (hydrogenated domains) on C_3N, we investigate the adsorption of a second H atom at different sites at close distances to the first. When a H atom is adsorbed on top of a surface C atom, the second H atom can adsorb on six possible relevant sites on the hexagonal C ring. The closest pairing, most commonly labeled as the "ortho" pair is where the H atoms are directly bonded to adjacent C atoms. The next closest pairing is labeled as the "meta" pair, and finally the next next closest pairing is labeled as the "para" pair. The optimized atomic structure and corresponding structural parameters for six types of two-H clusters/pairs on C_3N, namely, one-side ortho, one-side meta, one-side para, two-side ortho, two-side meta and two-side para, are shown in Fig. 3.4(a). We see that the H-C bonds are approximately vertical to the C_3N surface and the range of the C-H bond lengths is $\sim$ 1.113-1.125 Å. Adsorption of a single H atom yields 0.05 Å buckling of the C_3N lattice, and adjacent C atoms forming C-H bonds in these configurations are buckled by a similar small amount of $\sim$ 0.03 Å. The difference charge densities shown in Fig. 3.4(b) indicate that there is formation of chemical bonds for all configurations, and clearly explains the sp^3-type covalent character of the C-H bonds. We see a charge accumulation about the H and N atoms, whereas a depletion of electrons in C_3N, showing that there is charge transfers from C_3N to the H atoms. In order to help to visualize the effects of the adsorbed H clusters on C_3N, we also performed STM image calculations. The same set of simulation parameters were used for all the structures investigated. The simulated STM images for the three one-sided configuration, namely ortho, meta and para, are shown in Fig. 3.4(c). The atomic structure, with C (gray balls), N (blue balls) and H (white balls) atoms, is overlayed. From the predicted STM images, it is straightforward to recognize and correlate them with the corresponding atomistic structure. The H atoms around the adsorption site correspond to the bright spots.

We now discuss the surface electronic states in the presence of adsorbed H pairs, which is important for the identification of adsorbed H structures, and for providing fundamental

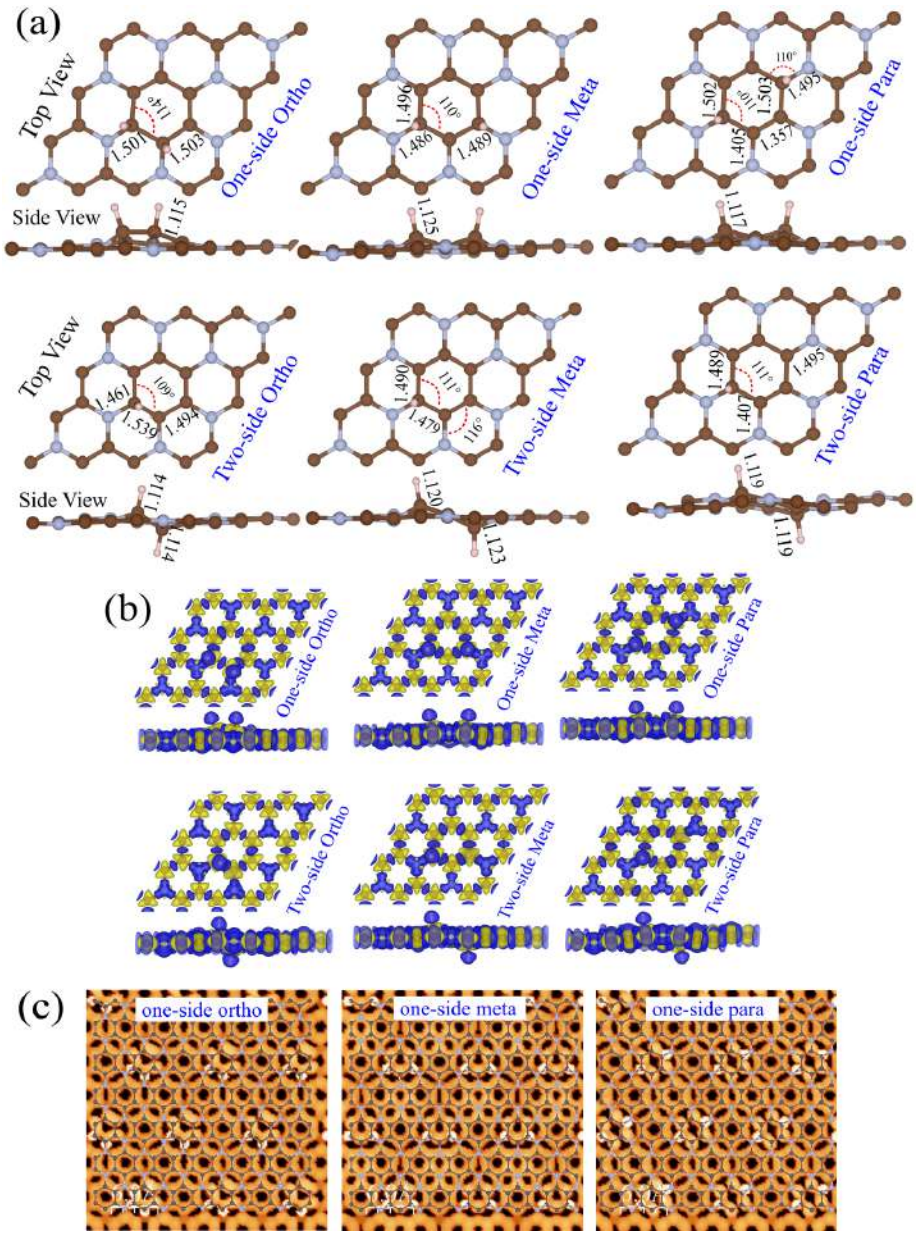

Figure 3.4: (a) Optimized atomic structures of two H atoms adsorbed on C_3N. (b) Difference electron charge densities and (c) simulated STM images of three different configurations including one-side ortho, meta and para. Blue and yellow regions represent the charge accumulation and depletion, respectively.

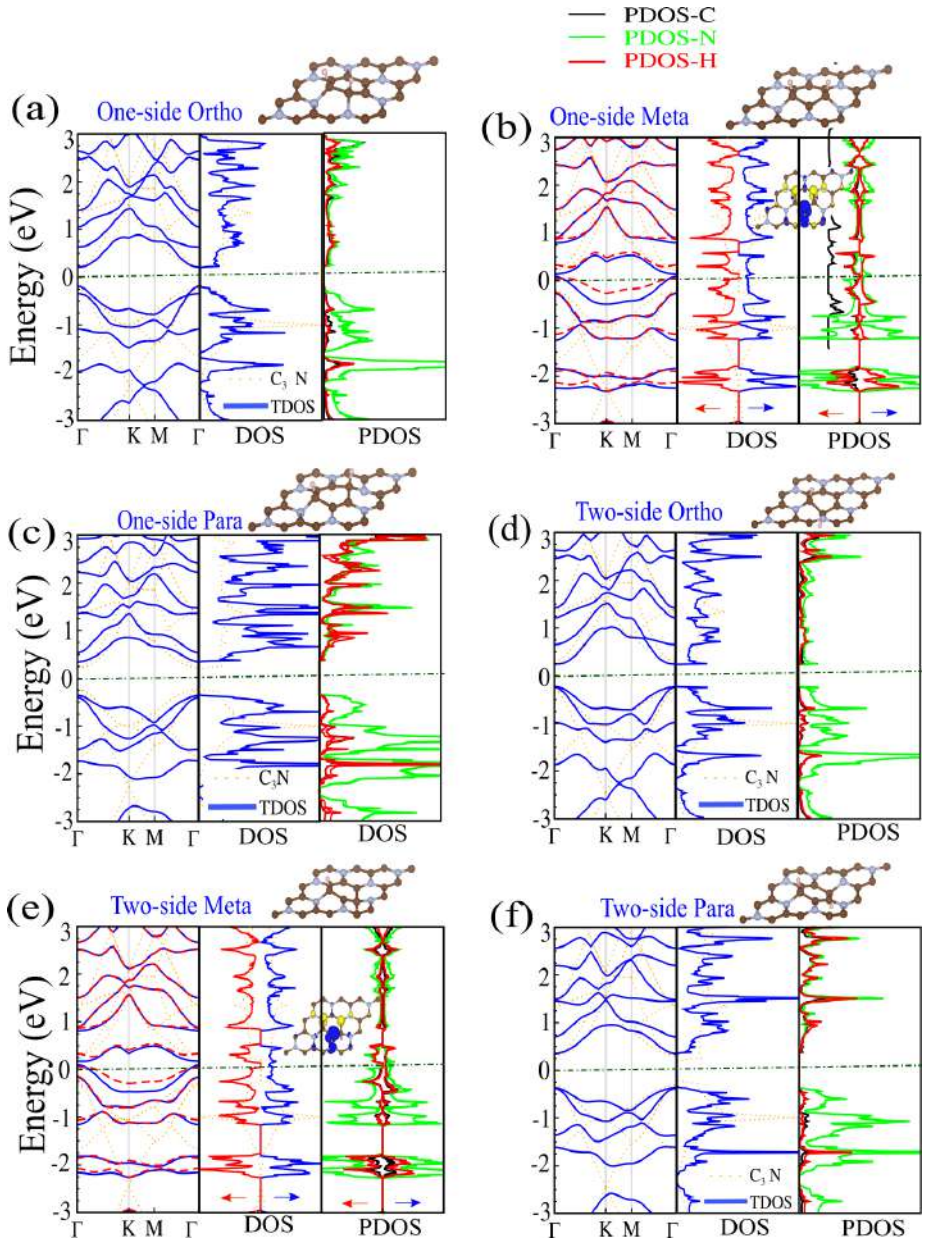

Figure 3.5: Electronic band structure, DOS and PDOS for the six different H pair configurations including (a) one-side ortho, (b) one-side meta, (c) one-side para, (d) two-side ortho, (e) two-side meta and (f) two-side para. The zero of energy is at E_F and shown by the dashed green line.

knowledge on how C_3N electronics can be tailored by H adsorption. The electronic band

structure, DOS and PDOS for the six configurations of two-H atom clusters adsorbed on C_3N (namely one-side ortho, one-side meta, one-side para, two-side ortho, two-side meta and two-side para) are shown in Figs. 3.5(a-f). It can be seen that the one-side and two-side ortho shows a semiconducting character, with a narrow band gap at Γ (0.37/0.47 eV). The one-side and two-side para structures are also nonmagnetic with a direct band gap 0.7 eV and the VBM and CBM is located at the Γ point. The one-side and two-side meta structure induces impurity states around E_F which mainly originate from states of the adsorbed H pair. Interestingly, we find these systems exhibit a magnetic moment of $1\mu_B$ (Figs. 3.5(b,e)). It can be seen that the VBM and CBM of the one-side and two-side meta structure is due to the hybridization of C- and N-p orbitals. Also, the VBM of one-side and two-side para is due to the hybridization of N and H orbitals, and the CBM is due to the hybridization of C and H orbitals. Our results show that the electronic and magnetic structure are significantly affected by the configuration of two-H atom clusters and the systems can exhibit diverse electronic characteristics from metal to semiconductor and to inducing magnetism in some configurations.

3.3.1 Effect of H adsorption with different distances

The interaction between the adsorption of two H atoms on C_3N as a function of the distance between them is important in order to understand the coverage dependence of the electronic properties. We consider two H atoms on the C_3N surface using a (4×2) surface unit cell and investigate the electronic properties as a function of the separation between

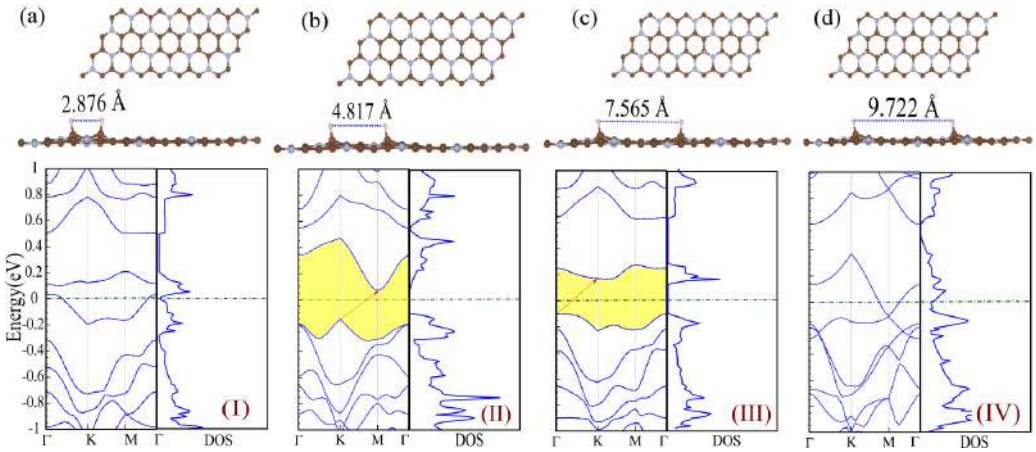

Figure 3.6: Optimized atomic structures, electronic band structure, DOS and PDOS of two H atoms adsorbed on the same side of C_3N for four different configurations, namely, (a) I, (b) II, (c) III and (d) IV for increasing H-H distance. The zero of energy is at E_F shown by the dashed green line.

them. The corresponding supercell contains 48 C, 16 N and 2 H atoms with (x, y) lattice constants of 19.44 and 9.72 Å, respectively. The distances considered between the H atoms are: I (2.876Å), II (4.817Å), III (7.565Å) and IV (9.722Å). All of the atoms are fully relaxed. The resulting optimized atomic structures, electronic band structure and DOS are shown in Figs. 3.6(a-d). It can be seen that the electronic and magnetic properties change with H-H separation. The (I) configuration exhibit metallic character with the Fermi level crossing the bands. The (II) configuration is a indirect semiconductor with 0.25 eV band gap, and the VBM and CBM located at the K and M points, respectively. The (III) configuration is a semiconductor with a narrow indirect band gap of 0.23 eV.

3.3.2 Effect of H adsorption with 0.125% concentration

It is known that the introduction of electrons into a system pushes the E_F up into the CB so that the E_F may approach the singularity point which may be associated with ferromagnetism. We have considered four structures for a 0.125% one-sided uniform coverage of H atoms on $(n \times m)$ supercells of C_3N. The coverages of homogeneously arranged H atoms are $C_{96}N_{32}H_4$, $C_{192}N_{64}H_8$, $C_{214}N_{72}H_9$ and $C_{240}N_{80}H_{10}$, and are shown in Fig. 3.7(a). For the first structure, we have constructed a (4×4) supercell of 132 atoms ($C_{96}N_{32}H_4$) to study a series of H adsorbed C_3N systems (0.125%). The H atoms are adsorbed in such a way that the distance between them is 9.722 Å. The $C_{96}N_{32}H_4$, exhibit a metallic character and induces a negligible magnetic moment. Smaller and larger supercells of H/C_3N systems are studied to determine the role of the size of the supercell on the electronic and magnetic properties. The spin-polarized electronic band structure for 0.125% H adsorbed C_3N is shown in Fig. 3.7(b). For $C_{192}N_{64}H_8$, it exhibits metallic characteristics with a small magnetic moment of $4 \times 10^{-4}\mu_B$. With increase of supercell size, the magnetic moment increases slightly, and for $C_{214}N_{72}H_9$, the magnetic moment becomes $7 \times 10^{-3}\mu_B$, and the $C_{240}N_{80}H_{10}$ (10×2 structure with 330 atoms) exhibits a magnetic moment of $2 \times 10^{-2}\mu_B$ in the ground state. Thus, our calculations for $C_3NH_{0.125}$ using the large supercells, show that the hydrogenated material becomes slightly ferromagnetic. The electronic band structure for the 0.125% one-sided uniform coverage structures of H atoms adsorbed on each $(n \times m)$ supercell of C_3N ($C_{96}N_{32}H_4$, $C_{192}N_{64}H_8$, $C_{214}N_{72}H_9$ and $C_{240}N_{80}H_{10}$), are shown in Fig. 3.7(b). Compared to the electronic band structure of C_3N, $C_3NH_{0.125}$ becomes a metal with impurity states appearing near E_F. These impurity states arise from the chemical adsorption of H atoms and their nearest-neighbor C atoms which change from sp^2 to sp^3 hybridization. Concominantly, there are electrons transferred from C_3N to the H atoms. The $\uparrow$ and $\downarrow$ spin channels are not symmetric at the Fermi energy level, which gives rise to small associated magnetic moments as shown in Fig. 3.7(c). The blue and yellow regions represent the $\uparrow$ and $\downarrow$ spin channels, respectively.

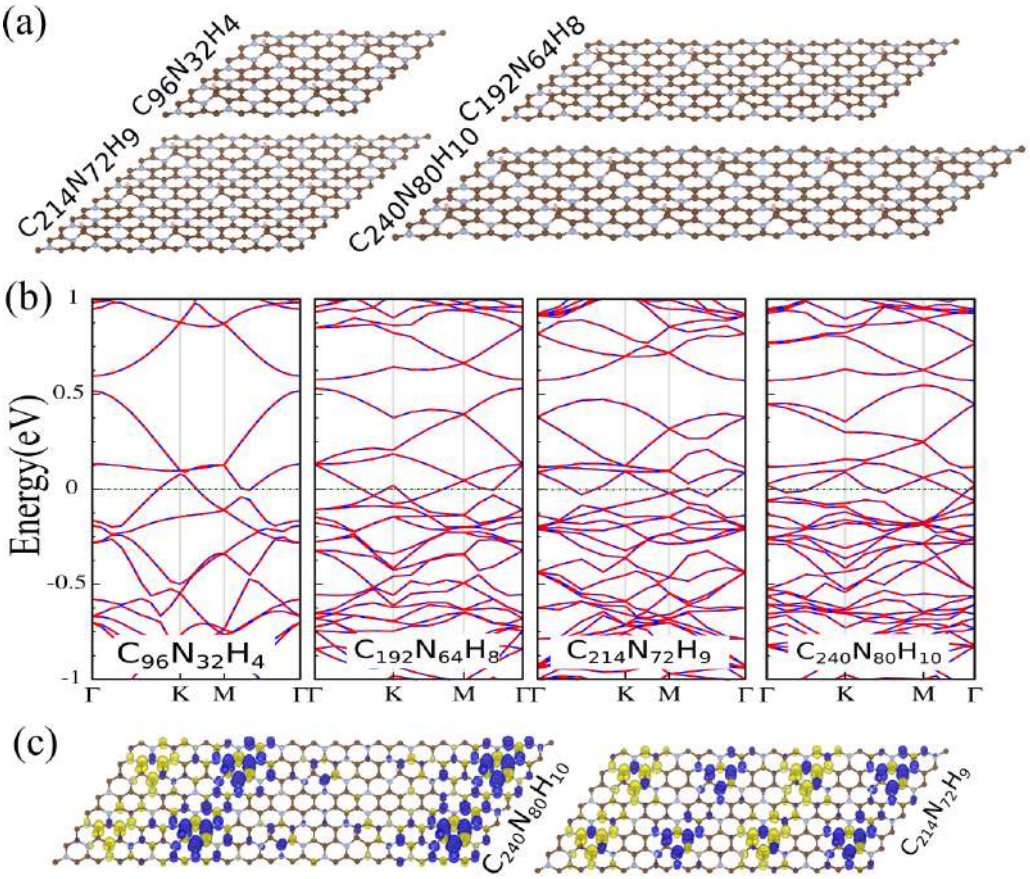

Figure 3.7: (a) Optimized structures (b) electronic band structure, for a 0.125% one-sided uniform coverage of H atoms adsorbed on each ($n \times m$) supercell of C_3N: $C_{96}N_{32}H_4$, $C_{192}N_{64}H_8$, $C_{214}N_{72}H_9$ and $C_{240}N_{80}H_{10}$. The zero of energy is set at E_F shown by the dashed green-point line. (c) Difference spin density. Blue and yellow regions represent the $\uparrow$ and $\downarrow$ spin channels, respectively.

3.4 Functionalization of C_3N with H, O and F atoms

Functionalization by the adsorption of atoms is a feasible method to modify the electronic and magnetic properties of 2DMs. Below, we investigate the structural and electronic properties of semi and full coverages of H, O and F atoms on C_3N in the chair-like conformation. For this we fully optimize the atomic structures.

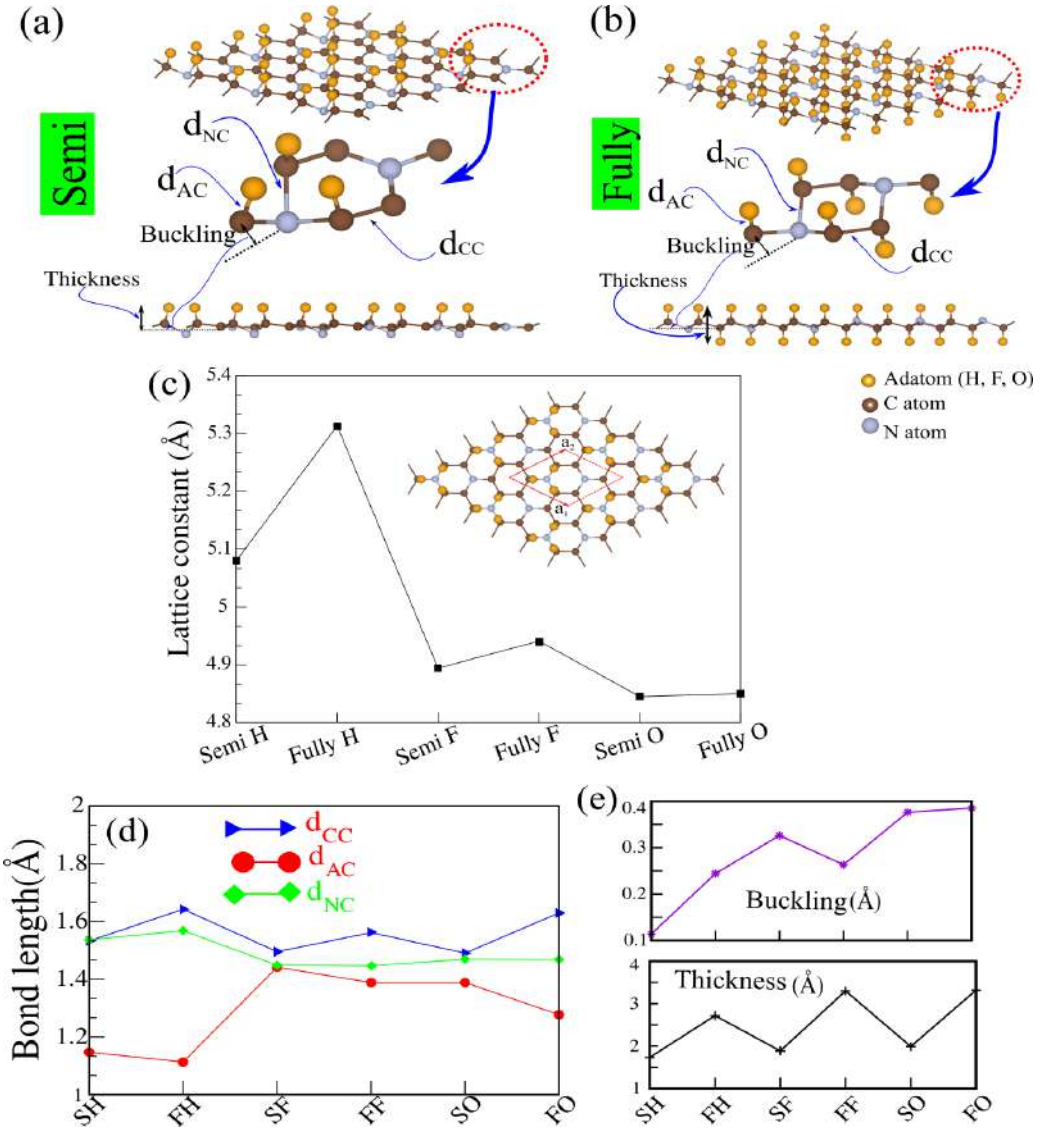

Figure 3.8: Schematic atomic structures of (a) semi and (b) fully functionalized (hydrogenated, fluorinated and oxidized) C_3N in the chair-like conformation. (c-e) Variation of structural parameters including (c) lattice constant, (d) bond lengths (e) and buckling together with the thickness of the layers for the different structures.

3.4.1 Structure properties

After optimization we find that these adatoms are adsorbed on C atoms with bonds approximately perpendicular to the C_3N plane. Here, SH- and FH-C_3N are the abbreviations for

semi hydrogenated C_3N and fully hydrogenated C_3N, respectively. The relaxed structures and corresponding atomic parameters such as lattice constant, the bond lengths between C-(H,F,O), N-C, C-C and buckling parameter for SH-, SO- and SF-C_3N, are shown in Figs. 3.8(a,b) schematically. Variation of the lattice constant, bond length, buckling and thickness layers, are shown in Figs. 3.8(c-e). We see that for C_3N, the lattice constant and the bond lengths between C-(H,F,O), N-C and C-C are slightly increased upon semi and full coverage. In general, the C-C and C-N bond lengths without SH-, SO- and SF-C_3N are smaller than that between the C and N atoms with one or both C and N atoms bonded to the H, O and F atoms (C-$C_{H,O,F}$ or $C_{H,O,F}$-$C_{H,O,F}$). For example, for SH- and FH-C_3N there is a slight increase of the lattice constant from 4.861 Å in pristine C_3N, to 5.080 and 5.313 Å, respectively. The increase in lattice parameter is due to the increase in bond lengths, which is changed from 1.4 to 1.5 Å (for SH-C_3N) and 1.6 (for FH-C_3N) Å. For SH-C_3N, the C_H-H bond length is 1.147 Å. The values of rumpling for SH- and FH-C_3N are 0.114 Å and 0.244 Å, respectively.

3.5 Electronic properties

We now consider the atomic and electronic structure of the semi coverage of C_3N with H, O and F atoms in the chair-like conformation. After relaxation, we see that the H, O and F atoms are adsorbed on the C atoms with bonds oriented approximately normal to the both sides of the C_3N plane. The optimized structures and corresponding atomic parameters such as lattice constant, the bond lengths between C-(H,F,O), N-C and C-C and buckling parameter for SH-, SO- and SF-C_3N, are shown in Figs. 3.9(a-f). For C_3N, the lattice constant a plus the bond lengths between C-(H,F,O), N-C and C-C are slightly increased on SH-, SO- and SF-C_3N. In general, the C-C and C-N bond lengths adsorption, are smaller than those between the C and N atoms with one or both C and N atoms bonded with H, O and F atoms (C-$C_{H,O,F}$ or $C_{H,O,F}$-$C_{H,O,F}$). We find that SH and FH-C_3N slightly enlarge the lattice constant from 4.861 for C_3N, to 5.080 Å and 5.313 Å, respectively. The increase of lattice parameter is due to the increase in the bond length, which changes from 1.4 to 1.5 Å for SH-C_3N. For SH-C_3N, C_H-H bond length is 1.147 Å and bond angle between C_H-N-C_H, N-C_H-C and C-C_H-C are 105, 113 and 115°, respectively. The values of rumpling for the SH- and FH-C_3N structures are 0.114 Å and 0.244 Å, respectively. In general, the C-C and C-N bond lengths without hydrogenation are smaller than those between the C and N atoms with one or both C and N atoms bonded to H atoms (C-$C_{H,F,O}$ or $C_{H,F,O}$-$C_{H,F,O}$). For the FH-C_3N, C_H-H bond length is 1.147 Å and bond angles between C_H-N-C_H, N-C_H-C and C-C_H-C are 105, 113 and 115 ° ,respectively. The values of rumpling for FH-C_3N is 0.244 Å. The difference charge density are shown in top of panels

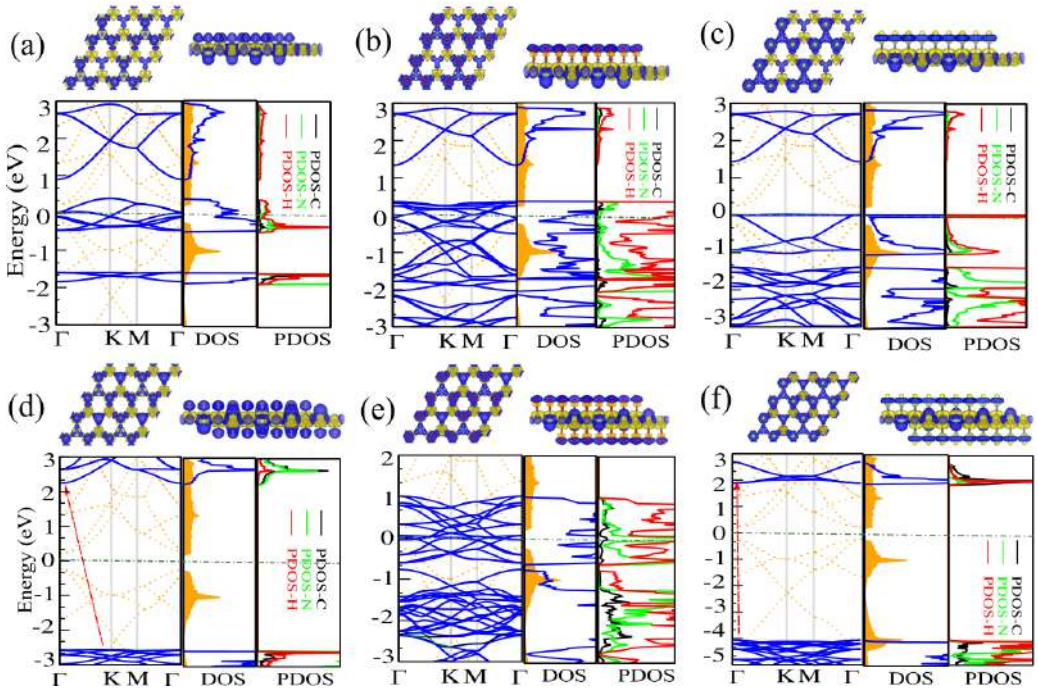

Figure 3.9: Electronic band structure, DOS and PDOS of (a) semi-hydrogenated, (b) semi-fluorinated, (c) semi-oxidized, (d) fully-hydrogenated, (e) fully-fluorinated and (f) fully-oxidized in the chair-like conformation of C_3N. The difference charge density is given in the top of the panels. The blue and yellow regions represent the charge accumulation and depletion, respectively. The zero of energy is at E_F as shown by the dashed green line.

in Figs. 3.9(a-c). The high charge density around C bonded, H and N atoms projecting toward the C-N and C-H bonds indicate charge transfer from C to N and H atoms. In order to understand the effects of semi and full coverage on C_3N, we investigate the electronic properties.

The electronic band structure corresponding to the DOS and PDOS of SH-, SO- and SF-C_3N, are shown in Figs. 3.9(a-c). Our results show impurity states appear around E_F, and induce metallic properties in the former two systems. In comparison with pure C_3N, the band structure is greatly changed due to the functionalization. For SH-, SO- and SF-C_3N, all the H, O and F atoms are adsorbed on one side, which naturally results in a repulsion among the H,O and F atoms. This results in a shift of most of the C-p_z orbital type bands and this further causes the crystal to expand. It becomes evident from comparison that for SH-C_3N, the N-p_z and H-s orbitals are shifted toward E_F. In fact, the

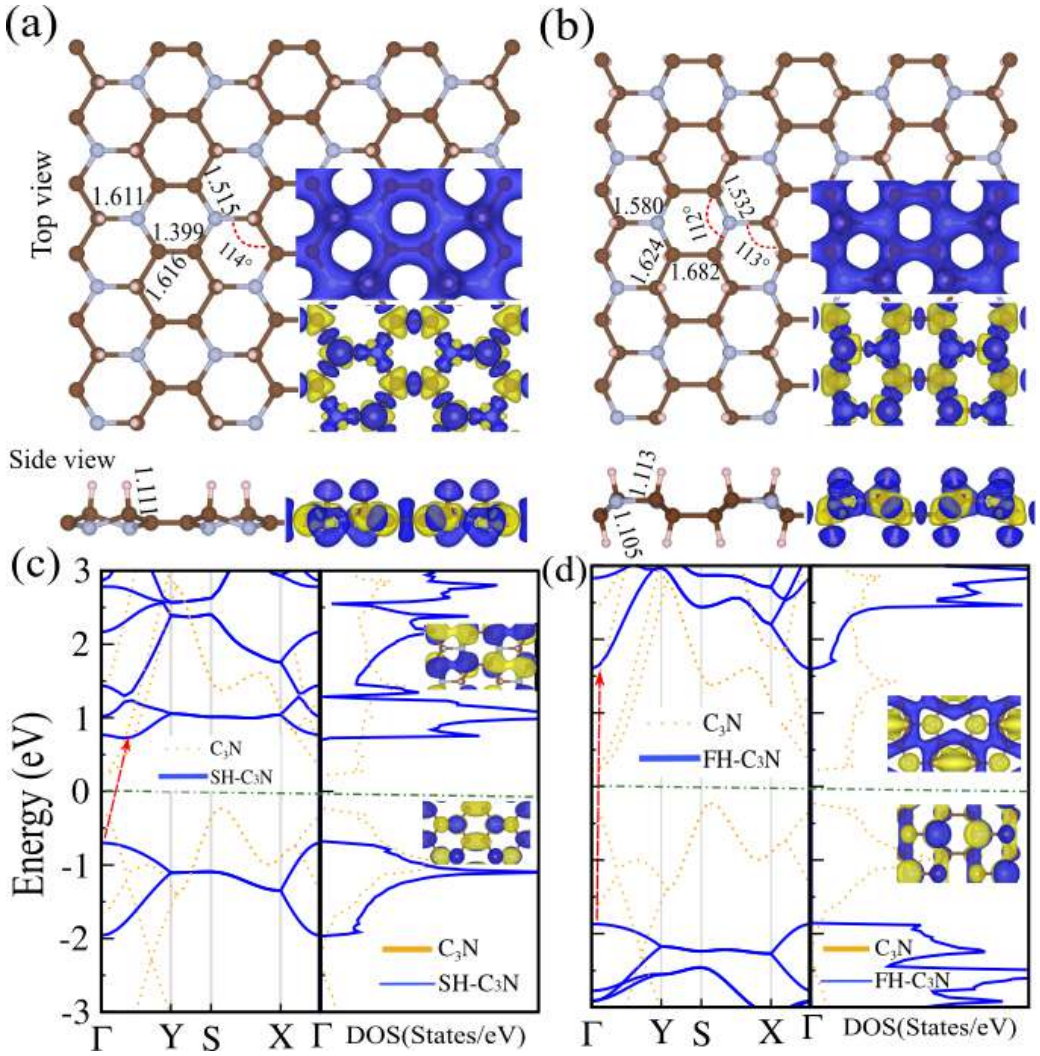

Figure 3.10: Optimized atomic structures, electronic band structure, DOS and PDOS of boat-like conformation for (a,b) semi-hydrogenated, (c,d) fully-hydrogenated of C_3N. The difference charge densities indicated in top of panels. The blue and yellow regions represent the charge accumulation and depletion, respectively. The zero of energy is set at E_F shown by the dashed green-point line.

contribution from N-p_z orbitals is almost as large as that of C-p_z orbitals. The electronic band structure, DOS and PDOS for full coverage of C_3N are shown in Figs. 3.9(d-f). The FH- and FF-C_3N, exhibits a insulator, with very large band gaps of 4.8 eV and 5.8 eV, respectively, while the FO-C_3N structure is metallic.

3.5.1 Smei and fully hyrogenation with boat-like conformation

We next consider the boat-like conformation/structure to investigate the effects of H coverage on C_3N. The optimized structures and geometrical parameters (bond lengths, bond angles) of semi and fully hydrogenated-C_3N are shown in Figs. 3.10(a,b). The lattice constant of C_3N and the C-C and C-N bond lengths are slightly increased upon semi and full hydrogenation and the C-C bond length is the largest for FH-C_3N, however the buckling parameter is significantly increased. We see that the C-C and C-N bond lengths are increased from 1.403 to 1.616 Å (C-C bond) and 1.404 to 1.611 Å (C-N bond), respectively. The lattice constant of FH-C_3N is 9.10 Å and the bond lengths between C and H atoms (C_H-H bond) in SH-C_3N are 1.111 Å, larger than those in FH-C_3N, 1.105 Å. The bond angle between N-C_H-C for SH-C_3N is 114°, also H atoms not sitting directly above the C atoms, whereas the C_H-H bond is approximately perpendicular to the C_3N plane. The geometry of hydrogenated C_3N is buckled and the range of buckling constants for SH-C_3N is 0.229 Å and for FH-C_3N are 0.373 Å for C bonded toward up and 0.260 Å for C bonded toward down, respectively. The difference charge density are shown in Figs. 3.10(a-c). We see a high electron density around C bonded and N atoms. The band structure, DOS of SH- and FH-C_3N with boat-like conformation, are shown in Figs. 3.10(c,d). Our results show that the boat-like conformation of SH-C_3N becomes an indirect semiconductor with a 1.4 eV band gap, while the FH-C_3N exhibits a direct band gap of 3.45 eV. C_3N without hydrogenation is a typical sp^2 bonded system. When a H atom is adsorbed on a C atom, sp^3 hybridized bonds form, leading to a distortion of C_3N and results in the opening of a band gap.

3.6 Effect of vacancy defect

The synthesis of large C_3N sheets having a high-density of nanoscale holes or multiple C vacancies is another landmark in controlling the electronic properties of C_3N. Controllable change of the electronic and magnetic properties of C_3N through holes and vacancies can potentially be utilized for different technological applications. To study the effect of such defects on the electronic and magnetic structure, we consider 1H-, 2H and 3H-vacancies in one-side of FH-C_3N. Our calculations show that ferromagnetic ordered states form, where the larger the number of H vacancies, the larger the magnetic moments. The optimized atomic structures for the chair-like conformation of fully hydrogenated C_3N with H vacancies (by removing one, two and three H atoms), are shown in Figs. 3.11(a-c). The difference charge density is shown, where it can be seen that there is a charge accumulation in the region of the H vacancies, as well as on the neighboring C/N atoms. The band structure and corresponding DOS are shown in Figs. 3.11(a-c). We can see that the

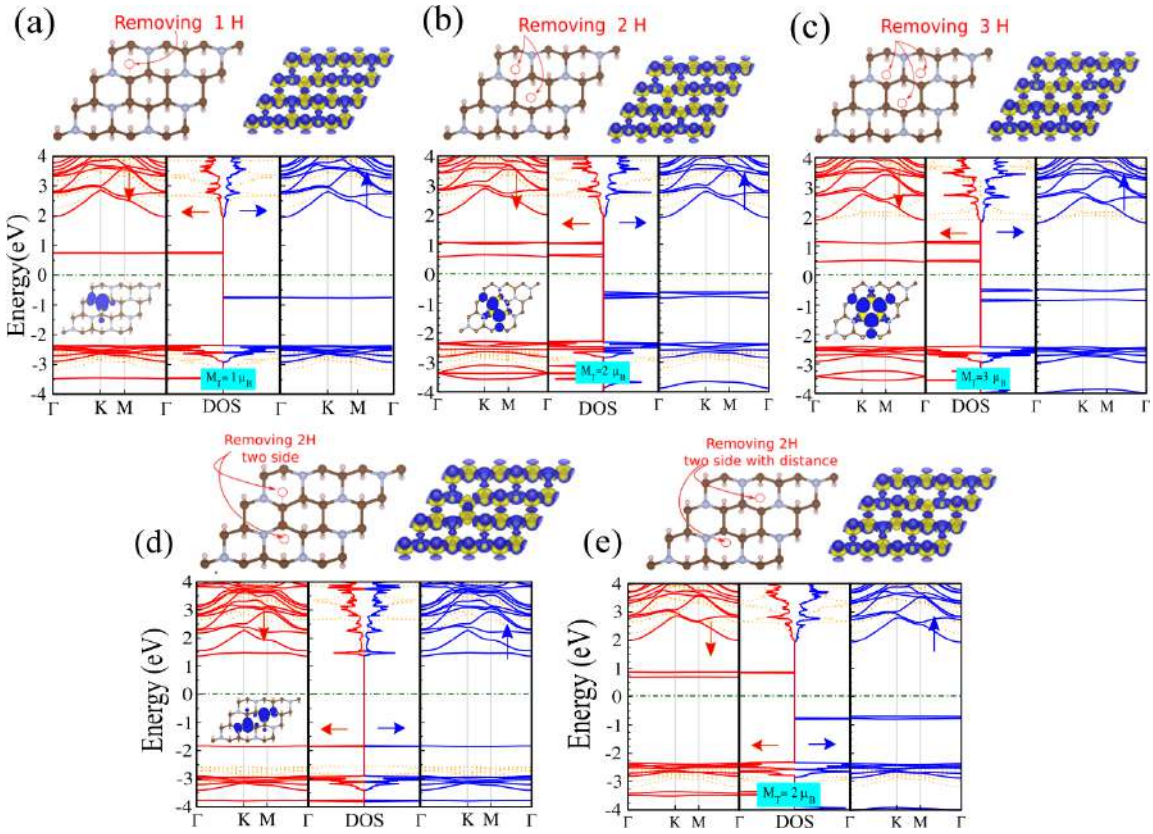

Figure 3.11: Relaxed atomic structures, band structure and DOS of fully hydrogenated C_3N with the boat-like conformation for the (a) single vacancy H formed by removing one H atom and (b) a double vacancy H structure by removing two H atom, from one side. The difference spin density is shown as inset. The blue and yellow regions represent the ↑ and ↓ spin channels, respectively. The difference charge densities are also indicated at the top of the figures. The blue and yellow regions represent the electron accumulation and depletion, respectively. The zero of energy is set at E_F shown by the dashed green-point line.

energy band dispersion is modified by removing the H atoms. Each 1H-vacancy leads to a half-filled sp^3-like orbital on the C_3N surface and the band gap decreases as the vacancy defect states are located in the band gap. FH-C_3N is nonmagnetic insulator with a large band gap of 4.8 eV. By introducing a single H vacancy on one-side, the band gap decreases to 4.3 eV due to the defect states that appear in the gap. Each 1H-vacancy, induces a 1 μ_B magnetic moment, as shown in Fig. 3.11(a). The 2H and 3H-vacancy structures also exhibits a semiconducting nature with a reduced band gap compared to C_3N. The magnetic moment enhanced with increase of number of H atoms removed. In particular, we find

that the magnetic moments are 2 and 3 μ_B, respectively. These induced magnetic properties in C_3N may be useful for future data storage and spintronics applications. The spin density shows that the unpaired spin states are located in the region around the vacancy. Upon removing one H atom (the 1H-vacancy) the original sp^3 bonding is re-transformed into planar sp^2 bonding and perpendicular p_z orbitals. At the vacancy, the one electron accommodated in the dangling p_z orbital becomes unpaired and induces the 1 μ_B magnetic moment. Therefore we find that FH-C_3N with the considered H vacancies yield interesting magnetic properties (ferromagnetic domains with large net magnetic moments) which are promising for nanoscale spintronic devices and useful for future data storage applications. These properties may also enable the engineering of desired electronic characteristics.

We also consider double H-vacancies. The optimized atomic structures of FH-C_3N formed by removing two H atoms from first and third neighbor atoms, from two sides, are shown in Figs. 3.11(d,e). The corresponding electronic band structure and DOS are also shown. We can see that there is no spin splitting of the band structure for the 2H-vacancy FH-C_3N from first neighbor atoms. In comparison with the electronic band structure of FH-C_3N, the the 2H-vacancy FH-C_3N remains a semiconductor with the introduction of impurity states in the gap. These impurity states, comes from the H-vacancy and their nearest-neighbor C atoms. The 2H-vacancy structure formed from third neighbor atoms, is also a semiconductor, but with a smaller band gap of 2.8 eV. The $\uparrow$ and $\downarrow$ spin channels are not symmetric which results in an induced magnetic moment of 2 μ_B. Our results thus show that H vacancy domains on FH-C_3N, which is the hydrogenated counterpart of C_3N, exhibit induced states in the band gap, which are not present for defect-free FH-C_3N. This furthermore demonstrates that FH-C_3N surfaces may result in a ferromagnetic states, and that the magnetism depends on the concentration of the H vacancies, as well as their distribution on the surface.

3.6.1 Effect of vacancy defect in boat-like conformation

In the following we examine the effect of H vacancies on SH-C_3N with the boat-like conformation. The optimized atomic structures, band structure and DOS are shown in Figs. 3.12(a-d). We see from the difference charge density that there is accumulation of electron density in the region of the H-vacancy with neighboring C/N atoms, resulting in strong H-C and F-C bonds. Our results show that the boat-like conformation of SH-C_3N, is an indirect semiconductor with a band gap of 1.4 eV. For the 1H-vacancy SH-C_3N structure, there are defect states introduced into the band gap, but it is still semiconducting with a band gap of 0.2 eV. The VBM and CBM are located at the **Y** and Γ points, respectively, thus it is indirect. The spin density (difference between spin up and down electrons) are shown in Fig. 3.12(a). The unpaired electron at the unsaturated C site, leads to an induced

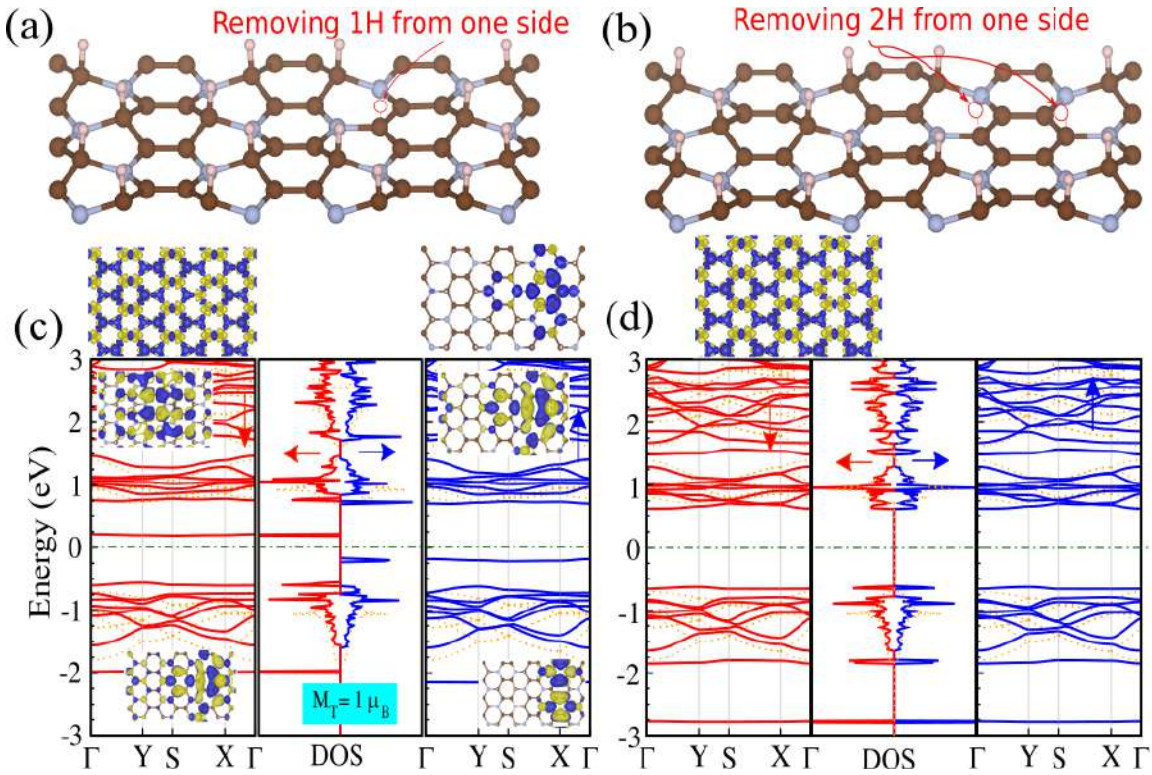

Figure 3.12: Relaxed atomic structures, band structure and DOS of fully hydrogenated C_3N with the boat-like conformation for the (a) single vacancy H formed by removing one H atom and (b) a double vacancy H structure by removing two H atom, from one side. The difference spin density is shown as inset. The blue and yellow regions represent the ↑ and ↓ spin channels, respectively. The difference charge densities are also indicated at the top of the figures. The blue and yellow regions represent the electron accumulation and depletion, respectively. The zero of energy is set at E_F shown by the dashed green-point line.

magnetic moment of 1 μ_B. For the 2H-vacancy SH-C_3N structure, we see from the band structure that its a semiconductor.

3.6.2 Simulated STM images and molecular dynamics simulations

In order to facilitate comparisons between theory and experiment, we present a simulated STM image of SH-C_3N that was discussed in the previous section as shown in Fig. 3.13(a). The overlayed structure represents the SH-C_3N repeating unit. From the STM image, it is straightforward to recognize and correlate features with the corresponding atomic structure. The atoms in the vicinity of the adsorbed H atoms exhibit the bright spots. The

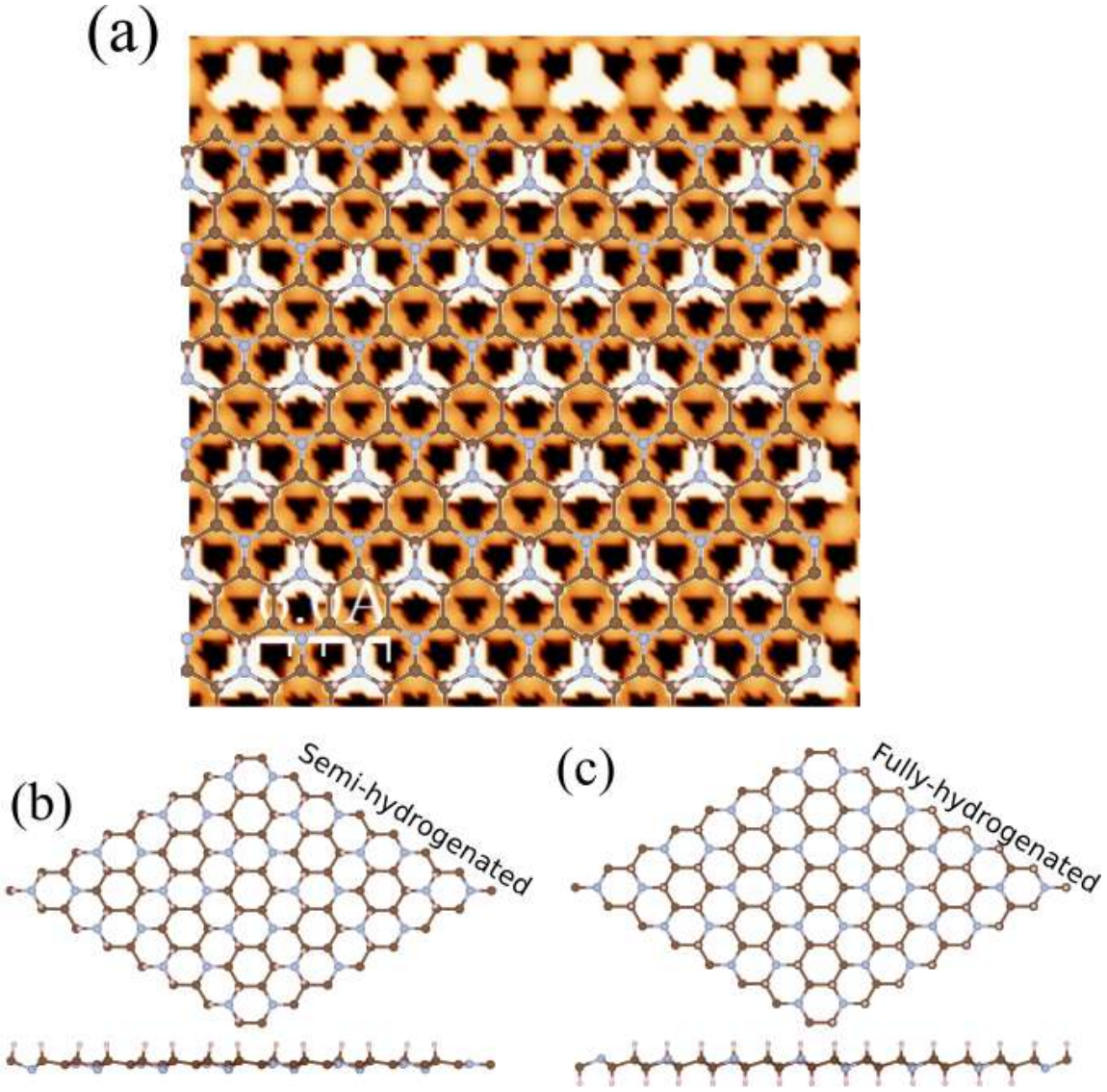

Figure 3.13: Simulated STM images of semi-hydrogenated C_3N. (b) Top and side views of snapshots for the relaxed structures of the C_3N at temperatures of 1000K, as obtained from molecular dynamics simulations.

thermodynamic stability of the SH- and FH-C_3N structures, is investigated by performing DFT molecular dynamics (MD) simulations. A large 3×3 supercell of SH- and FH-C_3N is used and we consider the effect of temperature at 1000 and 1500 K. Top and side views of snapshots for the relaxed structures of SH- and FH-C_3N at 1000K, are shown in Figs.

3.13(b,c). At 1000 K, SH- and FH-C_3N is predicted to maintain its original structure.

3.7 Conclusion

Using of first-principles calculations, we carried out extensive and systematic investigations into the atomic, electronic and magnetic structure of C_3N that has been recently synthesized. Functionalization by atoms is widely believed to be an effective way to improve and tune the properties of two-dimensional materials. We discussed the modifications that occur in the electronic structure of C_3N when adsorbed with different coverages of H and O atoms. Our results show that the electronic band gap values depend on the coverage, and also that the electronic and magnetic structure are significantly affected by the configuration of two-H clusters/pairs (ortho, meta and para) and the structures exhibit diverse electronic characteristics, from metal to semiconductor and to induce magnetism in some of the configurations. found We considered various large super cells for investigating magnetism in the $C_3NH_{0.125}$. The magnetic state results for $C_3NH_{0.125}$ exhibiting ferromagnetism. Furthermore, we investigated effects of semi and full functionalization (with two types configurations 'chair-' and 'boat-like') for adsorption of H, O and F atoms on C_3N and found how the electronic and magnetic properties C_3N are modified. From C_3N to semi-hydrogenated C_3N and then to fully-hydrogenated C_3N, the system changes from semiconducting to metallic and then to insulating. In addition, the electronic and magnetic properties of the resulting semi/fully hydrogenated C_3N can be further controlled by introducing H atoms vacancies, which also show diverse electronic properties including metallic, dilute-magnetic semiconductor and ferromagnetic insulator, depending on the side the H-vacancy is created and the vacancy concentration. Thus, creation of H vacancies is an effective method to control the magnetism in the semi and fully functionalization of C_3N. Finally, we studied the interaction of H and O atoms with zigzag and armchair C_3N nanoribbon. Adsorption of H can lead to considerable modifications in the electronic structure. Under these conditions, either the wide band gap of the C_3N nanoribbon with two difference types of zigzag and armchair, can be reduced or diminished and the C_3N nanoribbons becomes metal or semiconductor with an induced a magnetic moment. Furthermore, for exploiting the application possibilities of C_3N, we also investigate the effects of strain on the properties of hydrogenated C_3N. We showed that the band gap could be modulated with strain, and thus offering the potential to control this property. Overall, our detailed investigations show that there are unique opportunities to engineer the electronic properties of C_3N which may enable many useful potential technological applications in fields such as catalysis, energy storage and nanoelectronic devices.

CHAPTER 4

Topological defect and impurity atoms

Many approaches have been developed to modify the electronic and magnetic properties of 2DM. These methods involve substitution of atoms, defect engineering, surface functionalization and applying strain and/or electric field. Several computational studies have been conducted to investigate adatom and molecule adsorption on 2D monolayers [167**? ? ?** –173] and substitution of atoms [174–176]. Substitution of atoms into 2DM is of fundamental importance in order to tailor their electronic and magnetic properties, which are useful for numerous applications such as energy storage and conversion [177–179], sensing [180, 181] and nanoelectronics devices [176, 182–184]. The substitution of atoms into carbon nitride materials is of fundamental importance, enabling a wide range of applications by tailoring the electronic and magnetic properties [185–187].

In this chapter, by using first-principles calculations, we carried out a detailed investigation of how various point defects including vacancies (single and double vacancy), Stone-Wales (SW) and anti-site defects affect the structure of C_3N and its electronic and magnetic properties. We demonstrate the capability of defect engineering to alter the properties of C_3N from nonmagnetic semiconductor to a metal and/or a magnetic ground state. Furthermore, we present a detailed study of the effect of substitution of H, O, S, F, Cl, B, C, N, Si, P, Li, Na, K, Be, Mg, Ca and Al atoms on the electronic and magnetic properties of C_3N. We analyze the modification of the band structure of C_3N as the underlying mechanism for the changes in its properties. One of the goals is to show how introducing the above impurities turns the semiconductor of C_3N into a metal, half-metal, spin-glass semiconductor or dilute-magnetic semiconductor. The effects of charging and strain on

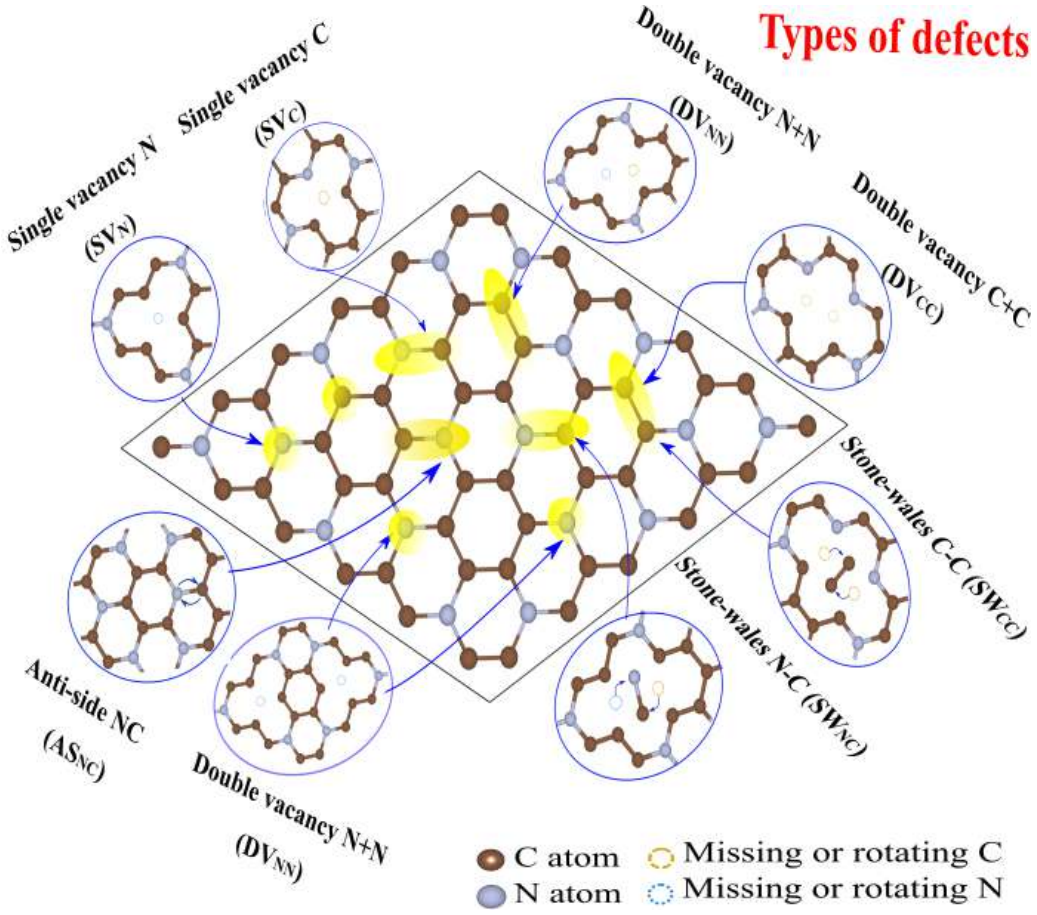

Figure 4.1: Schematic view of the different topological defects considered in the present paper: single vacancy with missing one C atom (SV_C), single vacancy with missing one N atom (SV_N), double vacancy with missing a pair of C (DV_{CC}), double vacancy with missing a pair of N (DV_{NN}), double vacancy with missing a pair of N and C (DV_{NC}), Stone-Wales (SW) and anti-site with exchange of the position of N and C atoms (AS_{NC}).

the substituted-C_3N are studied and we show how the band gap and magnetism can be modulated. The important point here is that a wide variety of electronic and magnetic properties, differing from pristine C_3N, emerge using the above methods.

4.1 Effect of topological defects

We investigate different topological defects in monolayer C_3N and in addition vacancies, Stone-Wales and anti-site defects. In order to investigate vacancies, we removed C and N atoms to produce single vacancy of the C atom SV_C or N atom SV_N, while for double vacancies, we remove C+C (DV_{CC}), N+N (DV_{NN}) and N+C (DV_{NC}) atoms respectively. For the Stone-Wales (SW) defect, we rotate a single C-C (SW_{CC}) or N-C (SW_{NC}) bond in C_3N by 90°, resulting in a structure with a pair of seven-membered and five-membered rings, respectively. For the anti-site defects, we replaced N with C atoms (i.e., exchanged the position of N and C atoms) (AS_{NC}). Typical defects are schematically shown in Fig. 4.1. With fully structural optimization, where all atoms are relaxed in all directions and calculations are performed using $2 \times 2 \times 1$ supercell of C_3N which contains 32 atoms (24 C and 8 N atoms).

4.1.1 Structure properties

In Fig. 4.5, we present the optimized structures with corresponding bond lengths and bond angles of SV_C and SV_N. The C and N atoms around the vacancy in C_3N undergo a Jahn-Teller distortion [146] and C and N atoms close to the vacancy site move towards each other to form C-C or C-N bonds. For the reconstructed SV_C (SV_N), two C atoms bond together to build a joint pentagonal and nonagonal (i.e., the 5-9 configurations). Two C atoms around the vacancy are approaching each other, so the C-C (N-C) bond lengths are changed to 1.597 (1.730) and 1.550 (1.560) Å, respectively, which differs from pristine C_3N (1.403 and 1.404 Å) (see Fig. 3). For SV_C, upon structural optimization the same symmetry and a planar structure of C_3N is found. In DV_{CC} case, we observed no deviation from the planar configuration upon structural relaxation and it exhibits a non-reconstructed structure, while DV_{NC} shows reconstructed structure and two C atoms bond together to build two pentagon and one heptagon (i.e. the 5-8-5 configurations) (see Fig. 4.2). The distance between dangling bonds in DV_{CC} is found to be about 1.404 Å and the bond lengths of C and N atoms around the vacancies become 2.041 and 1.404 Å. The bond lengths of DV_{NC} are 1.404 and 1.404 Å (see Fig. 3). The DV_{NN} shows a non-reconstructed structure and the bond lengths of C and N atoms around the vacancies become 1.44 and 1.43 Å. For AS_{NC} we see a negligible bond length elongation in the modified structure. The C-C bond length undergoes a small modification from 1.404 to 1.406 Å, and the N-C bond length is calculated to be 1.400 Å. As can be seen from Fig. 4.2, after the formation of SW defect, four neighboring hexagons of C_3N are transformed into one pentagon and two heptagons (the 55-77 configurations), and C_3N maintains its planer 2D structure. Through 90° rotation of a dimer, the C-C bond becomes stronger than the

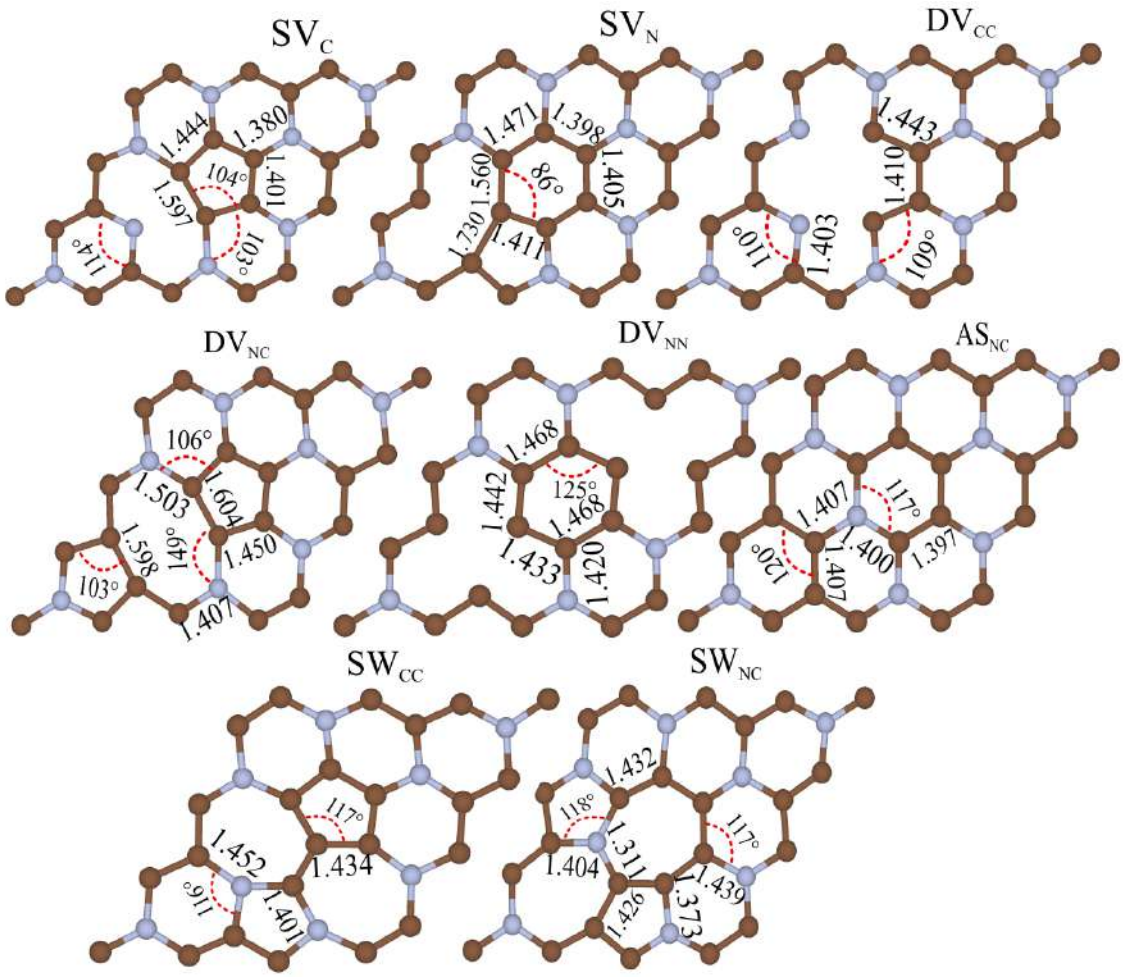

Figure 4.2: Optimized structures with corresponding bond lengths and angles of (a) SV_C, (b) SV_N, (c) C+C (DV_{CC}), (d) N+C (DV_{NC}), (e) N+N (DV_{NN}), (f) anti-site (AS_{NC}), (g) C-C (SW_{CC}) and (h) N-C (SW_{NC}) defects on C_3N.

one in pristine C_3N, and its length decreases from 2.281 to 2.191 Å. Due to the shortening of bond lengths along the direction parallel to the pentagons, the lattice constant decreases from 23.212 to 23.041 Å.

4.1.2 Electronic and magnetic properties

The effect of SV defects on the electronic and magnetic properties of C_3N, are shown in Fig. 4.3. It is noticeable that the band structure of pristine C_3N is strongly disturbed by

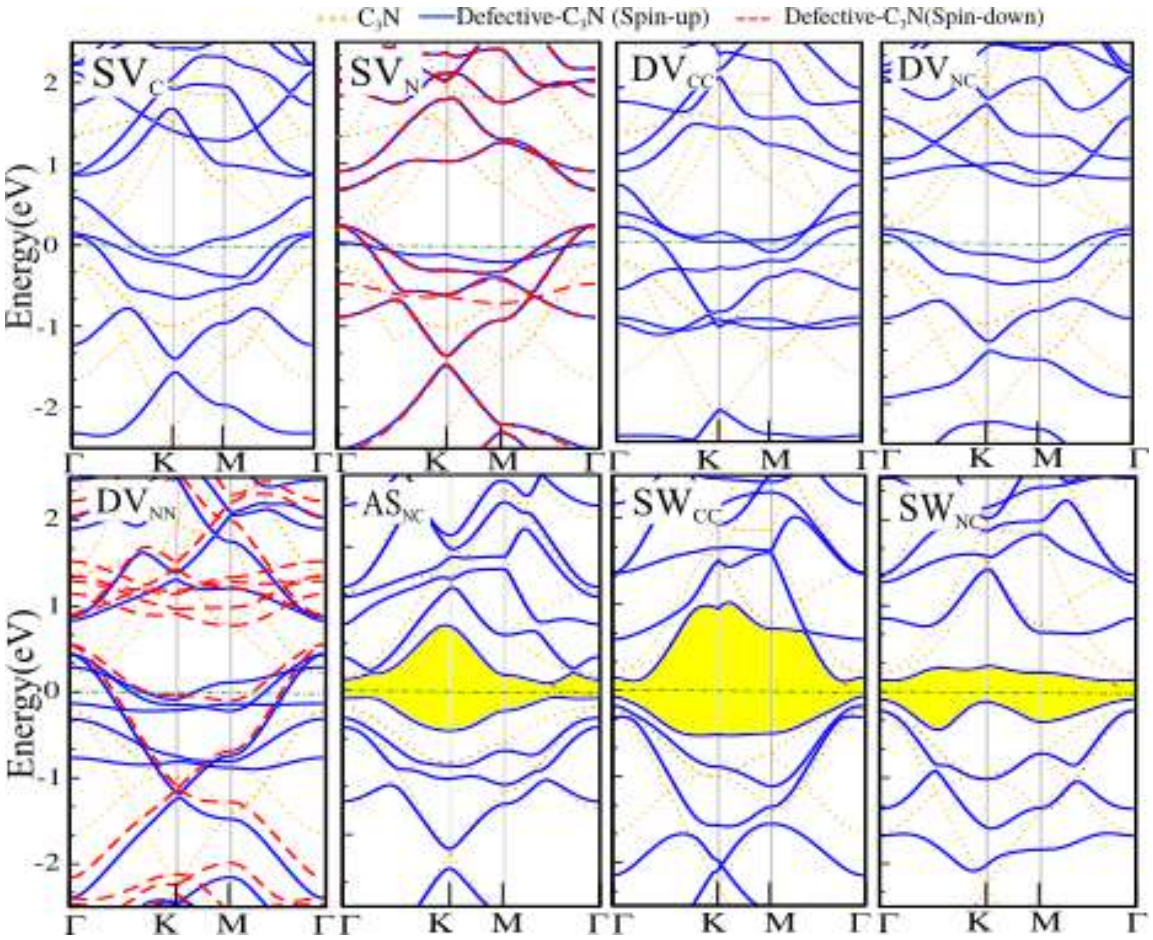

Figure 4.3: Electronic structure of C_3N with different defects including SV_C, SV_N, C+C (DV_{CC}), N+C (DV_{NC}), N+N (DV_{NN}), anti-site (AS_{NC}), C-C (SW_{CC}) and N-C (SW_{NC}). Dotted curves represent the electronic structure of pristine C_3N. The zero of energy is set to E_F, shown by the green dash-point line.

the vacancy defects. The SV_C and SV_N turns pristine C_3N into a metal and ferromagnetic-metal, respectively. In addition, SV_N has 0.3 μ_B magnetic moment due to the dangling bond around the defect sites with an unpaired electron. For DV_{CC} and DV_{NC}, similar to what we have for the SV-defect, states appear near E_F, resulting in metallic characteristics in the electronic structure. Our results show that DV_{NN}, becomes a ferromagnetic-metal and induces 3.5 μ_B magnetic moment to C_3N. We see that AS_{NC}, is a semiconductor with 0.2 eV indirect band gap. After introducing the SW defects, the electronic states experience a shift due to the breaking of the hexagonal lattice symmetry by the SW defect.

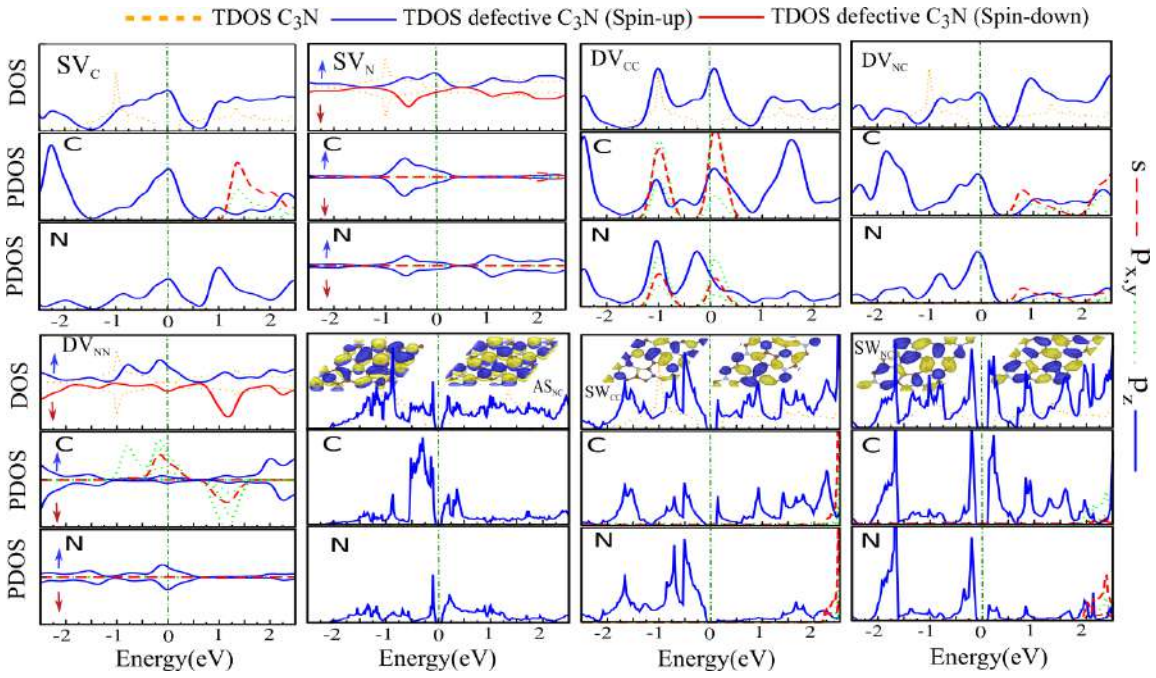

Figure 4.4: DOS and PDOS SV_C, SV_N, C+C (DV_{CC}), N+C (DV_{NC}), N+N (DV_{NN}), anti-site (AS_{NC}), C-C (SW_{CC}) and N-C (SW_{NC}) defects on C_3N. The charge distributions for the VBM and CBM are shown in the insets. Blue and yellow regions represent charge accumulation and depletion, respectively.

The SW-C_3N, is an indirect semiconductor with 0.2 eV band gap due to the introduction of an energy level near the CB, which is related to some bonds of both C and N atoms around the defect. The VBM (CBM) is located at Γ (between M and Γ points). Moreover, the band becomes flatter which indicates a strongly localized charge around these defects.

The DOS and PDOS SV_C, SV_N, C+C (DV_{CC}), N+C (DV_{NC}), N+N (DV_{NN}), anti-site (AS_{NC}), C-C (SW_{CC}) and N-C (SW_{NC}) defects on C_3N is shown in Fig. 4.4. It is also evident from the DOS and PDOS, that the state at E_F of SV-C_3N belongs to the C/N-p_z orbital around the missing atom which confirms the metallic behavior of SV-C_3N. By analyzing of PDOS it is clear that the magnetism in SV_N are derived from the C-p orbitals of the C atoms in SV_N. For the case of DV_{CC}, we found that the state at E_F belongs to the s and p-orbitals of C and N atoms locating around the missing atom which confirms the metallic behavior, whereas, for DV_{NC}, the state around E_F originates from C/N-p_z orbitals. While the VB and CB of DV_{NN} belongs to the C/N-s,$p_{x,y}$ orbital, the VB and CB of AS_{NC} belongs to the C/N-p_z orbitals. The VB of SW_{CC} and SW_{NC} has N-p_z orbital and the CB is build up of the C-p_z orbital around the defect, which results in

semiconducting behavior.

4.2 Substitution of atom

With fully structural optimization, where all atoms are relaxed in all directions and calculations are performed using $2 \times 2 \times 1$ supercell of C_3N which contains 32 atoms (24 C and 8 N atoms). We consider two substitution sites: (1) the C host atom site (Sb_C) and (2) the N host atom site (Sb_N). The change of lattice constant is shown in Fig. 4.5(a) and a schematic view of two substitution sites are shown in the inset. The substitution of foreign atoms with C (N) host atom of C_3N, is labeled as Sb_C-C_3N (Sb_N-C_3N). For instance, substitution of H atom for C (N), is labeled as H_C-C_3N (H_N-C_3N). The induced strain to the lattice structure of the C_3N can be estimated by calculating (a-a_0)/a_0, where a_0 is the lattice constant of pristine C_3N and a is the lattice constant of Sb-C_3N. The induced strain is plotted in Figs. 4.5(b,c). Lattice deformation of the substituted-C_3N structure exhibit an increase of induced distortion to the C_3N lattice constant. From Figs. 4.5(b,c), we find that the strain for H, O, S, F, Cl, B, Si and P substitution for C and N sites varies between 0.5 to 5 $\%$. For the Li, Na, K, Be, Mg, Ca and Al atoms the strain varies between 2.5 to 9 $\%$ which is significantly larger. Notice the increase in lattice constant with the atomic number which is present in both cases (see Fig. 4.5(a)). The interaction between the substituted atoms and the C_3N lattice can induce a charge redistribution. The Mulliken population analysis was performed to quantitatively analyze this effect. Positive (negative) charge transfer indicates a loss (gain) of electrons for each substituted atom to (from) C_3N. In pristine C_3N there is a charge transfer from C to N atoms. However, those C and N atoms in the substituted C_3N, have different Mulliken charges because of the different arrangement of atoms. The redistribution of charge for substituted C_3N depends mainly on the incorporation of substituted atom into the C and N lattice. For example, substitution of C host atom with Li and P atoms, induce Mulliken charges of -0.48 e and +0.53 e, respectively, while substitution with Na and Al yield +0.14 e and +0.23 e, respectively. The C and N atoms bonded to the substitutional atoms have much larger Mulliken charges than those in pristine C_3N. This difference can be attributed to the different atomic radius, electro-negativities, and their bond length of C and N atom with the foreign atoms.

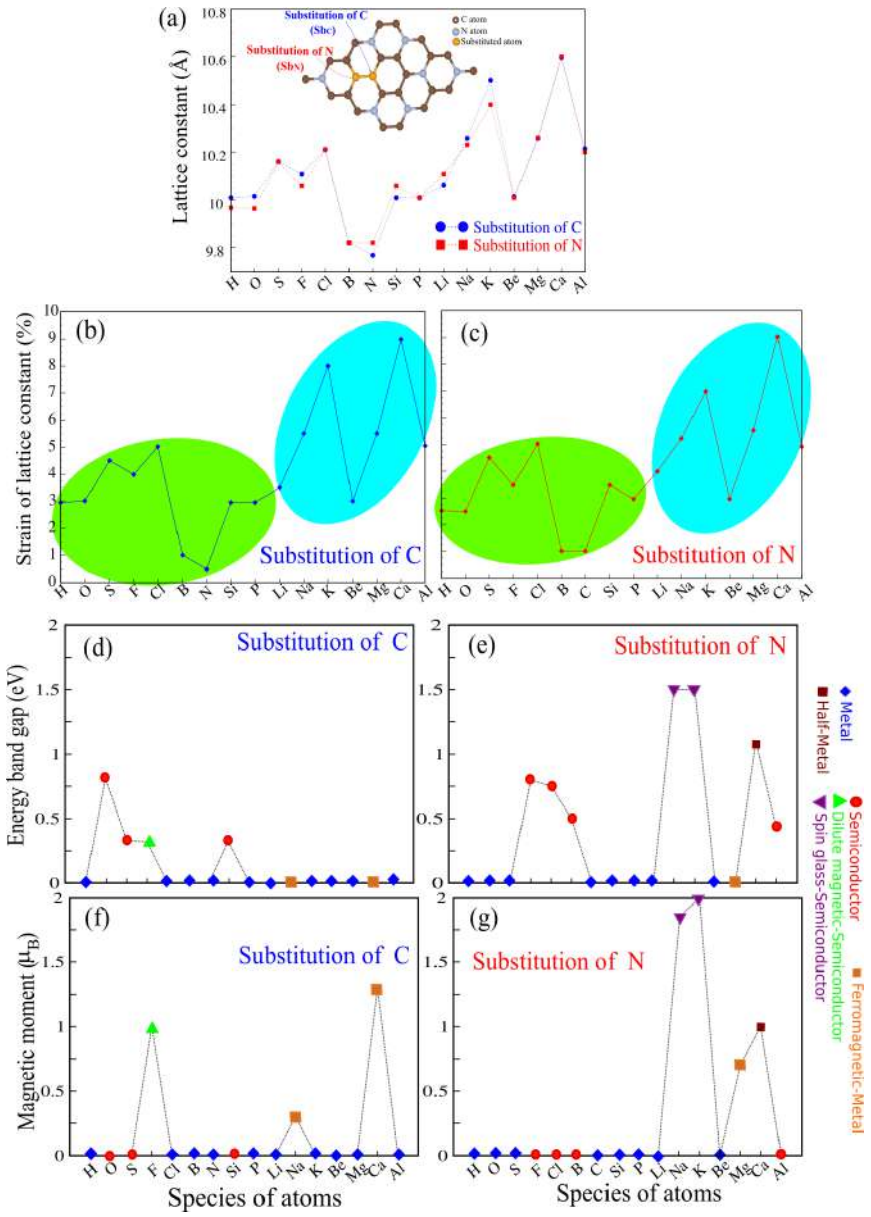

Figure 4.5: (a) Lattice constant of C_3N substituted with different atoms. Schematic model of two substitution sites is shown in the inset. (b,c) Effect of strain in lattice constant of C_3N substituted with different atoms. (d,e) Energy band gap and (f,g) magnetic moment due to substitution by difference species of atoms at respectively the, C and N host atom sites.

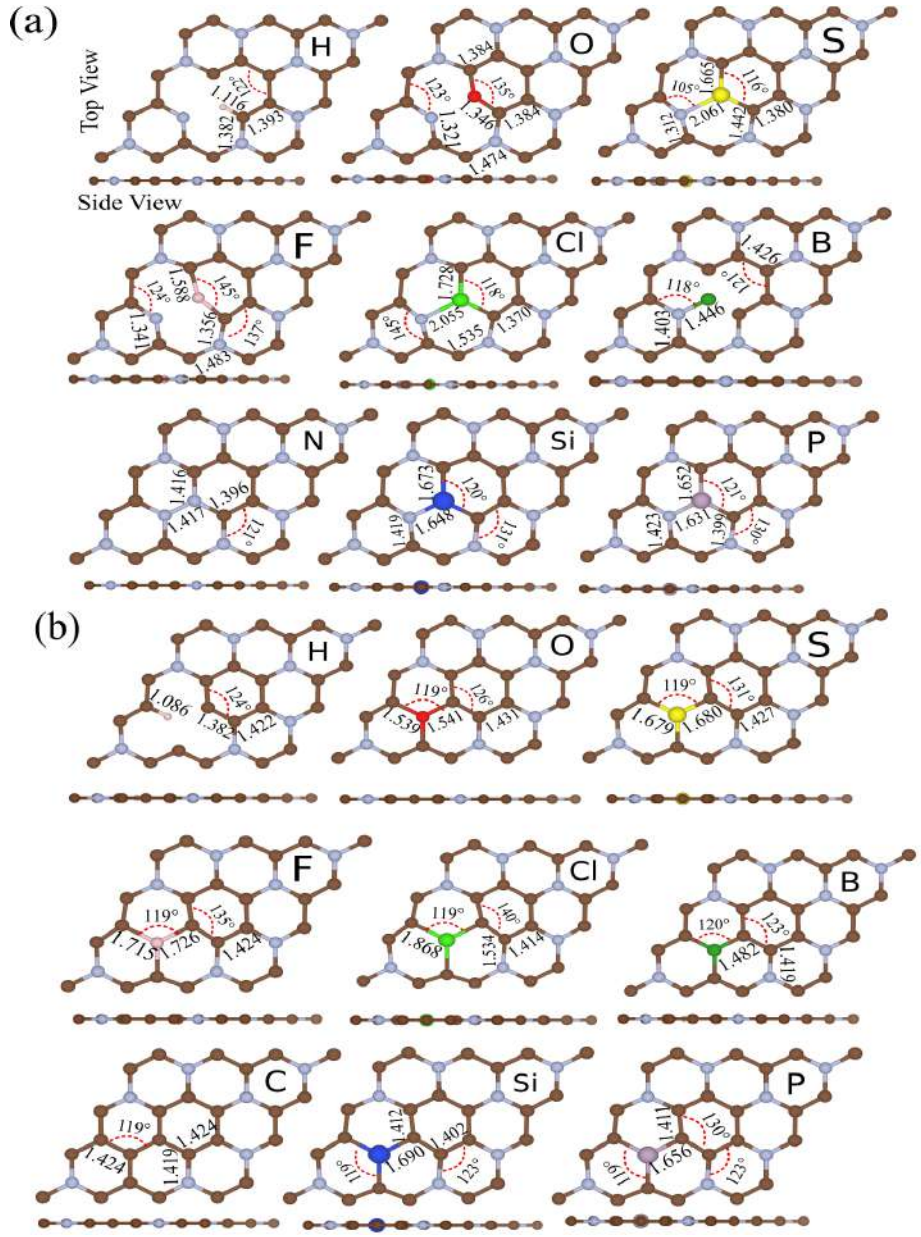

Figure 4.6: Optimized structures for substitution of (a) C or (b) N in the C_3N lattice with H, O, S, F, Cl, B, C, Si, N and P. Structural parameters including atomic bond length and angles are indicated. C, N and foreign atoms are shown by brown, blue and different colored balls, respectively.

4.3 Substitution of simple atoms

4.3.1 Structure properties

The optimized structures of H, O, S, F, Cl, B, C, Si, N and P substituted C_3N on C or N sites with their corresponding structural parameters including atomic bond length and angles are shown in Figs. 4.6(a,b). In the case of reconstruction, the honeycomb structure is deformed locally and the host atoms are pushed away from its lattice position. It can be seen that for H_C and H_N, the H atom becomes bonded to the neighboring C atom and the resulting length of the H-C bond is 1.116 and 1.086 Å, respectively. The O and F atoms interact through sp^2-hybridization, resulting in the formation of two and three σ bonds with the neighboring C atoms of C_3N, respectively. The bond length of O_C, O_N are 1.341 and 1.541 Å, and the C-O-C bond angles are 135° and 119°, respectively. For F_C and F_N, the F-C bond length is 1.582 and 1.712 Å, and the C-F-C bond angle is 145° and 119°, respectively. We can see a strong effect on the planar structure of C_3N for F_C. For B_C and B_N, the B atoms form one and three σ bonds with the neighboring N and C atoms, respectively. and the bond length with the nearest N atom is 1.441 Å, while for B_N the bond length with the nearest C atoms is 1.482 Å and the C-B-C bond angle is 120°, with a small in plane distortion of the C_3N lattice. The Si and P atomic radius is larger than that of C or N atom and as a consequence the Si and P atoms induce a structural deformation along the direction of the C_3N plane, leading to an expansion of the lattice parameter with $\sim 3.0\%$. The change in bond lengths and angles reflect the size of substituted atoms, and due to changes in the optimized structure the charge transfer between the substituted atoms and the substrate are modified.

4.3.2 Electronic and magnetic properties

The electronic structure of H, O, S, F, Cl, B, C, Si, N and P atoms substituted C_3N, are shown in Figs. 4.7(a,b). The blue-lines and red-dash lines represent up and down spin states, respectively. The electronic states of C_3N after substitution of different atoms are listed in Table1. The corresponding electronic states are specified as metal (M), half-metal (HM), ferromagnetic-metal (FM), spin-glass semiconductor (SG-SC), dilute-magnetic semiconductor (DM-SC) and semiconductor (SC) and are indicated in Fig. 4.5. The band gap and magnetic moment are indicated inside parentheses. In comparison with pristine C_3N, the shape of the electronic structure of Sb-C_3N is significantly modified. The H_C, Cl_C, H_N, O_N and S_N are metal, while O_C is a semiconductor with 0.6 eV direct band gap, where the VBM and CBM are located at the Γ point. We can see that S_C and Cl_N are indirect semiconductors with band gap of 0.33 eV and the VBM and CBM are

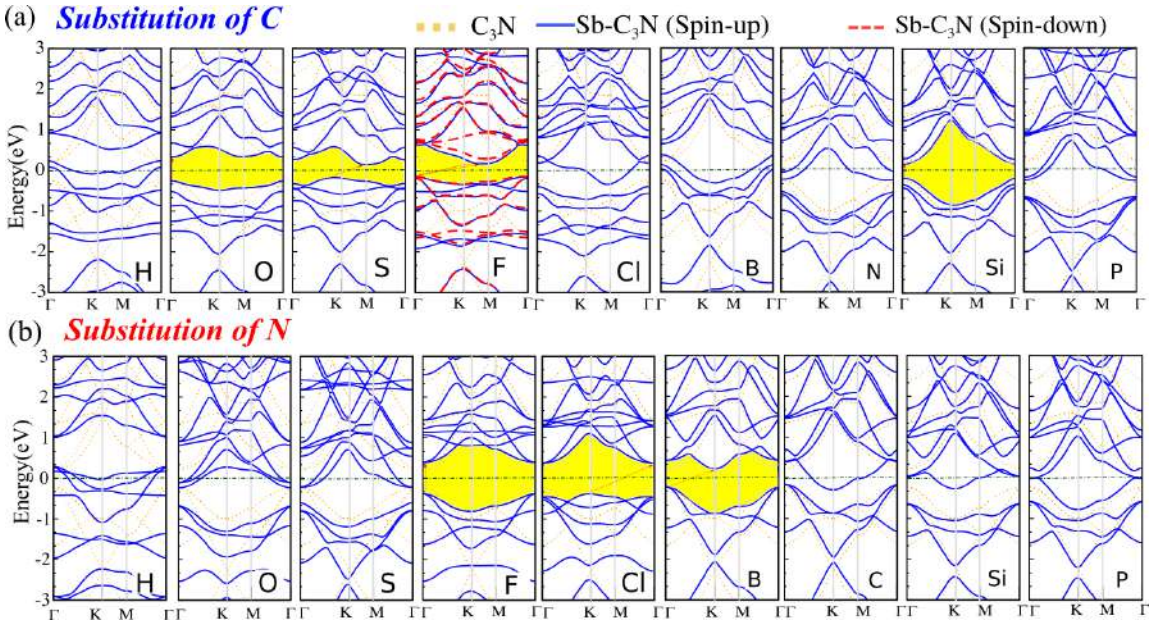

Figure 4.7: Electronic structure for substitution of (a) C or (b) N in the C_3N lattice with H, O, S, F, Cl, B, C, Si, N and P. The dotted curves represent the electronic structure of pristine C_3N. The zero of energy is set to E_F, shown by the green dash-point line.

located at the K point and between the M and Γ point, respectively. Moreover, S_C exhibit a p-type semiconductor, because these atoms gain electrons, resulting in a down shift of the E_F inside the VB edge. F_C is a dilute-magnetic semiconductor and the excess electron of the substituted F atom relative to C leads to spin-polarization and induces a magnetic moment of 1 μ_B in the ground state per F atom. B_C is a metal, while B_N is an indirect semiconductor with 0.5 eV band gap. Notice that the N atom has two extra electrons on the outer shell as compared to B which influences the VB and CB of C_3N. These excess electrons of the substituted N atom leads to a filling of the VB edge, similar to a p-type semiconductor and as a result B_N exhibit hole doping and thus causes a down shift of E_F. Also Si_C is a direct semiconductor with 0.34 eV band gap, while Si_N becomes a metal and the impurity states appear near the VBM and CBM edge.

The electronic structure of H, O, S, F, Cl, B, C, Si, N and P atoms substituted C_3N, are shown in Figs. 4.7(a,b). We found no spin polarized band structure for N_C, P_C, C_N, Si_N and P_N which exhibit metallic characteristics with their E_F crossing the electronic states. For Cl_C the electron states near E_F are mainly governed by the C/N-p_z orbitals and for Cl_N are governed by the C-$p_{x,y}$, N-p_z and Cl-s orbitals. We found that the VBM of Cl_C is due to the hybridization of Cl-s with C-$p_{x,y}$ and N-p_z orbitals of the nearest atoms and

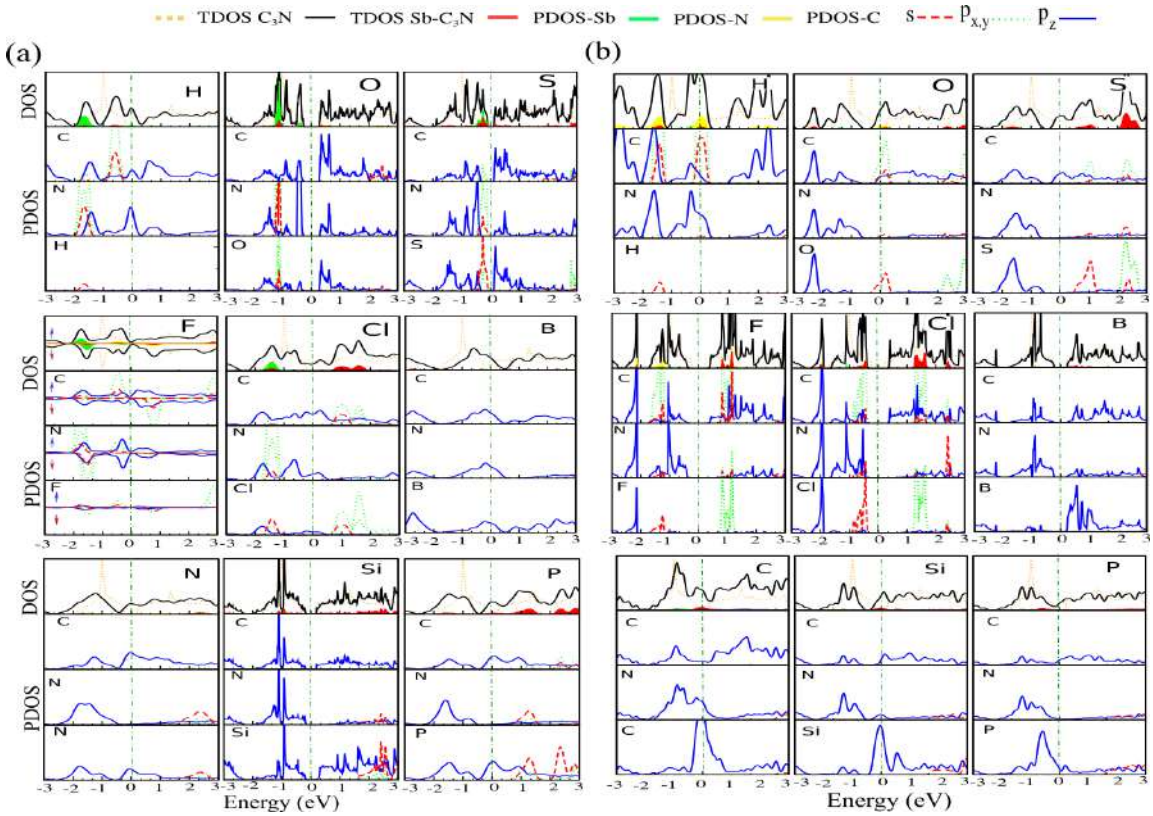

Figure 4.8: DOS and PDOS for substitution of (a) C or (b) N in the C_3N lattice with H, O, S, F, Cl, B, C, Si, N and P.

CBM of Cl_C originates from Cl-$p_{x,y}$ with $p_{x,y}$ orbitals of the nearest C atoms. The VBM of S_C is due to the hybridization of S-$s, p_{x,y}$ with $p_{x,y}$ orbitals of the nearest N atoms and the CBM of S_CN originates from S-p_z with p_z orbitals of the nearest C atoms. For F_C there is an asymmetric spin splitting around E_F and as a consequence the defected structure becomes a dilute-magnetic semiconductor with an induced magnetic moment.

The DOS and PDOS for substitution of (a) C or (b) N in the C_3N lattice with H, O, S, F, Cl, B, C, Si, N and P is shown in Fig. 4.7. The discussion of corresponding PDOS further reveals that these asymmetric impurity states in the band gap mainly originates from the hybridization of N/F-2p and the C-2p orbitals leading to a magnetic moment of 1 μ_B. However for F_N, the hybridization is slightly different and the state near E_F mainly originates from the F-3s and C-p_z orbital states. PDOS of B_C shows that the CBM arises from the B-p_z and C/N-p_z orbitals. Also hybridization between the B-p_z and C/N-p_z orbitals mainly contributes to the VBM. For Si_C, Si being in the same group as C in the

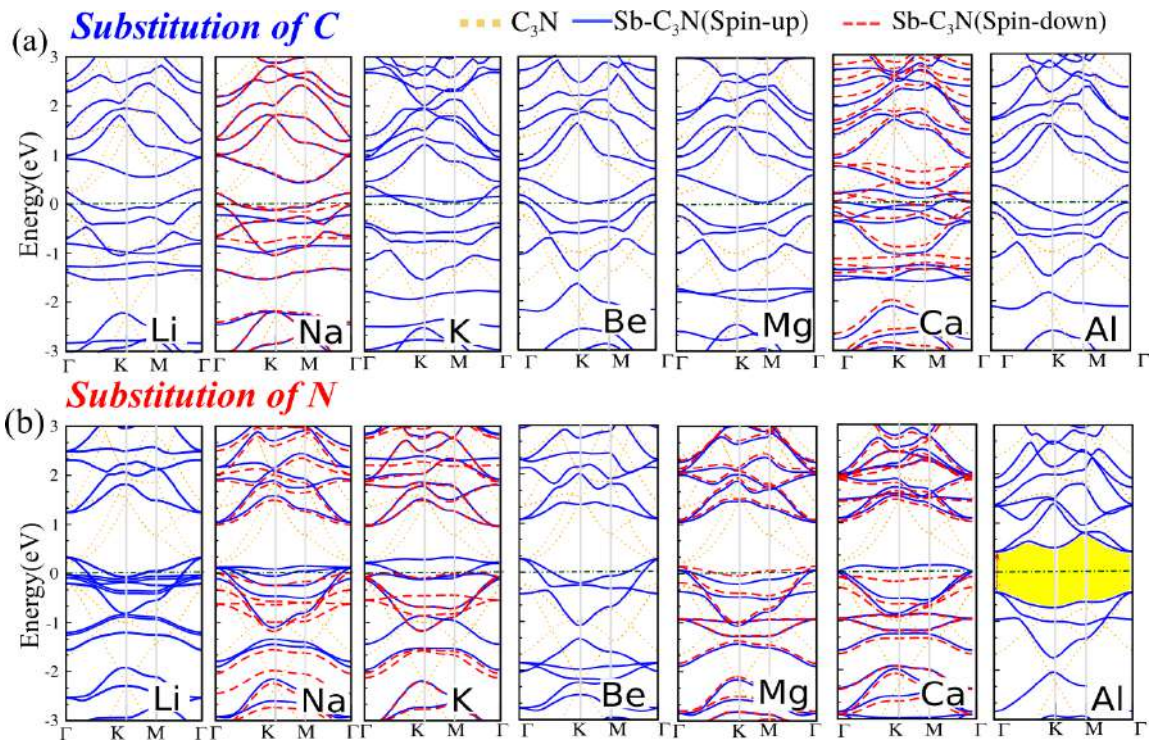

Figure 4.9: Electronic structure for substitution of (a) C or (b) N in the C_3N lattice with Li, Na, K, Be, Mg, Ca and Al. The zero of energy is set to E_F, shown by the green dash-point line.

periodic table with a larger atomic radius, distorts the planar structure of C_3N and causes an increase in the bond length. VBM of C_3N is not influenced much upon substitution, where the states originate from Si-p_z orbitals. DOS and PDOS of P_C and P_N, show that both the CBM and VBM are composed of P-p_z and C-p_z orbitals. As expected, DOS of the B_C, N_C, P_C, B_C, C_N and Si_N, shows that the interaction between these atoms and C or N host atoms is responsible for the semiconductor to metal transition. Based on the calculated PDOS, both the CBM and VBM receive mainly contributions from the hybridization of the p_z orbitals.

4.4 Substitution of alkaline metals and alkaline earth metals atoms

4.4.1 Electronic and magnetic properties

Figs. 4.9(a,b) show the electronic band structure of Li, Na, K, Be, Mg, Ca and Al substitution in C_3N, while Na_C is ferromagnetic-metal with 1.3 μ_B magnetic moment. Interestingly, Na_N and K_N, exhibit spin-glass semiconductor behavior with 1.9 and 2 μ_B magnetic moments, respectively. Namely, the $\uparrow$ spin channel is gapless, while the $\downarrow$ spin channel is a semiconductor and the VBM touches the Fermi level. Such spin-gapless semiconductors are of particular interest for e.g. spin photo-diodes, spin detectors and electromagnetic radiation generators for a wide range of wavelengths based on spin photo-conductivity. We found that Be_C, Mg_C, Li_N, Li_C, K_C and Be_N, are metallic, while Ca_C and Mg_N are ferromagnetic-metals with induced 1.3 and 0.7 μ_B magnetic moments, respectively. Al_N is a direct semiconductor with 0.43 eV band gap where the VBM and CBM are located at the Γ point. Unlike Ca_C, we see that Ca_N remains a direct semiconductor with a 1 eV band gap in the $\downarrow$ spin channel, whereas the $\uparrow$ spin channel is metallic, thus Ca_N is a half-metal with 1 μ_B magnetic moment. This suggests that the charge carriers within the energy bands in the vicinity of E_F are mobile, which is not only useful for electrical conduction but also for magnetic coupling. Notice that the half-metallic behavior of Ca_N can be useful in spintronics. Finally, Al_N is a direct semiconductor with band gap of 0.43 eV, while VBM and CBM are located at the Γ point.

4.5 Conclusion and Summary

In summary by using first-principle calculations within the framework of DFT, a systematic investigation of the effect of topological defects including single and double vacancies, Stone-Wales and anti-site, on the structure and electronic properties of C_3N was presented. Our results show that for both single and double vacancies C_3N becomes a metal, except in the case of a single vacancy of N and double vacancy of N+N. C_3N with anti-site defects when C_3N becomes a direct semiconductor with 0.2 eV band gap. With Stone-Wales defects, C_3N becomes an indirect semiconductor with the band gap of 0.2 eV. Furthermore, we studied the effects due to H, O, S, F, Cl, B, C, N, Si, P, Li, Na, K, Be, Mg, Ca and Al substitution on the electronic properties of C_3N. When the C site is substituted with O, S and Si atoms, the system remains a semiconductor with band gap in the range of 0.25-0.75 eV, while with H, Cl, B, P, Li, Na, K, Be and Mg atoms the system turns into a metal. Also, upon substitution of the native C with F atom, C_3N becomes

a dilute-magnetic semiconductor, while with Ca substitution it is a ferromagnetic-metal. Moreover, when N is replaced with H, O, S, C, Si, P, Li and Be atoms the system turns into a metal and with F, Cl, B and Al atoms becomes a semiconductor. With Mg and Ca atoms it becomes a ferromagnetic-metal and half-metal with induces magnetic moments of 0.3 and 2 μ_B, respectively. In addition, with Na and K shows spin-glass semiconductor. Moreover, we investigated the effect of charging and strain on the electronic structure of C_3N, in which native C and N atoms are substituted with Na atom. Our result shows that the magnetic moment with applied charging and strain can be tuned. It is possible to tune the magnetism by controlling the Fermi level via external fields such as by charging and strain. Our calculations predict that the introduction of typical topological defects or by substitution of atoms in C_3N, provides an interesting way to tune the electronic and magnetic properties which can be useful in a diversity of applications including solar cells, sensors, nanoelectronics, optoelectronics and spintronic devices.

CHAPTER 5

Electric filed and mechanical strain

In this chapetr, by using of first-principles calculations, we as systematically investigate the structural, electronic and magnetic properties of a novel two-dimensional materials (2DM), with a stoichiometry of C_3N is recently synthesized. Control of layer thickness, is an effective method to tune the electronic properties of 2DM. We found that single layers of C_3N are stacked together to form a bilayer and trilayer with multiple type stacking of layers. In result shows metallic and semiconducting character. Transition of semiconductor to metal in C_3N nanosheet through thickness control could potential application in future nanoelectronic devices. In addition, we study the effects of width and length of C_3N nanoribbon as well as radius and length of C_3N nanotube, on structure and electronic properties. In result, we found how the electronic and magnetic properties C_3N nanoribbon and nanotube, depending on the width, length and radios of C_3N nanoribbon and nanotube are modified. It would be noted that the properties of nanoribbon and nanotube are significantly dependent on the edge states. Adsorption of adatom is an robust approach to improve and modulate the properties of 2DM. We investigated the adsorption of H adatom on C_3N nanostuctures, and our calculation shows that they may induce metallic, half-metalic, semiconducting and ferromagnetic behaviors. We also, investigate effect of an external field strain on C_3N nanostuctures and found that the electronic and magnetic properties C_3N are modified. Our calculation insight into C_3N showing an unusual electronic and magnetic properties. Therefore, the C_3N nanosheet, nanoribbons, nanotubes are predicted to have great potential applications in sensor, electronics and optoelectronic at the nanoscale. We investigate effects of an electrical field, charging and strain on C_3N

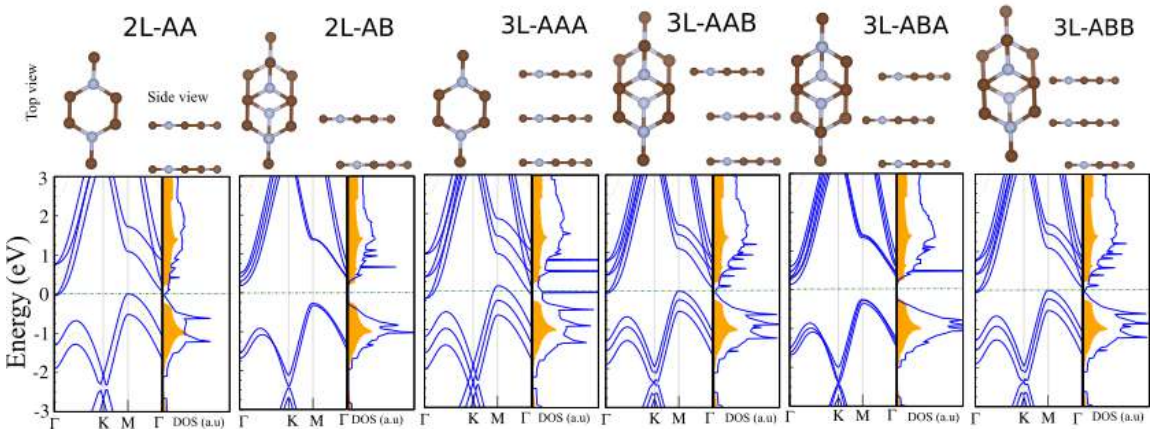

Figure 5.1: Optimized structures, band structure, DOS and PDOS of a few layer C_3N nanosheet with different stackings. The zero of energy is set to the Fermi level energy.

and found how the electronic and magnetic properties are modified. Semi and fully hydrogenation, are studied. From our calculations we gained novel insights into the properties of C_3N demonstrating its unique electronic and magnetic properties that can be useful for semiconducting, nanosensor and catalytic applications.

In this paper, firstly we investigate the layer thickness-dependent on the electronic property of C_3N nanosheet. Single layers of C_3N can be stacked together and form a few layer of C_3N with multiple type stacking configuration. In result, depending to layer thickness and type of stacking, we can see that the band structure, exhibits a metallic or semiconducting behaviors. The main point is that the C_3N nanoribbon (C_3NNR) and nanotube (C_3NNT) are characterized through the change electronic character by width, length and radius respect to the zigzag and armchair edgs states. The character of these nanostructures in either shape can be tuned through changing length/width in the nanoribbon or length/radius of the nanotube. Moreover, we investigate an analysis from adsorption of H adatom on the C_3N nanaostructures. Our result show that the electronic and magnetic properties can be modified through adsorption of H adatom. In addition, the effects of charging and strain on the electronic structure of C_3N nanostructures, are studied. Our result showed that the band gap and magnetism can be modulated by these ways. Some of these properties can be useful and very promising for future applications.

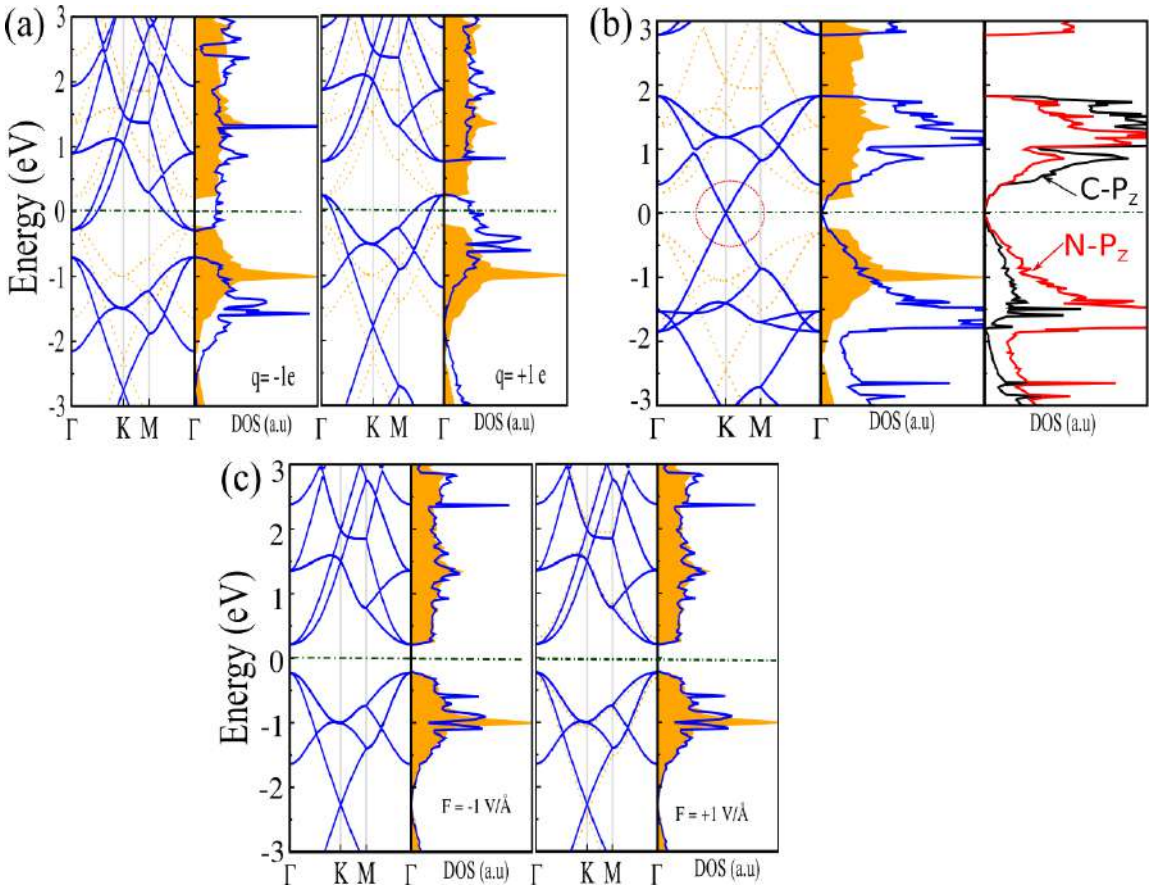

Figure 5.2: Electronic band structures and DOS of C_3N as a function of (a,b) charging and (c) electric field. The **F**= +1 and -1 V/Å denotes parallel and antiparallel to the z-axis), respectively. The q= +1 e and q= -1 e, corresponds to the charging where one electron is removed from and added to the C_3N, respectively. Zero of energy is set at the E_F indicated by dash-dotted lines.

5.1 Layer thickness

We constructed bilayer C_3N (2L-C_3N) with two different stacking sequences of AA and AB. In the AA stacking, the in-plane position of atoms on the two layers are exactly the same, while in the AB stacking, the in-plane atomic positions of the top layer are shifted such that some of the atoms are placed on the hollow center of the hexagonal lattices of the atoms on the bottom layer. In the trilayer C_3N (3L-C_3N), sandwich structure, we consider four stacking configurations: AAA, ABA, ABB and AAB. In the ABA stacking configuration, a hexagonal ring center (labeled by) and a C atom are located directly below and above the C atom of the a C_3N lattice, respectively; and a N atom and a hexagonal ring

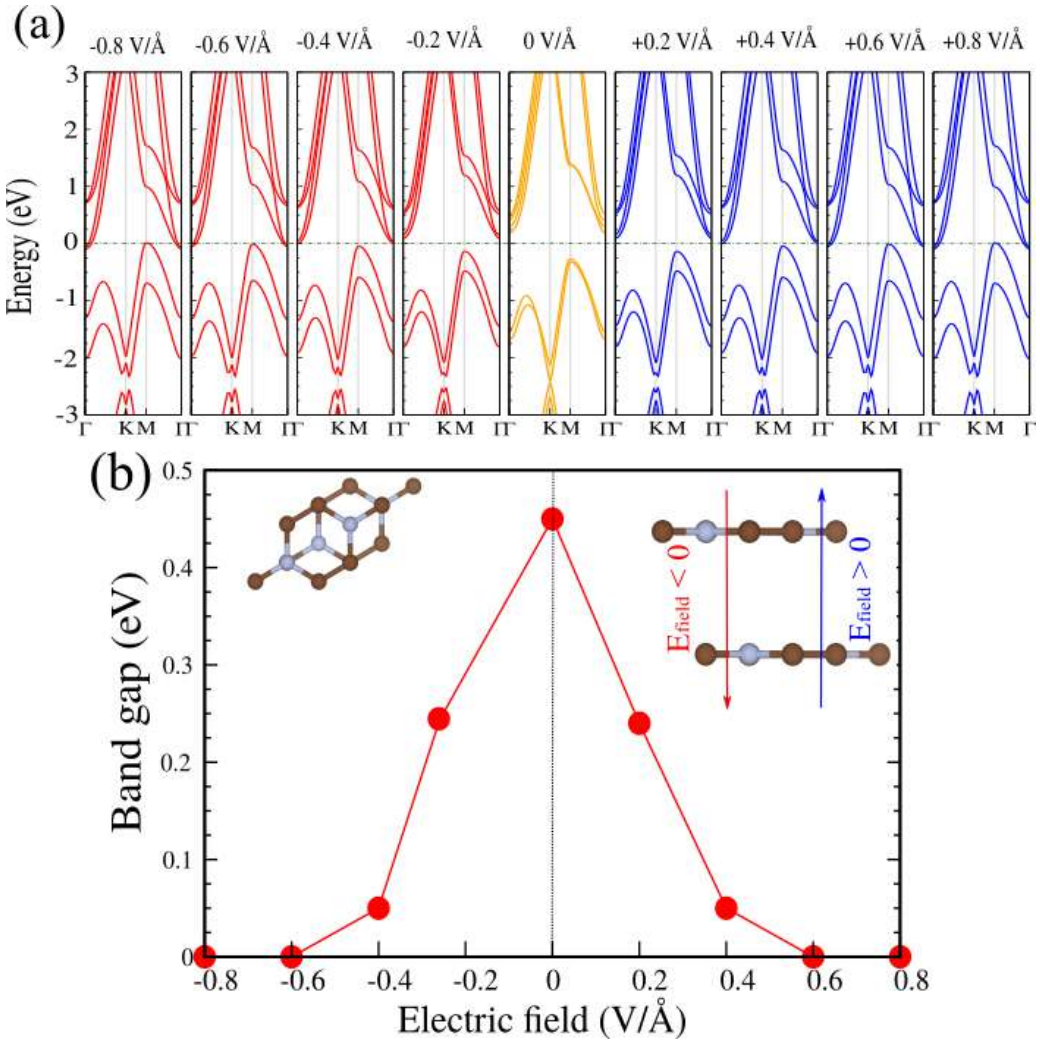

Figure 5.3: (a) Electronic structure of bilayer C_3N as a function of the an electric field, whose strength varies from -0.8 to +0.8 V/Å. The perpendicular electric field **F**> 0 and < 0 that denotes parallel and antiparallel to the z-axis, respectively. The zero of energy is set at the E_F. (d) Band gap of bilayer C_3N with respect to the electric field.

center are located directly below and above the C atom of C_3N lattice, respectively. The optimized atomic structure of 2L- and 3L-C_3N, are shown in Fig. 5.1. After the geometry optimization, the interlayer distances between the layers of 2L-C_3N, were obtained 3.309 (AA) and 3.298 Å (AB), While for the 3L-C_3N were obtained 3.301 (AAA), 3.305 (ABA), 3.587 (ABB) and 3.316 (AAB) Å, stackings. For the 2LAA- and 2LAB-C_3N, the in-plane

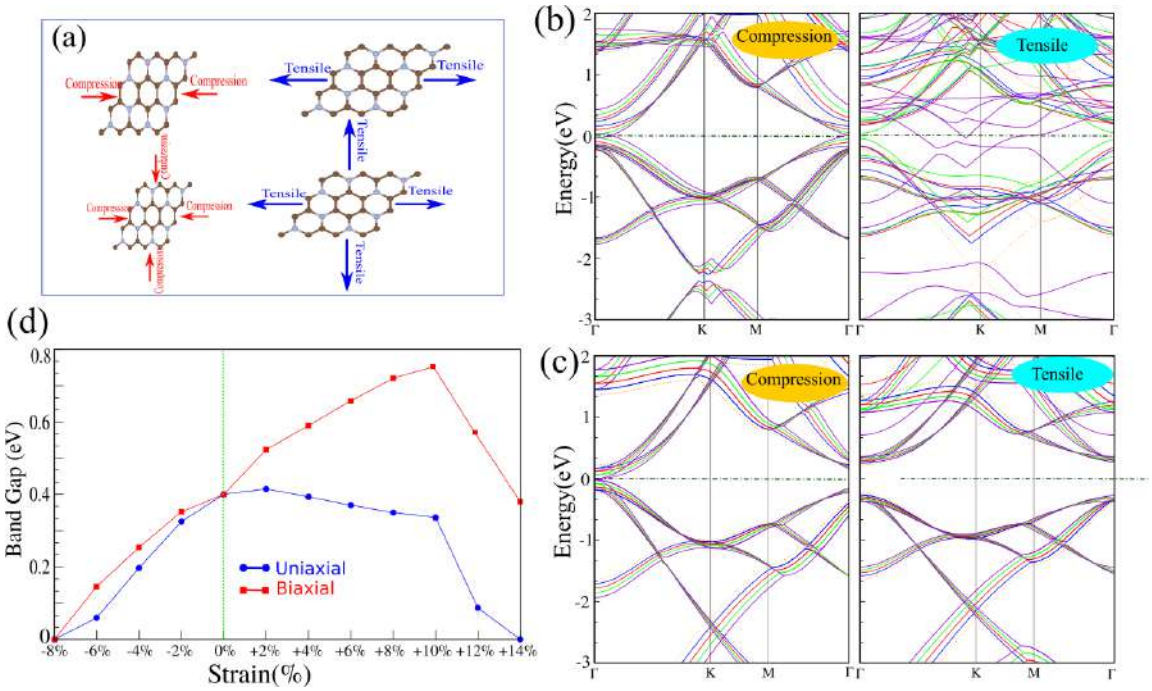

Figure 5.4: (a) Schematically view of the uniaxial and biaxial strain applied on C_3N along ab-axis. Electronic band structures of C_3N as a function of (b) uniaxial strains along zigzag directions and (c) biaxial strains. The E_F is set to zero. (d) The band gap a function of uniaxial and biaxial strains.

covalent bond lengths of the C-C and C-N atoms were 1.398 and 1.408 Å, respectively that compared to C_3N the bond lengths changed (C-C and C-N bond lengths are 1.403 and 1.404 Å). For 3L-C_3N, the in-plane covalent bond length of the C-C and C-N atoms is $\sim$ 1.40 Å. The electronic structure of 2L- and 3L-C_3N, are shown in Fig. 5.1. We found that the energy band of C_3N is modified by number of layer and type of stacking configuration. Our result show that the 2LAA, eliminate the semiconducting band gap of C_3N and exhibit a metallic property, while the 2LAB, becomes a indirect semiconductor with 0.45 eV band gap, while the VBM and CBM are located at the Γ and **M** points, respectively. In the 3L-C_3N, exhibit a metallic characteristics with their Fermi levels crossing the electronic states for all stacking except the 3LABA, that becomes a indirect semiconductor with 0.5 eV band gap. Compared to the monolayer C_3N nanosheet band gap (0.4 eV), the band gaps of bilayer and trilayer in the 2LAB and 3LAB stackings ones are pronouncedly reduced because of the strong interlayer interaction and some bonds of both C and N atoms. [171, 188]

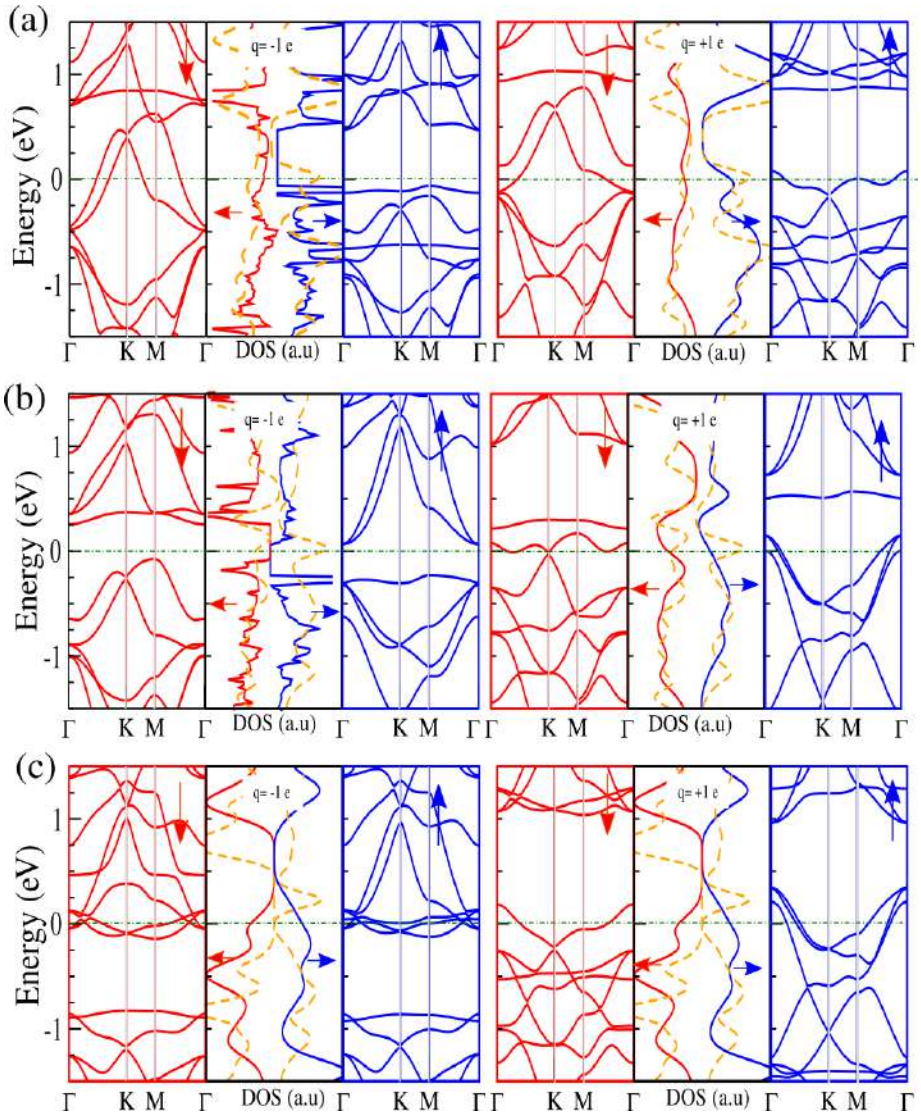

Figure 5.5: Electronic band structure of (a) Ti, (b) Mn and (c) Fe adsorbed C_3N as a function of charging. The q= +1 e and q= -1 e, corresponds to the charging where one electron is removed from and added to the C_3N, respectively.

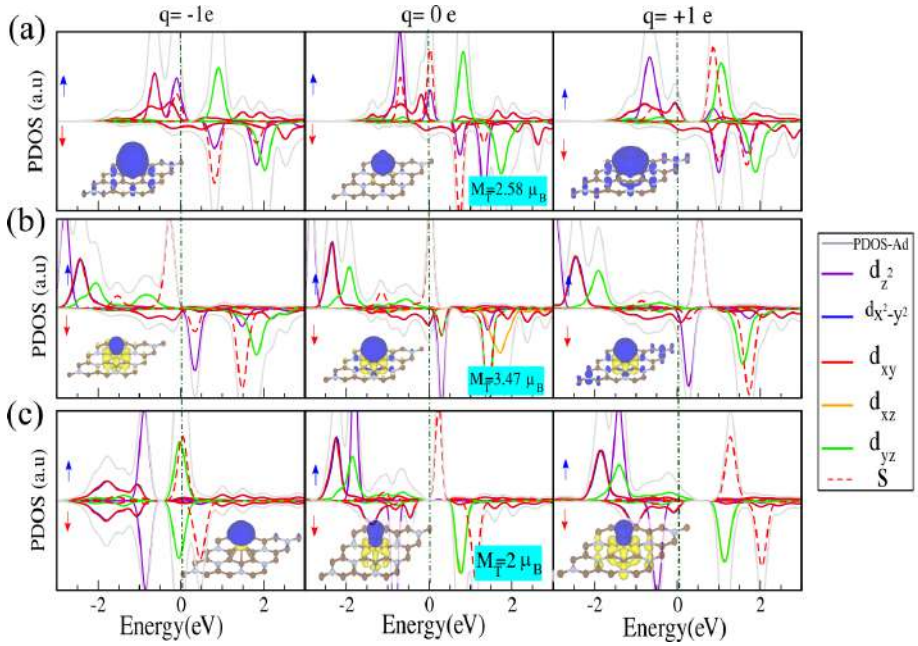

Figure 5.6: DOS and PDOS of (a) Ti, (b) Mn and (c) Fe adsorbed C_3N as a function of charging. The q= +1 e and q= -1 e, corresponds to the charging where one electron is removed from and added to the C_3N, respectively.

5.2 Applying an electric field and charging on the pristine C_3N

We present here the effect of charging, electric field and strain on the properties of C_3N. In Figs. 5.2(a-b), the changes in band structure and DOS with charging are shown. For q = +1 e, the Fermi level shift into the VB and creates holes, while for q = -1 e, the Fermi level shifts into the CB and creates electrons. Incidentally, as a result of negative charging (q = -8 e), Dirac-point moves to the Fermi level and the VBM and CBM touch each other at the Fermi level, similar to graphene. The electronic band structures and DOS of the C_3N as a function of electric field, is shown in Fig. 5.2(c). The **F**= +1 and -1 V/Å denotes electric field parallel and antiparallel to the z-axis, respectively. For both **F** = +1.0 and -1.0 V/Å, the C_3N did not yield any change in electronic state as a result of applied electrical field. We examined other values of **F** and found that the electronic structure of C_3N does not change.

Here we investigate the effect of an uniform electric field on the electronic property of bilayer C_3N under a perpendicular electric field $\mathbf{F} > 0$ and < 0 that denotes parallel

and antiparallel to the z-axis, respectively. The electronic structure, under an electric field of -0.8 to +0.8V/, is shown in Fig. 5.3(a). We found that, the electric field changes the electronic structure of bilayer C_3N and brings out a redistribution of molecular orbitals as well as a reduction in the gap between frontier molecular orbitals, result in the presence of a electric field lowers energy gap. My results show, when we apply an electric field the band gap will decrease and reach to zero gap as the electric field increases (parallel and antiparallel to the z-axis) and a semiconductor-to-metal transition occur.

Result in, it is possible to tune the electronic properties by controlling the Fermi-level. The energy band gap versus the applied electric field in the normal direction, whose strength varies from -0.8 to +0.8 V/, is shown in Fig. 5.3(b). The optimized atomic structure of bilayer C_3N indicated in the inset. Owing to their tunable band gaps in a wide range for the layered C_3N materials will have tremendous opportunities to be applied in nanoscale electronic and optoelectronic devices.

5.3 Mechanical strain

5.3.1 Strain on the pristine C_3N

2DM monolayers are often put or a substrate which may induce strain. Strain engineering is a important methods to change the properties of 2DM. We investigate the effects of uniaxial and biaxial strain (tensile and compression) on C_3N. The tensile and compression strain are defined as $\varepsilon = (a - a_0)/a_0 \times 100$, where a and a_0 are strained and non-strained lattice constants, respectively. Uniaxial strain is applied along zigzag direction, while biaxial strain is applied along ab-axis. The band structure under uniaxial (tensile and compression) strains, are shown in Fig. 5.4. Under uniaxial tensile strain along zigzag direction C_3N becomes metallic when it is larger than +14$\%$. The reason is that the CB at the C point shifts down to the E_F and in the VB vicinity the Γ point rises up to E_F. Interestingly, the Dirac-point (located at about -2.25 eV) will move away from the K point to the M point in the Brillouin zone. Under uniaxial compression strain along zigzag direction the structure becomes metallic when larger than -8$\%$ and the Dirac-point will move away from the K point to the M point in the Brillouin zone. The electronic band structure under biaxial strain (tensile and compression), are shown in Figs. 5.4(b,c). For biaxial compression strain, we see that C_3N transforms into a metallic state if the amount of compression strain is larger than -8$\%$. This differs from the case of biaxial tensile strain where semiconducting behavior is found up to +14$\%$. Fig. 5.4(d), shows the variation of energy band gap with strain. The energy band with increase of uniaxial strain, decreases to zero gap for compression strain of -8$\%$, and becomes metallic for tensile strain of +14$\%$. Also the band gap increases from 0.4 eV as biaxial tensile strain is applied to C_3N and the

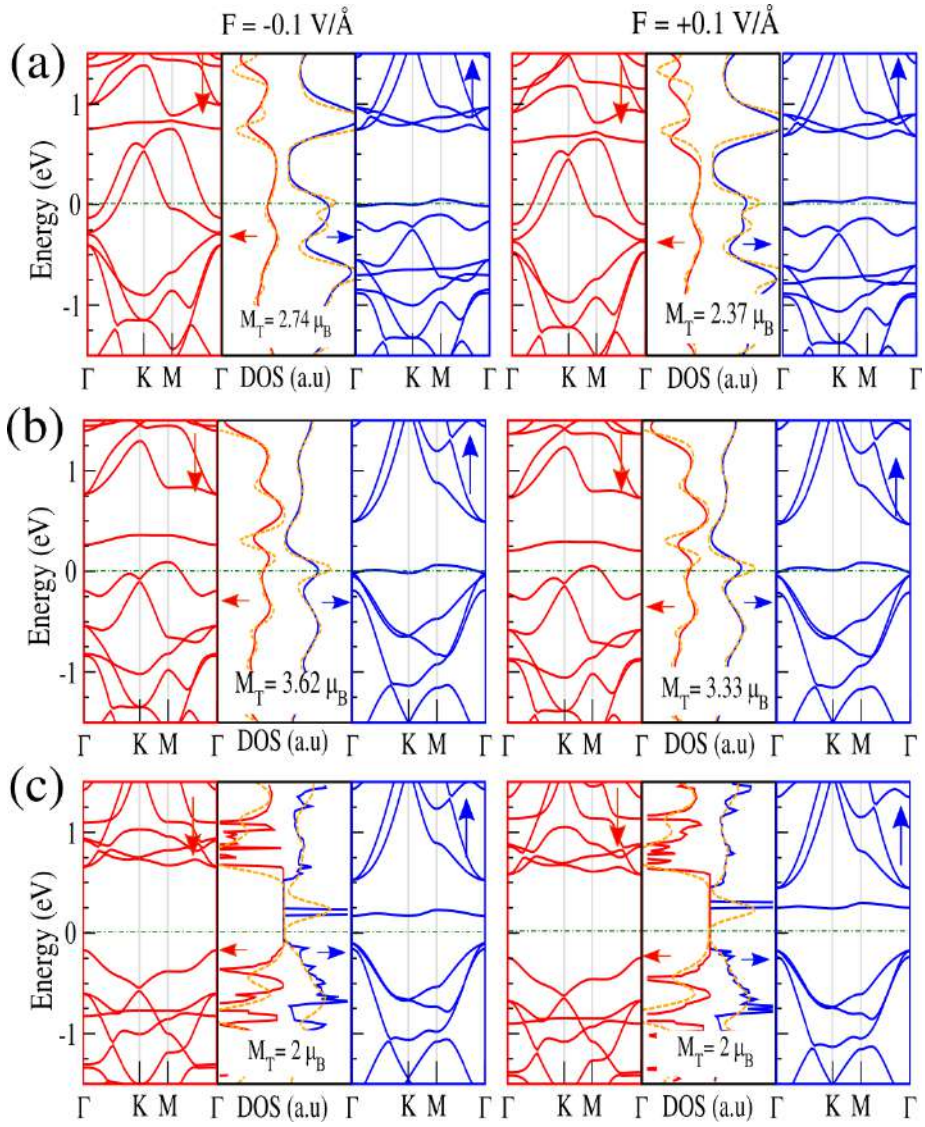

Figure 5.7: Electronic band structure of (a) Ti, (b) Mn and (c) Fe adsorbed C_3N as a function of electric field (**F**). **F**= +1 and -1 V/Å denotes parallel and antiparallel to the z-axis, respectively.

energy band gap increases with biaxial compression and becomes metal at -8%.

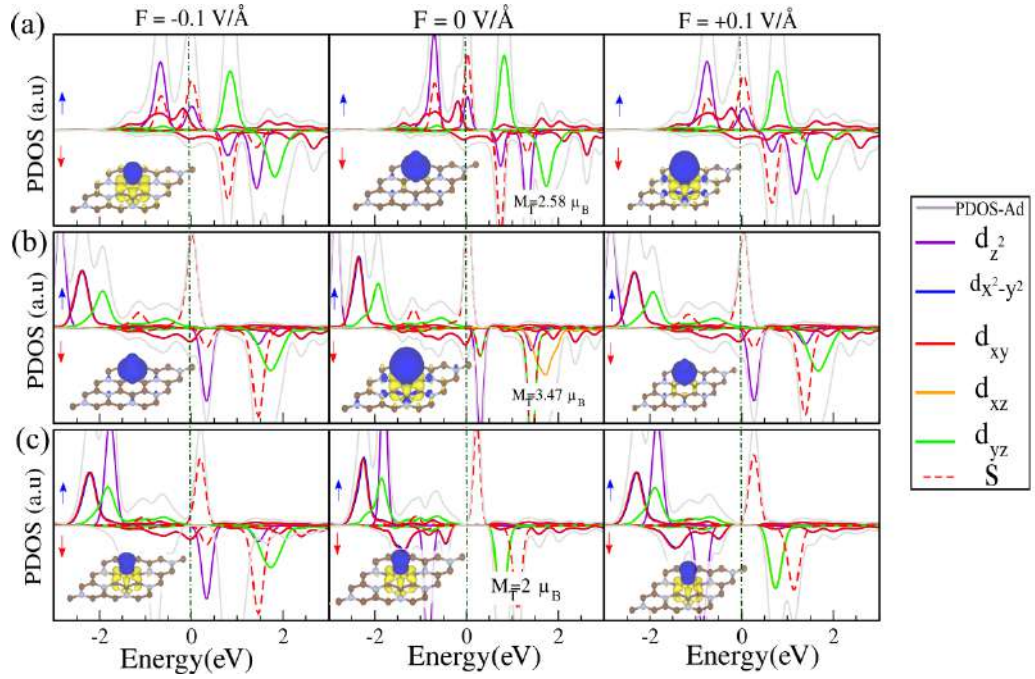

Figure 5.8: DOS and PDOS of (a) Ti, (b) Mn and (c) Fe adsorbed C_3N as a function of electric field (**F**). **F**= +1 and -1 V/Å denotes parallel and antiparallel to the z-axis, respectively.

5.4 Effect of charging on the adsorbed-TM atoms C_3N

The effect of charging, electric field and strain on the properties of TMs/C_3N (TMs= Ti, Mn and Fe) are here discussed. We show the calculated variation of the magnetic moment with charging in the case of q = +1 e (when one electron is removed) and q = -1 e (when one electron is added). The electronic band structure and DOS of the TMs/C_3N (TM= Ti, Mn and Fe) as a function of charging, are shown in Fig. 5.5. and 5.6, respectively. Our results show that Ti/C_3N is spin-polarized with 2.58 μ_B and the magnetic moment of the Ti/C_3N increases to 2.6 μ_B with q = +1 e and remains a ferromagnetic-metal, whereas for excess electronic charge of q = -1 e, the magnetic moment increases to 2.95 μ_B and it become a ferromagnetic-half metal. Namely it is metal for one spin channel, but a semiconductor for the opposite spin channel. This material transports electrons only in one spin channel and can function as a spin valve. The Mn/C_3N is a ferromagnetic-metal with 3.47 μ_B and reach 2.62 μ_B, when 1 electron is removed (q = +1 e) from the Mn/C_3N and it remains metal. Under excess electronic charge a reverse situation is observed, where the magnetic moment decreases to 4 μ_B for q = -1 e and C_3N becomes a semiconductor. For Fe/C_3N, which is a semiconductor with 2 μ_B in neutral state, magnetic moment decreases to 0.11

μ_B for q = +1 e and 1.51 μ_B for q = -1 e and becomes metal. The variation of M_T is due to the accommodation of different electronic charges of TMs-3d orbital states for different values of q.

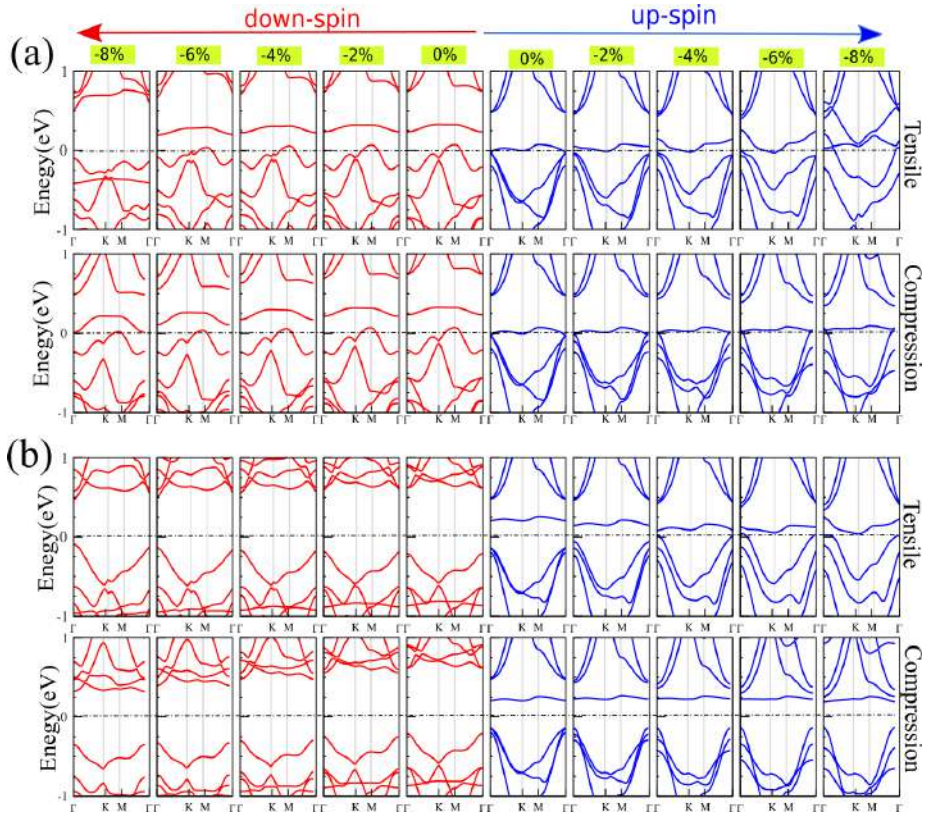

Figure 5.9: Electronic band structures of (a) Mn and (b) Fe adsorbed C_3N for different of uniaxial strain (tensile and compression). The E_F is set to zero.

The electronic band structure and DOS for Ti, Mn and Fe adatoms as a function of electric field is here investigated. The **F**= +1 and -1 V/Å denotes parallel and antiparallel to the z-axis, respectively, are shown in Fig. 5.7. and 5.8. The applied electric field effects on the electronic and magnetic properties of TMs/C_3N are significant and cause spin polarizations of TMs/C_3N show also considerable changes. In the case of Ti/C_3N, magnetic moments decreases to 2.37 μ_B with **F** = +1.0 V/Å, and increases to 2.74 μ_B for **F**= -1.0 V/Å. In both cases it remains a metal. For **F** = +1.0 V/Å, the charge on the Ti decreases with increasing **F** and Ti/C_3N remains metal and with **F** = -1.0 V/Å, the charge on the Ti increases with increasing value of **F** and excess electronic charge on the Ti is transferred from C atoms. The magnetic moment of Mn/C_3N decreases to 3.33 μ_B in **F** =

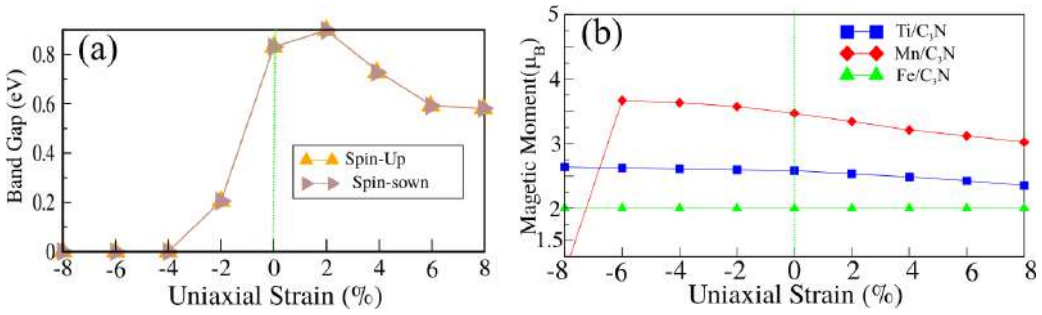

Figure 5.10: (a) Band gap as a function of uniaxial strain for Fe/C_3N. (b) Magnetic moment of TMs/C_3N (TM=Ti, Mn and Fe) as a function of uniaxial strain.

+1.0 V/Å, and increases to 3.62 μ_B in **F** = -1.0 V/Å. In both cases it remains metallic. But Fe/C_3N, will remain unchanged, whereas the energy band gap will be changed.

5.4.1 Strain effect on the adsorbed atom C_3N

The strain effects on the electronic and magnetic properties of the TMs/C_3N cause spin polarization. The band structure under uniaxial strain with tensile and compression states for Mn and Fe/C_3N in the $\uparrow$ and $\downarrow$ spin states, are shown in Figs. 5.9(a,b). The range of uniaxial strain is from -8% to $+8\%$. We see, that Mn/C_3N is initially a ferromagnetic-metal but becomes half-metal under compression larger than -8$\%$. While with increasing tensile strain, structure preserved ferromagnetic-metallic character. The Fe/C_3N is dilute-omagnetic semiconductors we see from Fig. 5.9(b), that C_3N transforms into a half-metal if the amount of compression strain is larger than -8$\%$. This differs from the case of Mn/C_3N, while Fe/C_3N, keeps its dilute-omagnetic semiconducting character with increasing strain to +8$\%$. Fig. 5.10(a), shows the variation of Fe/C_3N energy band gap with strain. The band gap with increase of uniaxial strain, decreases and becomes zero for compression, and remains scemiconductor with increasing tensile strain but band gap decreases for both $\uparrow$ and $\downarrow$ spin state. Variation of magnetic moment of Mn and Fe/C_3N as a function of uniaxial strain, is shown in Fig. 5.10(b). For Mn/C_3N, magnetic moments decreases from 3.5 μ_B to 3 μ_B with tensile strain +8$\%$, and increases to larger than 3 μ_B with increasing compression strain. The magnetic moment of Fe/C_3N is approximately constant in the range of -8% to $+8\%$. For Ti/C_3N, magnetic moment is approximately constant in the range of 0% to -8% and decreases for range of 0% to $+8\%$.

It is interesting to investigate the affect of uniaxial tensile and compressive strain on the electronic properties of C_3N. A schematic view of the boat-like conformation of SH-C_3N upon uniaxial strain, along the armchair and zigzag directions, is presented in Fig.

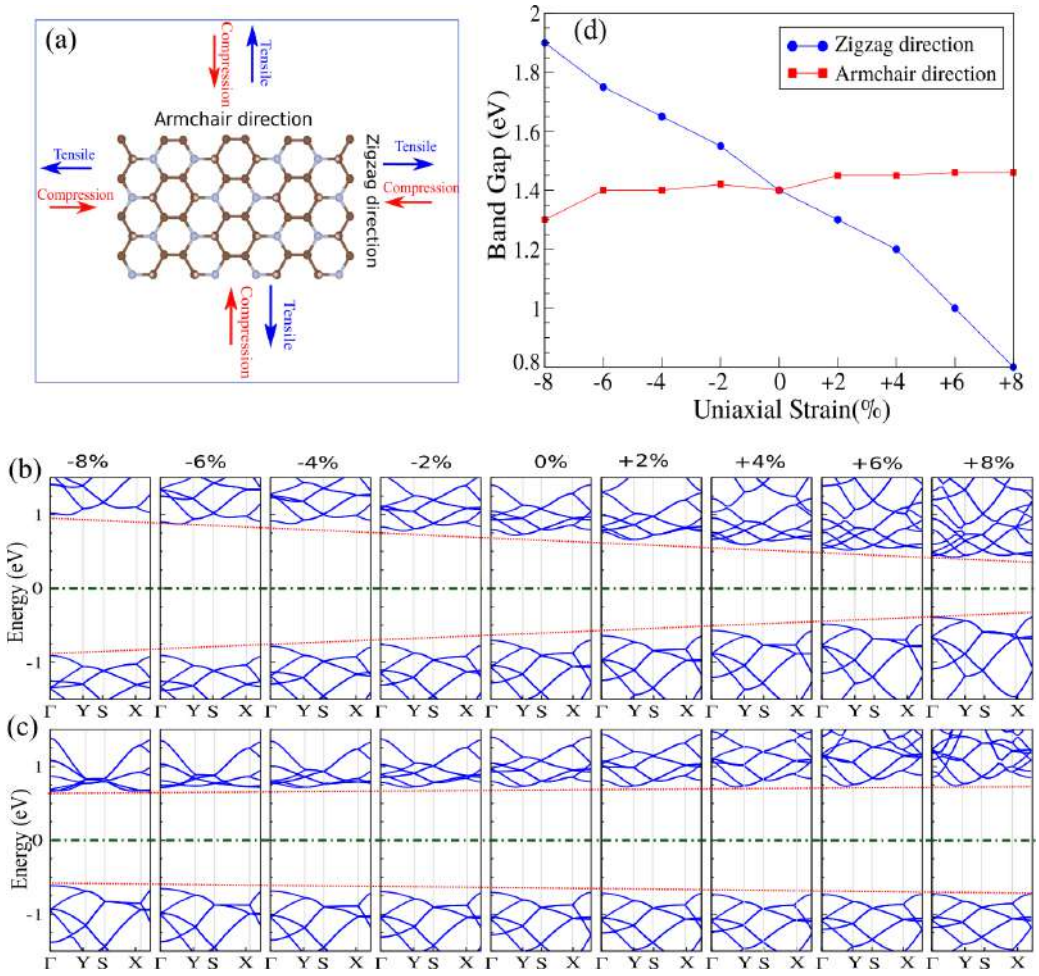

Figure 5.11: (a) Schematic view of the boat-like conformation of SH-C_3N upon uniaxial strain (tensile and compressive). Electronic band structure of SH-C_3N with the boat-like conformation as a function of uniaxial strains along the (b) zigzag and (c) armchair directions. (d) Variations of the band gap as a function of uniaxial strain.

5.11(a). The tensile and compressive strain is defined as $\varepsilon = (a - a_0)/a_0 \times 100$, where a and a_0 are the strained and equilibrium lattice constants, respectively. The electronic band structures of the boat-like conformation of SH-C_3N as a function of uniaxial strains (tensile and compressive), are shown in Figs. 5.11(b,c). For the zigzag direction, we see that electronic band structure changes systematicallly with ε (ε= -8, -6, -4, -2, 0, +2, +4, +6 and +8 %), namely the band gap decreases when ε varies from -8% to +8%. On increasing ε from zero to +8%, the band gap decreases from 1.4 eV to 0.8 eV in +8%.

For a huge strain of +14%, the system becomes metallic. For compressive strain, the band gap increases, specifically, when ε varies from zero to -8%, the band gap increases from 1.4 to 1.56 eV. in +8%. For the armchair direction, there is very little change in the band gap with strain. The variation of the energy band gap as a function of strain (tensile and compressive) is shown in Fig. 5.11(d). Thus it can be seen that the band gap is sensitive to structural strain particularly for the zigzag direction.

5.5 Conclusion

In summary, based on the first-principles calculations, we as systematically investigate the structural and electronic properties of a novel 2DM, with a stoichiometry of C_3N is recently synthesized. Firstly, we investigate the electronic property of few-layer C_3N with different stacking and layer numbers. Because of the interlayer coupling band gap depends on its stacking order between the layers and exhibits monotonically decreasing behavior as the layer number increases. Besides when we apply an uniform electric field on bilayer C_3N its band gap will decrease as the electric field changes and a semiconductor-to-metal transition may occur.

CHAPTER 6

Summary

In summary, based on first-principles calculations, i investigated the structural, electronic and magnetic properties of a novel 2D material, with stoichiometry C_3N that has been recently synthesized from carbonized organic single crystals. Two-dimensional polyaniline with structural unit C_3N is a semiconductor, which has attracted a lot of interest because of its unusual electronic, optoelectronic, thermal and mechanical properties that are potentially useful for various applications. The present study highlights that adatom adsorption on C_3N is a favorable approach to modulate its properties which may be relevant applications in catalysis, batteries and nanoelectronics. I investigated systematically the interaction between 27 different adatoms and the C_3N honeycomb structure. These adatoms lead to considerable modifications in the electronic structure, when the related adsorption energy is significant. In this case, the band gap of C_3N can be reduced and the system tune into a metal or semiconductor. The effect of charging, electric field and strain on the electronic and magnetic properties of C_3N were studied. My results show that the band gap and magnetic moment considerable changes with charging, applied electric field and strain. In this way it is possible to tune the electronic and magnetic properties.

Understanding the interaction between C_3N and adsorbate gas molecules is important for the exploitation of C_3N in e.g. gas sensors. In particular, using first principle calculations, the adsorption of common atmospheric (H_2, N_2, O_2, CO H_2O and H_2S) and polluted (CO, CO_2, NO, NO_2, SO_2, NH_3 and CH_4) gas molecules on C_3N was investigated. A detailed analysis of the optimized atomic structure and electronic properties of adsorption of those different molecules was carried out. The results showed that O_2, NO,

NO_2 and SO_2 are chemisorbed on C_3N and that the corresponding electronic structure of C_3N was modified. Adsorption of O_2 and SO_2 molecules, turns C_3N into a metal, while for NO_2 adsorption C_3N becomes a dilute-magnetic semiconductor with 0.6 μ_B magnetic moment. Our computational results show that other molecules including H_2, N_2, CO, CO_2, H_2O, H_2S, NH_3 and CH_4 are physisorbed causing little distortion of C_3N. The amount of charge transfer upon adsorption of these gas molecules are found to be small. Our theoretical studies indicate that C_3N-based sensor has a high potential for O_2, NO, NO_2 and SO_2 detection due to the significant electronic structure changes with moderate adsorption energy.

Functionalization by atoms is widely believed to be an effective way to improve and tune the properties of two-dimensional materials. I investigated discussed the modifications that occur in the electronic structure of C_3N when adsorbed with different coverages of H and O atoms. Our results show that the electronic band gap depends on the amount of coverage, and also that the electronic and magnetic structure are significantly affected by the configuration of two-H clusters/pairs (ortho, meta and para) . These structures exhibit diverse electronic characteristics, from metal to semiconductor and induce magnetism in some of the configurations. We considered various super cell in order to investigate magnetism in $C_3NH_{0.125}$. The magnetic state for $C_3NH_{0.125}$ exhibit ferromagnetism. Furthermore, we investigated effects of semi and full functionalization (with two types of configurations 'chair-' and 'boat-like') for adsorption of H, O and F atoms on C_3N and found how the electronic and magnetic properties of C_3N are modified. From C_3N to semi-hydrogenated C_3N and then to fully-hydrogenated C_3N, the system changes from semiconducting to metallic and then to insulating. In addition, the electronic and magnetic properties of the resulting semi/fully hydrogenated C_3N can be further controlled by introducing H atom vacancies, which result in metallic, dilute-magnetic semiconductor and ferromagnetic insulator behavior depending on the particular side of the H-vacancy and the vacancy concentration. Thus, creation of H vacancies is an effective method to control the magnetism in the semi and fully functionalization of C_3N. Finally, we studied the interaction of H and O atoms with zigzag and armchair C_3N nanoribbon. Adsorption of H can lead to considerable modifications in the electronic structure. Under these conditions, either the wide band gap of the C_3N nanoribbon with two difference types of zigzag and armchair, can be reduced or diminished and the C_3N nanoribbons becomes metal or semiconductor with an induced magnetic moment. I also investigate the effect of strain on the properties of hydrogenated C_3N. I showed that the band gap could be modulated with strain, offering the potential to control e.g. its optical properties.

Next we investigated the effect of topological defects including single and double vacancies, Stone-Wales and anti-site, on the structure and electronic properties of C_3N. Our results show that for both single and double vacancies C_3N becomes a metal, except in the

case of a single vacancy of N and double vacancy of N+N. C_3N with anti-site defects turns C_3N into a direct semiconductor with 0.2 eV band gap. With Stone-Wales defects, C_3N becomes an indirect semiconductor with band gap of 0.2 eV. Subsequently, we studied the effects due to H, O, S, F, Cl, B, C, N, Si, P, Li, Na, K, Be, Mg, Ca and Al substitution on the electronic properties of C_3N. When the C site is substituted with O, S and Si atoms, the system remains a semiconductor with band gap in the range of 0.25-0.75 eV, while with H, Cl, B, P, Li, Na, K, Be and Mg atoms the system turns into a metal. Also, upon substitution of the native C with F atom, C_3N becomes a dilute-magnetic semiconductor, while with Ca substitution it is a ferromagnetic-metal. Moreover, when N is replaced with H, O, S, C, Si, P, Li and Be atoms the system turns into a metal and with F, Cl, B and Al atoms becomes a semiconductor. With Mg and Ca atoms it becomes a ferromagnetic-metal and half-metal with induces magnetic moments of 0.3 μ_B and 2 μ_B, respectively. In addition, with Na and K substitution we predict that C_3N becomes a spin-glass semiconductor. Moreover, we investigated the effect of charging and strain on the electronic structure of C_3N, when native C and N atoms are substituted with Na atom. We found that it is possible to tune the magnetism by controlling the Fermi level via external fields such as by charging and strain. The effect of different stacking and layer numbers on the electronic property of few-layer C_3N was studied. Because of the interlayer coupling the band gap depends on its stacking order between the layers and exhibits monotonically decreasing behavior as the layer number increases. Besides when we apply an uniform electric field on bilayer C_3N its band gap will decrease as the electric field changes and a semiconductor-to-metal transition may occur. Furthermore, the effects of nanoribbon width/length and nanotube width/diameter on structure, and electronic properties of C_3N are investigated.

CHAPTER 7

Samenvatting

Op basis van 'first principle' berekeningen, hebben we de structurele, elektronische en magnetische eigenschappen van een nieuw 2D-materiaal onderzocht, met stoichiometrie C_3N die onlangs is gesynthetiseerd uit gecarboniseerde organische kristallen. Tweedimensionale polyaniline met structurele eenheid C_3N is een halfgeleider, die in de belangstelling is gekomen vanwege zijn ongebruikelijke elektronische, opto-elektronische, thermische en mechanische eigenschappen die kunnen nuttig zijn voor verschillende toepassingen. Mijn studie vond dat de adsorptie van adatomen aan C_3N de eigenschappen ervan kon moduleren, dat relevant is voor toepassingen in katalyse, batterijen en nano-elektronica. We onderzochten systematisch de interactie tussen 27 verschillende adatomen en de honingraatstructuur C_3N. Deze adatomen leiden tot aanzienlijke wijzigingen in de elektronische structuur, wanneer de gerelateerde adsorptie-energie aanzienlijk is. Onder deze omstandigheden kan de bandkloof van C_3N worden verkleind en wordt het systeem metaal of halfgeleider. Het effect van het introduceren van lading en van een elektrisch veld op de elektronische en magnetische eigenschappen van C_3N werd berekend. Onze resultaten laten zien dat de bandkloof en het magnetische moment aanzienlijk veranderen met het introduceren van lading, of het aanleggen van een elektrisch veld.

Inzicht in de interactie tussen C_3N en adsorbaat gasmoleculen is belangrijk voor de exploitatie van C_3N in b.v. gas sensoren. Met behulp van eerste principepe berekeningen, werd de adsorptie van de atmosferische (H_2, N_2, O_2, CO, H_2O en H_2S) en giftige (CO, CO_2, NO, NO_2, SO_2, NH_3 en CH_4) gasmoleculen op C_3N onderzocht. Een gedetailleerde analyse van de geoptimaliseerde atoomstructuur en elektronische eigenschappen

van adsorptie van verschillende moleculen werd uitgevoerd. De resultaten toonden aan dat O_2, NO, NO_2 en SO_2 chemisch geadsorbeerd zijn op C_3N. Er werd ook vastgesteld dat de overeenkomstige elektronische structuur van C_3N werd gewijzigd. Adsorptie van O_2 en SO_2 moleculen maakt van C_3N een metaal, terwijl onder NO_2 adsorptie verkrijgen we een verdunde magnetische halfgeleider met 0.6 μ_B magnetisch moment. Onze resultaten tonen aan dat andere moleculen waaronder H_2, N_2, CO, CO_2, H_2O, H_2S, NH_3 en CH_4 fysisch geabsorbeerd zijn. De hoeveelheid ladingoverdracht bij adsorptie van deze gasmoleculen blijkt klein te zijn. Onze theoretische studies geven aan dat een op C_3N gebaseerde sensor een groot potentieel heeft voor O_2, NO, NO_2 en SO_2 detectie vanwege de significante verandering van de elektronische structuur met kleine adsorptie-energie.

Functionalisatie door atomen wordt algemeen beschouwd als een effectieve manier om de eigenschappen van tweedimensionale materialen te veranderen. We bestudeerde de veranderingen in de elektronische structuur van C_3N wanneer geadsorbeerd met H- en O-atomen. Onze resultaten laten zien dat de waarde van de elektronische bandkloof afhankelijk is van de dekking, en ook dat de elektronische en magnetische structuur aanzienlijk worden beinvloed door de configuratie van twee-H-clusters/paren (ortho, meta en para). The elektronische structuur is een metaal of halfgeleider en magnetisme wordt geinduceerd in sommige configuraties. We hebben verschillende grote supercellen beschouwd voor het onderzoek van magnetisme in $C_3NH_{0.125}$. De magnetische toestand van $C_3NH_{0.125}$ is een ferromagneet. Verder onderzochten we effecten van semi- en volledige functionalisatie (met twee typen van configuraties 'stoel-' en 'boot-achtig') voor adsorptie van H-, O- en F-atomen op C_3N en ontdekten hoe de elektronische en magnetische eigenschappen C_3N zijn gewijzigd. Van C_3N naar semi-gehydrogeneerde C_3N en vervolgens naar volledig gehydrogeneerde C_3N, vonden we dat het systeem verandert van halfgeleidend naar metallisch en vervolgens naar isolerend. Bovendien kunnen de elektronische en magnetische eigenschappen van de resulterende semi/volledig gehydrogeneerde C_3N worden bepaald door H-atoom vacatures. Dit leidt tot een metal, verdunde magnetische halfgeleider en ferromagnetische isolator, afhankelijk van de zijde waar de H-vacature is gecreeerd en van de vacature-concentratie. Ten slotte hebben we de interactie van H- en O-atomen met zigzag en armchair C_3N nanoribbon bestudeerd. Adsorptie van H kan leiden tot aanzienlijke wijzigingen in de elektronische structuur. Onder deze omstandigheden kan de grote bandkloof van de C_3N nanoribbon met twee verschillende soorten zigzag en armchair worden verkleind.

Vervolgens onderzochten we het effect van topologische defecten, waaronder enkele en dubbele vacatures, Stone-Wales en anti-site, op de structuur en elektronische eigenschappen van C_3N. Onze resultaten laten zien dat voor zowel enkele als dubbele vacatures C_3N een metaal wordt, behalve in het geval van een enkele vacature van N en dubbele vacature van N+N. C_3N met anti-site-defecten in C_3N resulteert in een directe halfgeleider met een

bandkloof van 0.2 eV. Met Stone-Wales-defecten wordt C_3N een indirecte halfgeleider met een bandkloof van 0.2 eV. Verder hebben we de effecten onderzocht van H, O, S, F, Cl, B, C, N, Si, P, Li, Na, K, Be, Mg, Ca en Al substitutie op de elektronische eigenschappen van C_3N. Wanneer C wordt gesubstitueerd met O-, S- en Si-atomen, blijft het systeem een halfgeleider met een bandkloof van 0.25-0.75 eV, terwijl met H, Cl, B, P, Li, Na, K, Be en Mg atomen verandert het systeem in een metaal. Ook wordt bij vervanging van C door het F-atoom C_3N een verdunde magnetische halfgeleider, terwijl bij Ca-substitutie we een ferromagnetisch metaal voorpellen. Wanneer N wordt vervangen door H-, O-, S-, C-, Si-, P-, Li- en Be-atomen verandert het systeem bovendien in een metaal en voor F-, Cl-, B- en Al-atomen wordt het een halfgeleider. Met Mg- en Ca-atomen wordt het een ferromagnetisch metaal en een halfmetaal met magnetische momenten van respectievelijk 0.3 en 2 μ_B. Met Na en K bekomen we een spin-glas halfgeleider. Bovendien onderzochten we het effect van lading en spanning op de elektronische structuur van C_3N, waarbij ÂăC- en N-atomen worden vervangen door Na.

We onderzochten de elektronische eigenschap van verschillende lagen C_3N voor verschillende stapel configuraties. Vanwege de tussenlaag is de koppelingsbandafstand afhankelijk van de stapelvolgorde tussen de lagen en vertoont deze een monotoon afnemend gedrag naarmate het aantal lagen toeneemt. Bovendien, wanneer we een uniform elektrisch veld aanbrengen, wordt de bandkloof Âăkleiner naarmate het elektrische veld verandert en er een overgang van halfgeleider naar metaal kan optreden. Vervolgens worden de effecten van de breedte/lengte van de nanoribbon op de structuur en de elektronische eigenschappen van C_3N onderzocht. We vonden hoe de elektronische structuur van een C_3N nanoribbon afhankelijk is van de breedte, lengte en diameter. Bovendien wordt de adsorptie van het H-atoom op C_3N nanostructuren bestudeerd en vonden dat dit kan leiden tot aanzienlijke wijzigingen in de elektronische structuur, warreer de gerelateerde adsorptie-energie aanzienlijk is. Ons resultaat laat zien dat de bandkloof en het magnetische moment met aangelegde lading, elektrisch veld en spanning, aanzienlijke veranderingen kunnen ondergaan. Het is mogelijk om de elektronische en magnetische eigenschappen te manipuleren door het Fermi-niveau te regelen of door het elektrische veld te veranderen.

Bibliography

[1] X. Li, L. Tao, Z. Chen, H. Fang, X. Li, X. Wang, J. B. X. H. Zhu, and Hongwei, "Graphene and related two-dimensional materials: Structure-property relationships for electronics and optoelectronics," *Appl. Phys. Rev.*, vol. 4, no. 2, p. 021306, 2017.

[2] F. Wang, Z. Wang, Q. Wang, F. Wang, L. Yin, K. Xu, Y. Huang, and J. He, "Synthesis, properties and applications of 2D non-graphene materials," *Nanotechnology*, vol. 26, no. 29, p. 292001, 2015.

[3] P. Miro, M. Audiffred, and T. Heine, "An atlas of two-dimensional materials," *Chem. Soc. Rev.*, vol. 43, pp. 6537–6554, 2014.

[4] B. Anasori, M. Lukatskaya, and Y. Gogotsi, "2D metal carbides and nitrides (mxenes) for energy storage," *Nat. Rev. Mater.*, vol. 2, p. 16098, 2017.

[5] A. K. Geim and I. V. Grigorieva, "Van der waals heterostructures," *Nat.*, vol. 499, pp. 419–425, 2013.

[6] J. Mahmood, E. K. Lee, M. Jung, D. Shin, H. J. Choi, J. M. Seo, S. M. Jung, D. Kim, F. Li, M. S. Lah, N. Park, H. J. Shin, J. Oh, and J. B. Baek, "Two-dimensional polyaniline (C_3N) from carbonized organic single crystals in solid state," *PNAS*, vol. 113, pp. 7414–7419, 2016.

[7] K. S. Novoselov, A. K. Geim, S. V. Morozov, D. Jiang, S. V. D. Y. Zhang, I. V. Grigorieva, and A. A. Firsov, "Electric field effect in atomically thin carbon films," *Science*, vol. 306, no. 5696, pp. 666–669, 2004.

[8] H. Kroemer, "Nobel lecture: Quasielectric fields and band offsets: teaching electrons new tricks," *Rev. Mod. Phys.*, vol. 73, pp. 783–793, 2001.

[9] R. P. Feynman, *The Arabidopsis Book*. American Society of Plant Biologist, 2002.

[10] P. R. Wallace, "The band theory of graphite," *Phys. Rev.*, vol. 71, pp. 622–634, 1947.

[11] H. P. Boehm, A. Clauss, G. O. Fischer, , and U. Hofmann, "The band theory of graphite," *Zeitschrift fur Naturforschung B*, vol. 17, pp. 150–153, 1962.

[12] J. Shelton, H. Patil, and J. Blakely, "Equilibrium segregation of carbon to a nickel (111) surface: A surface phase transition," *Surf. Sci.*, vol. 43, no. 2, pp. 493–520, 1974.

[13] A. V. Bommel, J. Crombeen, and A. V. Tooren, "Leed and auger electron observations of the SiC(0001) surface," *Surf. Sci.*, vol. 48, no. 2, pp. 463–472, 1975.

[14] X. Lu, M. Yu, H. Huang, and R. R. S, "Tailoring graphite with the goal of achieving single sheets," *Nanotechnology*, vol. 10, no. 3, pp. 269–272, 1999.

[15] E. Fitzer, K. H. Kochling, H. P. Boehm, , and H. Marsh, "Recommended terminology for the description of carbon as a solid (iupac recommendations 1995)," *Pure Appl. Chem.*, vol. 67, no. 3, pp. 473–506, 1995.

[16] D. Jariwala, V. K. Sangwan, L. J. Lauhon, T. J. Marks, and M. C. Hersam, "Carbon nanomaterials for electronics, optoelectronics, photovoltaics, and sensing," *Chem. Soc. Rev.*, vol. 42, pp. 2824–2860, 2013.

[17] X. Li, Z. Lv, and H. Zhu, "Carbon/silicon heterojunction solar cells: State of the art and prospects," *Adv. Mater.*, vol. 27, no. 42, pp. 6549–6574, 2015.

[18] M. S. Xu, T. Liang, M. M. Shi, and H. Chen, "Electronics and optoelectronics of two-dimensional transition metal dichalcogenides," *Chem. Rev.*, vol. 113, pp. 3766–98, 2013.

[19] J. A. Wilson and A. D. Yoffe, "Van der waals heterostructures," *Adv. Phys.*, vol. 18, pp. 193–335, 1969.

[20] X. Huang, Z. Zeng, and H. Zhang, "Metal dichalcogenide nanosheets: preparation, properties and applications," *Chem. Soc. Rev.*, vol. 42, pp. 1934–1946, 2013.

[21] Q. H. Wang, K. Kalantar-Zadeh, A. Kis, J. N. Coleman, and M. S. Strano, "Electronics and optoelectronics of two-dimensional transition metal dichalcogenides," *Nat. Nanotechnology*, vol. 7, pp. 699–712, 2012.

[22] S. Z. Butler, S. M. Hollen, L. Cao, Y. Cui, H. R. G. J. A. Gupta, T. F. Heinz, S. S. Hong, J. Huang, A. F. Ismach, E. Johnston-Halperin, M. Kuno, V. V. Plashnitsa, R. D. Robinson, R. S. Ruoff, S. Salahuddin, J. Shan, L. ShiMichael, G. Spencer, M. Terrones, W. Windl, and J. E. Goldberger, "Progress, challenges, and opportunities in two-dimensional materials beyond graphene," *ACS Nano*, vol. 7, no. 4, pp. 2898–2926, 2013.

[23] L. F. Mattheiss, "Band structures of transition-metal-dichalcogenide layer compounds," *Phys. Rev. B*, vol. 8, pp. 3719–3740, Oct 1973.

[24] D. J. Late, B. Liu, J. Luo, A. Yan, H. S. S. R. Matte, M. Grayson, C. N. R. R. Vinayak, and P. Dravid, "Gas and gase ultrathin layer transistors," *Adv. Mater.*, vol. 24, pp. 3549–54, 2012.

[25] D. J. Late, B. Liu, H. S. S. R. Matte, C. N. R. Rao, and V. P. Dravid, "Rapid characterization of ultrathin layers of chalcogenides on $SiO_2/textSi$ substrates," *Adv. Funct. Mater.*, vol. 22, pp. 1894–905, 2012.

[26] A. S. A. Yamamoto, K. T. T. Goto, E. Kulatov, K. Ohno, Y. Kawazoe, K. Uchida, and N. Miura, "Excitons and band structure of highly anisotropic GaTe single crystals," *Phys. Rev. B*, vol. 64, p. 035210, Jun 2001.

[27] D.-J. Xue, J.-S. H. J. Tan, W. Hu, Y.-G. Guo, and L.-J. Wan, "Anisotropic photoresponse properties of single micrometer-sized GeSe nanosheet," *Adv. Mater.*, vol. 24, no. 33, pp. 4528–4533, 2012.

[28] L. H. C. Li, G. P. Snigdha, Y. F. Yu, and L. Y. Cao, "Role of boundary layer diffusion in vapor deposition growth of chalcogenide nanosheets: The case of GeS," *ACS Nano*, vol. 6, pp. 8868–8877, 2012.

[29] J. E. Moore and L. Balents, "Topological invariants of time-reversal-invariant band structures," *Phys. Rev. B*, vol. 75, p. 121306, Mar 2007.

[30] X.-L. Qi, T. L. Hughes, and S.-C. Zhang, "Topological field theory of time-reversal invariant insulators," *Phys. Rev. B*, vol. 78, p. 195424, Nov 2008.

[31] D. S. Kong and Y. Cui, "Opportunities in chemistry and materials science for topological insulators and their nanostructures," *Nat. Chem.*, vol. 3, pp. 845–9, 2011.

[32] X.-L. Qi and S.-C. Zhang, "Topological insulators and superconductors," *Rev. Mod. Phys.*, vol. 83, pp. 1057–1110, Oct 2011.

[33] M. Z. Hasan and C. L. Kane, "Colloquium: Topological insulators," *Rev. Mod. Phys.*, vol. 82, pp. 3045–3067, Nov 2010.

[34] B. A. Bernevig, T. L. Hughes, and S.-C. Zhang, "Quantum spin hall effect and topological phase transition in HgTe quantum wells," *Science*, vol. 314, no. 5806, pp. 1757–1761, 2006.

[35] C.-X. Liu, X.-L. Qi, H. Zhang, X. Dai, Z. Fang, and S.-C. Zhang, "Model hamiltonian for topological insulators," *Phys. Rev. B*, vol. 82, p. 045122, Jul 2010.

[36] Y. Xia, D. Qian, D. Hsieh, L. Wray, A. Pal, H. Lin, A. Bansil, D. Grauer, Y. S. Hor, R. J. Cava, and M. Z. Hasan, "Observation of a large-gap topological-insulator class with a single dirac cone on the surface," *Nat. Phys.*, vol. 5, pp. 398–402, 2009.

[37] Y. Zhang, C.-Z. C. K. He, C.-L. Song, L.-L. Wang, X. Chen, J.-F. Jia, Z. Fang, X. Dai, W.-Y. Shan, S.-Q. Shen, Q. Niu, X.-L. Qi, S.-C. Zhang, X.-C. Ma, and Q.-K. Xue, "Crossover of the three-dimensional topological insulatorBi_2Se_2 to the two-dimensional limit," *Nat. Phys.*, vol. 6, pp. 584–588, 2010.

[38] D. S. Kong, W. H. Dang, J. J. Cha, H. Li, S. Meister, H. L. Peng, Z. F. Liu, and Y. Cui, "Few-layer nanoplates of Bi_2Se_2 and Bi_2Te_2 with highly tunable chemical potential," *Nano Lett.*, vol. 10, pp. 2245–2250, 2010.

[39] L. K. Li, Y. J. Yu, G. J. Ye, Q. Q. Ge, X. D. Ou, H. Wu, D. L. Feng, X. H. Chen, and Y. B. Zhang, "Black phosphorus field-effect transistors," *Nano Lett.*, vol. 9, pp. 372–377, 2014.

[40] R. W. Keyes, "The electrical properties of black phosphorus," *Phys. Rev.*, vol. 92, pp. 580–584, Nov 1953.

[41] P. Vogt, P. D. Padova, C. Quaresima, J. Avila, E. Frantzeskakis, M. C. Asensio, A. Resta, B. Ealet, and G. L. Lay, "Silicene: Compelling experimental evidence for graphenelike two-dimensional silicon," *Phys. Rev. Lett.*, vol. 108, p. 155501, Apr 2012.

[42] M. E. Davila, L. Xian, S. Cahangirov, A. Rubio, and G. L. Lay, "Germanene: a novel two-dimensional germanium allotrope akin to graphene and silicene," *New J. Phys.*, vol. 16, p. 095002, 2004.

[43] B. van den Broek, M. Houssa, E. Scarlise, G. Pourtois, V. V. Afanasev, and A. Stesmans, "Germanene: a novel two-dimensional germanium allotrope akin to graphene and silicene," *2D Mater.*, vol. 1, p. 021004, 2004.

[44] J. O. Sofo, A. S. Chaudhari, and G. D. Barber, "Graphane: A two-dimensional hydrocarbon," *Phys. Rev. B*, vol. 75, p. 153401, 2007.

[45] D. C. Elias, R. R. Nair, T. M. G. Mohiuddin, S. V. Morozov, P. Blake, M. P. Halsall, A. C. Ferrari, D. W. Boukhvalov, M. I. Katsnelson, A. K. Geim, and K. S. Novoselov, "Graphane: A two-dimensional hydrocarbon," *Science*, vol. 323, pp. 610–613, 2010.

[46] R. R. Nair, W. C. Ren, R. Jalil, I. Riaz, V. G. Kravets, L. Britnell, P. Blake, F. Schedin, A. S. Mayorov, S. J. Yuan, M. I. Katsnelson, H. M. Cheng, W. Strupinski, L. G. Bulusheva, A. V. Okotrub, I. V. Grigorieva, A. N. Grigorenko, K. S. Novoslov, and A. K. Geim, "Stability and exfoliation of germanane: a germanium graphane analogue," *Small*, vol. 6, pp. 2877–2884, 2010.

[47] J. T. Robinson, J. S. Burgess, C. E. Junkermeier, S. C.Badescu, T. L. Reinecke, F. K. Perkins, M. K. Zalalutdniov, J. W. Baldwin, J. C. Culbertson, P. E. Sheehan, and E. S. Snow, "Stability and exfoliation of germanane: a germanium graphane analogue," *Nano Lett.*, vol. 10, pp. 3001–3005, 2010.

[48] M. Springborg and J.-O. Joswig, eds., *Chemical Modelling*, vol. 11 of *SPR - Chemical Modelling*. The Royal Society of Chemistry, 2015.

[49] A. P. Nayak, T. Pandey, D. Voiry, J. Liu, S. T. Moran, A. Sharma, C. Tan, C.-H. Chen, L.-J. Li, M. Chhowalla, J.-F. Lin, A. K. Singh, and D. Akinwande, "Pressure-dependent optical and vibrational properties of monolayer molybdenum disulfide," *Nano Lett.*, vol. 15, pp. 346–353, 2015.

[50] G. Eda, T. Fujita, H. Yamaguchi, D. Voiry, M. Chen, and M. Chhowalla, "Pressure-dependent optical and vibrational properties of monolayer molybdenum disulfide," *ACS Nano*, vol. 6, pp. 7311–7317, 2012.

[51] M. Naguib, O. Mashtalir, J. Carle, V. Presser, J. Lu, L. Hultman, Y. Gogotsi, and M. W. Barsoum, "Two-dimensional transition metal carbides," *ACS Nano*, vol. 6, pp. 1322–1331, 2012.

[52] M. Naguib, M. Kurtogly, V. Presser, J. Lu, J. Niu, M. Heon, L. Hultman, Y. Gogotsi, and M. W. Barsoum, "Two-dimensional transition metal carbides," *Adv. Mater.*, vol. 23, pp. 4248–4253, 2011.

[53] M. Khazaei, M. Arai, T. S. andC. Y. Chung, N. S. Venkataramanan, M. Estili, Y. Sakka, and Y. Kawazoe, "Novel electronic and magnetic properties of two-dimensional transition metal carbides and nitrides," *Adv. Funct. Mater.*, vol. 23, pp. 2185–2192, 2013.

[54] J. Li, W. Cui, Y. Sun, Y. Chu, W. Cen, and F. Dong, "Directional electron delivery via a vertical channel between g-C_3N_4 layers promotes photocatalytic efficiency," *J. Mater. Chem. A*, vol. 5, pp. 9358–9364, 2017.

[55] Y. Zheng, J. L. Liu, J. Jaroniec, and M. Qiao, "Graphitic carbon nitride materials: Controllable synthesis and applications in fuel cells and photocatalysis," *Energy Environ. Sci.*, vol. 5, pp. 6717–6731, 2012.

[56] A. Thomas, A. Fischer, F. Goettmann, M. Antonietti, J.-O. Muller, and J. C. R. Schlogl and, "Graphitic carbon nitride materials: variation of structure and morphology and their use as metal-free catalysts," *J. Mater. Chem.*, vol. 18, p. 4893, 2008.

[57] Y. Zheng, Y. Jiao, J. Chen, J. Liu, J. Liang, A. Du, W. Zhang, S. S. Z. Zhu, M. Jaroniec, G. Lu, and S. Qiao, "Nanoporous graphitic-C_3N_4 carbon metal-free electrocatalysts for highly efficient oxygen reduction," *J. Am. Chem. Soc.*, vol. 133, pp. 20116–20119, 2011.

[58] S. Lyth, Y. Nabae, S. Moriya, S. Kuroki, M. Kakimoto, J. Ozaki, and S. Miyata, "Carbon nitride as a nonprecious catalyst for electrochemical oxygen reduction," *J. Phys. Chem. C*, vol. 113, pp. 20148–20151, 2009.

[59] A. Rajabpour, S. Bazrafshan, and S. Volz, "Carbon-nitride 2D nanostructures: Thermal conductivity and interfacial thermal conductance with the silica substrate," *Phys. Chem. Chem. Phys.*, vol. 21, pp. 2507–2512, 2019.

[60] M. Javeed, L. E. Kwang, J. Minbok, S. Dongbin, J. In-Yup, J. Sun-Min, C. Hyun-Jung, S. Jeong-Min, B. Seo-Yoon, P. N. S. So-Dam, O. J. Hak, S. Hyung-Joon, and B. Jong-Beom, "Nitrogenated holey two-dimensional structures," *Nat. Commun.*, vol. 6, p. 6486, 2015.

[61] B. Mortazavi, O. Rahaman, T. Rabczuk, and L. F. C. Pereira, "Thermal conductivity and mechanical properties of nitrogenated holey graphene," *Carbon*, vol. 106, pp. 1–8, 2016.

[62] B. Mortazavi, "Ultra high stiffness and thermal conductivity of graphene like C_3N," *Carbon*, vol. 118, pp. 25–34, 2017.

[63] M. Makaremi, B. Mortazavi, and C. V. Singh, "Adsorption of metallic, metalloidic, and nonmetallic adatoms on two-dimensional C_3N," *Phys. Chem. C.*, vol. 121, pp. 18575–18583, 2017.

[64] M. Tagani, "Electrical and mechanical properties of a fully hydrogenated two-dimensional polyaniline sheet," *Comput. Mater. Sci.*, vol. 153, pp. 126–133, 2018.

[65] S. H. M.D. Esrafili, "Catalytic reduction of nitrous oxide over boron-doped C_3N monolayers: A DFT study," *Chem. Phys. Lett.*, vol. 725, pp. 52–58, 2019.

[66] O. Faye, T. Hussain, A. Karton, and J. Szpunar, "Tailoring the capability of carbon nitride (C_3N) nanosheets toward hydrogen storage upon light transition metal decoration," *Nanotechnology*, vol. 30, p. 75404, 2018.

[67] Z. Guizhi, L. Kun, S. Qiang, K. Yoshiyuki, and J. Puru, "Lithium-doped triazine-based graphitic C_3N_4 sheet for hydrogen storage at ambient temperature," *Comput. Mater. Sci.*, vol. 81, pp. 275–279, 2014.

[68] X. Li, S. Zhang, and Q. Wang, "Stability and physical properties of a tri-ring based porous g-C_4N_3 sheet," *Phys. Chem. Chem. Phys.*, vol. 15, pp. 7142–7146, 2013.

[69] A. J. Mannix, B. Kiraly, M. C. Hersam, and N. P. Guisinger, "Synthesis and chemistry of elemental 2D materials," *Nat. Rev. Chemi.*, vol. 1, p. 0014, 2017.

[70] A. Du, S. Sanvito, and S. C. Smith, "First-principles prediction of metal-free magnetism and intrinsic half-metallicity in graphitic carbon nitride," *Phys. Rev. Lett.*, vol. 108, p. 197207, 2012.

[71] T. Hu, A. Hashmi, and J. Hong, "Transparent half metallic g-C_4N_3 nanotubes: Potential multifunctional applications for spintronics and optical devices," *Sci. Rep.*, vol. 4, p. 6059, 2014.

[72] A. Hashmi and J. Hong, "Metal free half metallicity in 2D system: Structural and magnetic properties of g-C_4N_3 on BN," *Sci. Rep.*, vol. 4, p. 4374, 2014.

[73] X. Zhang, M. Zhao, X. W. A. Wang, and A. Du, "Spin-polarization and ferromagnetism of graphitic carbon nitride materials," *J. Mater. Chem. C.*, vol. 1, pp. 6265–6270, 2013.

[74] Q. Y. Q. Guo, C. Yi, L. Zhu, and Y. Xie, "Synthesis of carbon nitrides with graphite-like or onion-like lamellar structures via a solvent-free route at low temperatures," *Carbon*, vol. 43, pp. 1386–1391, 2005.

[75] C. C. J. Li, J. Hao, H. Qiu, H. Xu, and H. Zhu, "Self-assembled One-Dimensional carbon nitride architectures," *Diamond and Related Mater.*, vol. 15, pp. 1593–1600, 2006.

[76] H. Qiu, Z. Wang, and X. Sheng, "First-Principles prediction of an intrinsic half-metallic graphitic hydrogenated carbon nitride," *Phys. Lett. A.*, vol. 377, pp. 347–350, 2013.

[77] A. Wang, X. Zhang, and M. Zhao, "Topological insulator states in a honeycomb lattice of s-triazines," *Nanoscale*, vol. 6, pp. 11157–11162, 2014.

[78] V. Arkady, J. P. Rabe, U. Kaiser, A. I. Cooper, A. Thomas, M. J. Bojdys, G. Algara-Siller, N. Severin, S. Y. Chong, T. Bjorkman, R. G. Palgrave, A. Laybourn, M. Antonietti, Y. Z. Khimyak, and A. V. Krasheninnikov, "Triazine-based graphitic carbon nitride: A two-dimensional semiconductor," *Angewandte Chemie*, vol. 126, pp. 7580–7585, 2014.

[79] H. Sahin, C. Cahangirov, M. Topsakal, E. Bekaroglu, E. Akturk, R. T. Senger, and S. Ciraci, "Monolayer honeycomb structures of group-IV elements and III-V binary compounds: First-principles calculations," *Phys. Rev. B*, vol. 80, p. 155453, 2009.

[80] H. L. Zhuang, A. K. Singh, and R. G. Hennig, "Computational discovery of single-layer III-V materials," *Phys. Rev. B*, vol. 87, p. 165415, 2013.

[81] F. Banhart, J. Kotakoski, and A. V. Krasheninnikov, "Structural defects in graphene," *ACS Nano*, vol. 5, pp. 26–41, 2011.

[82] A. Hashimoto, K. Suenaga, A. Gloter, K. Urita, and S. Iijima, "Direct evidence for atomic defects in graphene layers," *Nature*, vol. 430, pp. 870–873, 2004.

[83] L. Li, S. Reich, and J. Robertson, "Defect energies of graphite: Density-functional calculations," *Phys. Rev. B*, vol. 72, p. 184109, Nov 2005.

[84] J. C. Meyer, C. Kisielowski, R. Erni, M. D. Rossell, M. F. Crommie, and A. Zettl, "Direct imaging of lattice atoms and topological defects in graphene membranes," *Nano Lett.*, vol. 8, pp. 3582–3586, 2008.

[85] P. O. Lehtinen, A. S. Foster, A. Ayuela, A. Krasheninnikov, K. Nordlund, and R. M. Nieminen, "Magnetic properties and diffusion of adatoms on a graphene sheet," *Phys. Rev. Lett.*, vol. 91, p. 017202, Jun 2003.

[86] A. V. Krasheninnikov, P. O. Lehtinen, A. S. Foster, P. Pyykkö, and R. M. Nieminen, "Embedding transition-metal atoms in graphene: Structure, bonding, and magnetism," *Phys. Rev. Lett.*, vol. 102, p. 126807, Mar 2009.

[87] L. Ci, L. Song, C. Jin, D. Jariwala, D. Wu, Y. Li, A. Srivastava, Z. F. Wang, K. Storr, L. Balicas, F. Liu, and P. M. Ajayan, "Atomic layers of hybridized boron nitride and graphene domains," *Nat. Mater.*, vol. 9, pp. 430–435, 2010.

[88] J. B. Oostinga, H. B. Heersche, X. Liu, A. F. Morpurgo, and L. M. K. Vandersypen, "Gate-induced insulating state in bilayer graphene devices," *Nat. Mater.*, vol. 7, pp. 151–157, 2010.

[89] A. Splendiani, L. Sun, Y. Zhang, T. Li, J. Kim, C.-Y. Chim, G. Galli, and F. Wang, "Emerging photoluminescence in monolayer MoS_2," *Nano Lett.*, vol. 10, pp. 1271–1275, 2010.

[90] S. Bertolazzi, J. Brivio, and A. Kis, "Stretching and breaking of ultrathin MoS_2," *ACS Nano*, vol. 5, pp. 9703–9709, 2011.

[91] F. Ding, H. Ji, Y. Chen, A. Herklotz, K. Dorr, Y. Mei, A. Rastelli, and O. G. Schmidt, "Stretchable graphene: A close look at fundamental parameters through biaxial straining," *Nano Lett.*, vol. 10, pp. 3453–3458, 2010.

[92] Y. Y. Hui, X. Liu, W. Jie, N. Y. Chan, J. Hao, Y.-T. Hsu, L.-J. Li, W. Guo, and S. P. Lau, "Exceptional tunability of band energy in a compressively strained trilayer MoS_2 sheet," *ACS Nano*, vol. 7, pp. 7126–7131, 2013.

[93] W. Wu, L. Wang, Y. Li, F. Zhang, L. Lin, S. Niu, D. Chenet, X. Zhang, Y. Hao, T. F. Heinz, J. Hone, and Z. L. Wang, "Piezoelectricity of single-atomic-layer MoS_2 for energy conversion and piezotronics," *Nature*, vol. 514, pp. 470–474, 2014.

[94] J.-K. Lee, S. Yamazaki, H. Yun, J. Park, G. P. Kennedy, G.-T. Kim, O. Pietzsch, R. Wiesendanger, S. Lee, S. Hong, U. Dettlaff-Weglikowska, and S. Roth, "Modification of electrical properties of graphene by substrate-induced nanomodulation," *Nano Lett.*, vol. 13, pp. 3494–3500, 2013.

[95] Z. H. Ni, T. Yu, Y. H. Lu, Y. Y. Wang, Y. P. Feng, and Z. X. Shen, "Uniaxial strain on graphene: Raman spectroscopy study and band-gap opening," *ACS Nano*, vol. 2, pp. 2301–2305, 2008.

[96] H. Peelaers and C. G. Van de Walle, "Effects of strain on band structure and effective masses in MoS_2," *Phys. Rev. B*, vol. 86, p. 241401, 2012.

[97] W. S. Yun, S. W. Han, S. C. Hong, I. G. Kim, and J. D. Lee, "Thickness and strain effects on electronic structures of transition metal dichalcogenides: 2H$-MX_2$ semiconductors (M= Mo, W; X= S, Se, Te)," *Phys. Rev. B*, vol. 85, p. 033305, 2012.

[98] W. Kohn, A. D. Becke, and R. G. Parr, "Density functional theory of electronic structure," *J. Phys. Chem.*, vol. 100, no. 31, pp. 12974–12980, 1996.

[99] S. Cottenier, "Density functional theory and the family of (L)APW-methods: a step-by-step introduction," 2004.

[100] P. Hohenberg and W. Kohn, "Inhomogeneous electron GaS," *Phys. Rev.*, vol. 136, pp. 864–871, 1964.

[101] W. Kohn and L. J. Sham, "Self-consistent equations including exchange and correlation effects," *Phys. Rev.*, vol. 140, pp. 1133–1138, 1965.

[102] J. P. Perdew and W. Yue, "Accurate and simple density functional for the electronic exchange energy: Generalized gradient approximation," *Phys. Rev. B*, vol. 33, pp. 8800–8802, Jun 1986.

[103] J. P. Perdew, K. Burke, and M. Ernzerhof, "Generalized gradient approximation made simple," *Phys. Rev. Lett.*, vol. 77, pp. 3865–3868, Oct 1996.

[104] J. Hubbard and B. H. Flowers, "Electron correlations in narrow energy bands," *Proceedings of the Royal Society of London. Series A. Mathematical and Physical Sciences*, vol. 276, no. 1365, pp. 238–257, 1963.

[105] W. Xiong, C. Xia, T. Wang, J. Du, Y. Peng, X. Zhao, and Y. Jia, "Tuning electronic structures of the stanene monolayer via defects and transition-metal-embedding: Spin-orbit coupling," *Phys. Chem. Chem. Phys.*, vol. 18, pp. 28759–28766, 2016.

[106] S. Chintalapati, L. Shen, Q. Xiong, and Y. P. Feng, "Magnetism in phosphorene: Interplay between vacancy and strain," *Appl. Phys. Lett.*, vol. 107, no. 7, p. 072401, 2015.

[107] D. Gao, S. Shi, K. Tao, B. Xia, and D. Xue, "Tunable ferromagnetic ordering in MoS_2 nanosheets with fluorine adsorption," *Nanoscale*, vol. 7, pp. 4211–4216, 2015.

[108] A. Ramasubramaniam and D. Naveh, "Mn-doped monolayer MoS_2: An atomically thin dilute magnetic semiconductor," *Phys. Rev. B*, vol. 87, p. 195201, 2013.

[109] Y. Ding and Y. Wang, "Structural, electronic, and magnetic properties of adatom adsorptions on black and blue phosphorene: A first-principles study.," *Phys. Chem. Chem. Phys.*, vol. 119, pp. 10610–10622, 2015.

[110] S. R. Naqvi, T. Hussain, W. Luo, and R. Ahuja, "Exploring doping characteristics of various adatoms on single-layer stanene.," *Phys. Chem. Chem. Phys.*, vol. 121, pp. 7667–7676, 2017.

[111] A. A. Peyghan and M. Moradi, "DFT study of ozone dissociation on BC_3 graphene with stone–wales defects," *J. Molecular Model.*, vol. 20, no. 1, p. 2071, 2014.

[112] A. A. Peyghan and M. Noei, "Fluorination of BC_3 danotubes: DFT dtudies," *J. Molecular Model.*, vol. 19, pp. 3941–3946, Sep 2013.

[113] C. Chowdhury and A. Datta, "Exotic physics and chemistry of two-dimensional phosphorus: Phosphorene," *J. Phys. Chem. Lett.*, vol. 8, pp. 2909–2916, 2016.

[114] Y. J. Kwon, S. Y. Kang, P. Wu, Y. Peng, S. S. Kim, and H. W. Kim, "Selective improvement of NO_2 gas sensing behavior in SnO_2 nanowires by ion-beam irradiation," *ACS Applied Materials and Interfaces*, vol. 8, pp. 13646–13658, 2016.

[115] C. J. S. Yang and S.-H. Wei, "Gas sensing in 2D materials," *Applied Physics Reviews*, vol. 4, no. 2, p. 021304, 2017.

[116] O. Leenaerts, B. Partoens, and F. M. Peeters, "Adsorption of H_2O, NH_3, co, NO_2, and NO on graphene: A first-principles study," *Phys. Rev. B*, vol. 77, p. 125416, Mar 2008.

[117] O. Leenaerts, B. Partoens, and F. Peeters, "Adsorption of small molecules on graphene," *Microelectronics Journal*, vol. 40, no. 4, pp. 860–862, 2009. European Nano Systems (ENS 2007) International Conference on Superlattices, Nanostructures and Nanodevices (ICSNN 2008).

[118] J. Low, J. Yu, and W. Ho, "Graphene-based photocatalysts for CO_2 reduction to solar fuel," *J. Phys. Chem. Lett.*, vol. 6, pp. 4244–4251, 2015.

[119] S. Yun, W.-E. L. H. Lee, and H. S. Park, "Multiscale textured, ultralight graphene monoliths for enhanced CO_2 and SO_2 adsorption capacity," *Fuel*, vol. 174, pp. 36–42, 2016.

[120] B. Li, K. Fan, Y. L. X. Ma, T. Chen, Z. Cheng, X. Wang, J. Jiang, and X. Liu, "Graphene-based porous materials with tunable surface area and CO_2 adsorption properties synthesized by fluorine displacement reaction with various diamines," *Journal of Colloid and Interface Science*, vol. 478, pp. 36–45, 2016.

[121] J. Low, B. Cheng, J. Yu, and M. Jaroniec, "Carbon-based two-dimensional layered materials for photocatalytic CO_2 reduction to solar fuels," *Energy Storage Materials*, vol. 3, pp. 24–35, 2016.

[122] T. P. Kaloni, G. Schreckenbach, and M. S. Freund, "Large enhancement and tunable band gap in silicene by small organic molecule adsorption," *J. Phys. Chem. C*, vol. 118, pp. 23361–23367, 2014.

[123] R. Chandiramouli and V. Nagarajan, "Adsorption studies of NH_3 molecules on functionalized germanene nanosheet - A DFT study," *Chem. Phys. Lett.*, vol. 665, pp. 22–30, 2016.

[124] J.-W. Feng, Y.-J. Liu, H.-X. Wang, J.-X. Zhao, Q.-H. Cai, and X.-Z. Wang, "Gas adsorption on silicene: A theoretical study," *Computational Materials Science*, vol. 87, pp. 218–226, 2014.

[125] M.-Y. Chang, C.-S. Wu, Y.-F. Chen, B.-Z. Hsieh, W.-Y. Huang, K.-S. Ho, T.-H. Hsieh, and Y.-K. Han, "Polymer solar cells incorporating one-dimensional polyaniline nanotubes," *Organic Electronic.*, vol. 9, no. 6, pp. 1136–1139, 2008.

[126] M. M. Alam, J. Wang, Y. Guo, S. P. Lee, and H.-R. Tseng, "Electrolyte-gated transistors based on conducting polymer nanowire junction arrays," *J. Phys. Chem. B*, vol. 109, no. 26, pp. 12777–12784, 2005.

[127] X. Jiantie, M. Javeed, D. Yuhai, D. Shixue, L. Feng, D. Liming, and B. J. Beom, "2D frameworks of C_2N and C_3N as new anode materials for lithium-Ion batteries," *Adv. Mater.*, vol. 29, no. 34, p. 1702007.

[128] S. Mizuno, M. Fujita, and K. Nakao, "Electronic states of graphitic heterocompounds of carbon, boron and nitrogen," *Synthetic Metals*, vol. 71, no. 1, pp. 1869–1870, 1995.

[129] Q. Hu, Q. Wu, H. Wang, J. He, and G. Zhang, "First-Principles studies of structural and electronic properties of layered C_3N phases," *physica status solidi (b)*, vol. 249, no. 4, pp. 784–788, 2011.

[130] S. Yang, W. Li, C. Ye, G. Wang, H. Tian, C. Zhu, P. He, G. Ding, X. Xie, Y. Liu, Y. Lifshitz, S. T. Lee, Z. Kang, and M. Jiang, "C_3N–A 2D crystalline, hole-free, tunable narrow bandgap semiconductor with ferromagnetic properties," *Adv. Mater.*, vol. 29, no. 16, p. 1605625, 2016.

[131] H. J. Xiang, B. Huang, Z. Y. Li, S.-H. Wei, J. L. Yang, and X. G. Gong, "Ordered semiconducting nitrogen-graphene alloys," *Phys. Rev. X*, vol. 2, p. 011003, 2012.

[132] M. Pashangpour and A. A. Peyghan, "Adsorption of carbon monoxide on the pristine, b- and al-doped C_3N nanosheets," *J. Molecular Model.*, vol. 21, no. 5, p. 116, 2015.

[133] M. B. Tagani, "Electrical and mechanical properties of a fully hydrogenated two-dimensional polyaniline sheet," *Comput. Mater. Sci.*, vol. 153, pp. 126–133, 2018.

[134] T. Ozaki, "Variationally optimized atomic orbitals for large-scale electronic structures," *Phys. Rev. B*, vol. 67, p. 155108, 2003.

[135] T. Ozaki and H. Kino, "Numerical atomic basis orbitals from h to kr," *Phys. Rev. B*, vol. 69, p. 195113, 2004.

[136] J. P. Perdew, K. Burke, and M. Ernzerhof, "Generalized gradient approximation made simple," *Phys. Rev. Lett.*, vol. 77, pp. 3865–3868, 1996.

[137] N. Troullier and J. Martins, "Efficient pseudopotentials for plane-wave calculations," *Phys. Rev. B*, vol. 43, pp. 1993–2006, Jan 1991.

[138] H. J. Monkhorst and J. D. Pack, "Special points for brillouin-zone integrations," *Phys. Rev. B*, vol. 13, pp. 5188–5192, 1976.

[139] R. S. Mulliken, "Electronic Population Analysis on LCAO-MO Molecular Wave Functions. IV. Bonding and Antibonding in LCAO and Valence Bond Theories," *J. Chem. Phys.*, vol. 23, no. 12, pp. 2343–2346, 1955.

[140] P. Giannozzi, S. Baroni, N. Bonini, M. Calandra, R. Car, C. Cavazzoni, D. Ceresoli, G. L. Chiarotti, M. Cococcioni, I. Dabo, A. D. Corso, S. de Gironcoli, and et al., "QUANTUM ESPRESSO: A modular and open-source software project for quantum simulations of materials," *J. Phys.: Condens. Matter*, vol. 21, no. 39, p. 395502, 2009.

[141] J. M. Soler, E. Artacho, J. D. Gale, A. Garcia, J. Junquera, P. Ordejon, and D. Sanchez-Portal, "The SIESTA method for ab initio order-n materials simulation," *J. Phys.: Condens. Matter*, vol. 14, no. 11, p. 2745, 2002.

[142] T. Bucko, J. Hafner, S. LebÃÍgue, and J. G. Angyan, "Improved description of the structure of molecular and layered crystals: Ab initio DFT calculations with van der waals corrections," *J. Phys. Chem. A*, vol. 114, no. 43, pp. 11814–11824, 2010.

[143] H. Jonsson, G. Mills, and K. W. Jacobsen, "Nudged elastic band method for finding minimum energy paths of transitions," *World Scientific*, pp. 385–404, 1998.

[144] J. Tersoff and D. R. Hamann, "Theory and application for the scanning tunneling microscope," *Phys. Rev. Lett.*, vol. 50, pp. 1998–2001, 1983.

[145] I. Horcas, R. Fernandez, J. M. G.-R. J. Colchero, J. Gomez-Herrero, and A. M. Baro, "WSxM: A software for scanning probe microscopy and a tool for nanotechnology," *Rev. Sci. Inst.*, vol. 78, no. 1, p. 013705, 2007.

[146] H. A. Jahn and E. Teller, "Stability of polyatomic molecules in degenerate electronic states - i—orbital degeneracy," *Proc. Royal Soc. London A: Mathematical, Physical and Engineering Sciences*, vol. 161, no. 905, pp. 220–235, 1937.

[147] M. Z. Hossain, J. E. Johns, K. H. Bevan, H. J. Karmel, Y. T. Liang, S. Yoshimoto, K. Mukai, T. Koitaya, J. Yoshinobu, M. Kawai, A. M. Lear, L. L. Kesmodel, S. L. Tait, and M. C. Hersam., "Chemically homogeneous and thermally reversible oxidation of epitaxial graphene.," *Nature Chemistry*, vol. 4, pp. 305–309, 2012.

[148] H. sahin, M. Topsakal, and S. Ciraci, "Structures of fluorinated graphene and their signatures," *Phys. Rev. B*, vol. 83, p. 115432, Mar 2011.

[149] E. J. Duplock, M. Scheffler, Lindan, and J. D. Philip, "Hallmark of perfect graphene," *Phys. Rev. Lett.*, vol. 92, p. 225502, 2004.

[150] D. W. Boukhvalov, M. I. Katsnelson, and A. I. Lichtenstein, "Hydrogen on graphene: Electronic structure, total energy, structural distortions, magnetism from first-principles calculations," *Phys. Rev. B*, vol. 77, p. 035427, 2008.

[151] S. Ryu, M. Y. Han, J. Maultzsch, T. F. Heinz, P. Kim, M. L. Steigerwald, and L. E. Brus, "Reversible basal plane hydrogenation of graphene," *Nano Lett.*, vol. 8, pp. 4597–4602, 2008.

[152] D. Haberer, D. V. Vyalikh, S. Taioli, B. Dora, M. Farjam, J. Fink, D. Marchenko, T. Pichler, K. Ziegler, S. Simonucci, M. S. Dresselhaus, M. Knupfer, B. BÃijchner, and A. GrÃijneis, "Tunable band gap in hydrogenated quasi-free-standing graphene," *Nano Lett.*, vol. 10, no. 9, pp. 3360–3366, 2010.

[153] Z. Luo, j. Shang, s. Lim, D. Li, Q. Xiong, Z. Shen, J. Lin, and T. Yu, "Modulating the electronic structures of graphene by controllable hydrogenation," *Appl. Phys. Lett.*, vol. 97, no. 23, p. 233111, 2010.

[154] D. C. Elias, R. R. Nair, T. M. G. Mohiuddin, S. V. Morozov, P. Blake, M. P. Halsall, A. C. Ferrari, D. W. Boukhvalov, M. I. Katsnelson, A. K. Geim, and K. S. Novoselov, "Control of graphene's properties by reversible hydrogenation: Evidence for graphane," *Science*, vol. 323, no. 5914, pp. 610–613, 2009.

[155] J. Zhou, Q. Wang, Q. Sun, X. S. Chen, Y. Kawazoe, and P. Jena, "Ferromagnetism in semihydrogenated graphene sheet.," *Nano Lett.*, vol. 9, pp. 3867–3870, 2009.

[156] I. Žutić, J. Fabian, and S. D. Sarma, "Spintronics: Fundamentals and applications," *Rev. Mod. Phys.*, vol. 76, pp. 323–410, 2004.

[157] M. Gmitra, D. Kochan, and J. Fabian, "Spin-orbit coupling in hydrogenated graphene," *Phys. Rev. Lett.*, vol. 110, p. 246602, 2013.

[158] O. V. Yazyev and L. Helm, "Defect-induced magnetism in graphene," *Phys. Rev. B*, vol. 75, p. 125408, 2007.

[159] O. V. Yazyev and M. I. Katsnelson, "Magnetic correlations at graphene edges: Basis for novel spintronics devices," *Phys. Rev. Lett.*, vol. 100, p. 047209, 2008.

[160] O. V. Yazyev, "Magnetism in disordered graphene and irradiated graphite," *Phys. Rev. Lett.*, vol. 101, p. 037203, 2008.

[161] K. M. McCreary, A. G. Swartz, W. Han, J. Fabian, and R. K. Kawakami, "Magnetic moment formation in graphene detected by scattering of pure spin currents," *Phys. Rev. Lett.*, vol. 109, p. 186604, 2012.

[162] Q. Tang, Z. Zhou, and Z. Chen, "Graphene-related nanomaterials: tuning properties by functionalization," *Nanoscale*, vol. 5, pp. 4541–4583, 2013.

[163] J. Zhou, M. M. Wu, X. Zhou, and Q. Sun, "Tuning electronic and magnetic properties of graphene by surface modification.," *Appl. Phys. Lett.*, vol. 95, no. 10, p. 103108, 2009.

[164] Z. Shi, X. Zhao, and X. Huang, "First principles investigation on the stability, magnetic and electronic properties of the fully and partially hydrogenated bn nanoribbons in different conformers," *J. Mater. Chem. C*, vol. 1, pp. 6890–6898, 2013.

[165] M. C. Payne, M. P. Teter, D. C. Allan, T. A. Arias, and J. D. Joannopoulos, "Iterative minimization techniques for ab initio total-energy calculations: molecular dynamics and conjugate gradients," *Rev. Mod. Phys.*, vol. 64, pp. 1045–1097, 1992.

[166] L.-C. Xu, R.-Z. Wang, M.-S. Miao, X.-L. Wei, Y.-P. Chen, H. Yan, W.-M. Lau, L.-M. Liu, and Y.-M. Ma, "Two dimensional dirac carbon allotropes from graphene," *Nanoscale*, vol. 6, pp. 1113–1118, 2014.

[167] K. T. Chan, J. B. Neaton, and M. L. Cohen, "First-principles study of metal adatom adsorption on graphene," *Phys. Rev. B*, vol. 77, p. 235430, 2008.

[168] H. Sahin and F. M. Peeters, "Adsorption of Alkali, Alkaline-Earth, and 3d transition metal atoms on silicene," *Phys. Rev. B*, vol. 87, p. 085423, 2013.

[169] Q. Pang, L. Li, L.-L. Zhang, C. Zhang, and Y.-L. Song, "Functionalization of germanene by metal atoms adsorption: A first-principles study," *Can. J. Phys.*, vol. 93, no. 11, pp. 1310–1318, 2015.

[170] Y. Kadioglu, F. Ersan, G. Gokoglu, O. U. Akturk, and E. Akturk, "Adsorption of Alkali, Alkaline-Earth metal atoms on stanene: A first-principles study," *Mater. Chem. Phys.*, vol. 180, pp. 326–331, 2016.

[171] Y. Li, C. Xia, J. Du, W. Xiong, X. Li, and S. Wei, "Influences of the adsorption of different elements on the electronic structures of a tin sulfide monolayer," *Phys. Chem. Chem. Phys.*, vol. 19, pp. 5423–5429, 2017.

[172] M. Lalitha, S. S. Mahadevan, and S. Lakshmipathi, "Improved lithium adsorption in boron- and nitrogen-substituted graphene derivatives," *J. Mater. Sci.*, vol. 52, pp. 815–831, Jan 2017.

[173] X. Wang, X. Jiang, E. Sharman, L. Yang, X. Li, G. Zhang, J. Zhao, Y. Luo, and J. Jiang, "Isolating hydrogen from oxygen in photocatalytic water splitting with a carbon-quantum-dot/carbon-nitride hybrid," *J. Mater. Chem. A*, vol. 7, pp. 6143–6148, 2019.

[174] M. Sun, S. Wang, Y. Du, J. Yu, and W. Tang, "Transition metal doped arsenene: A first-principles study," *Appl. Surf. Sci.*, vol. 389, pp. 594–600, 2016.

[175] M. Sun, Q. Ren, S. Wang, Y. Zhang, Y. Du, J. Yu, and W. Tang, "Magnetism in transition-metal-doped germanene: A first-principles study," *Comput. Mater. Sci.*, vol. 118, pp. 112–116, 2016.

[176] Y. C. Cheng, Z. Y. Zhu, W. B. Mi, Z. B. Guo, and U. Schwingenschlögl, "Prediction of two-dimensional diluted magnetic semiconductors: Doped monolayer MoS_2 systems," *Phys. Rev. B*, vol. 87, p. 100401, Mar 2013.

[177] O. U. Akturk and M. Tomak, "Lithium and antimony adsorbed on graphene studied by first-principles calculations," *Appl. Surf. Sci.*, vol. 258, no. 2, pp. 800–805, 2011.

[178] S. Gao, Z. Ren, L. Wan, J. Zheng, P. Guo, and Y. Zhou, "Density functional theory prediction for diffusion of lithium on boron-doped graphene surface," *Appl. Surf. Sci.*, vol. 257, no. 17, pp. 7443–7446, 2011.

[179] J. D. Roy-Mayhew, D. J. Bozym, C. Punckt, and I. A. Aksay, "Functionalized graphene as a catalytic counter electrode in dye-sensitized solar cells," *ACS Nano*, vol. 4, no. 10, pp. 6203–6211, 2010.

[180] M. D. Ganji, N. Sharifi, M. Ardjmand, and M. G. Ahangari, "Pt-decorated graphene as superior media for H_2S adsorption: A first-principles study," *Appl. Surf. Sci.*, vol. 261, pp. 697–704, 2012.

[181] Y. Lee, S. Lee, Y. Hwang, and Y.-C. Chung, "Modulating magnetic characteristics of pt embedded graphene by gas adsorption (N_2, O_2, NO_2, SO_2)," *Appl. Surf. Sci.*, vol. 289, pp. 445–449, 2014.

[182] I. Khan and J. Hong, "Manipulation of magnetic state in phosphorene layer by non-magnetic impurity doping," *New J. Phys.*, vol. 17, p. 023056, feb 2015.

[183] L. Seixas, A. Carvalho, and A. H. C. Neto, "Atomically thin dilute magnetism in co-doped phosphorene," *Phys. Rev. B*, vol. 91, p. 155138, Apr 2015.

[184] A. Ramasubramaniam and D. Naveh, "Mn-doped monolayer MoS_2: An atomically thin dilute magnetic semiconductor," *Phys. Rev. B*, vol. 87, p. 195201, May 2013.

[185] Z. Zheng, X. Wang, and W. Mi, "Tunable electronic structure in stained two dimensional van der waals g-C_2N/XSe_2 (X = Mo, W) heterostructures," *Physica E: Low-dimensional Systems and Nanostructures*, vol. 94, pp. 148 – 152, 2017.

[186] R. Kumar, D. Das, and A. K. Singh, "C_2N/WS_2 van der waals type-ii heterostructure as a promising water splitting photocatalyst," *J. Catalysis*, vol. 359, pp. 143–150, 2018.

[187] M. A. Kishore, A. O. Sjastad, and P. Ravindran, "Influence of hydrogen and halogen adsorption on the photocatalytic water splitting activity of C_2N monolayer: A first-principles study," *Carbon*, vol. 141, pp. 50–58, 2019.

[188] L.-B. Shi, Y.-Y. Zhang, X.-M. Xiu, and H.-K. Dong, "Structural characteristics and strain behavior of two-dimensional C_3N: First principles calculations," *Carbon*, vol. 134, pp. 103–111, 2018.

Curriculum vitae

Curriculum Vitae

Personal Information

Surname: **Asadollah**
Name: **Bafekry**
Personal email: bafekry.asad@gmail.com; Asaollah.Bafekry@uantwerpen.be

Chronological overview

PhD : in Condensed matter Physics (*2015-2020*)

University of Guilan & University of Antwerp Antwerp

Joint PhD. in Condensed Matter Physics

Department of Physics, University of Guilan, Rasht, Iran

Department of Physics, University of Antwerp, Groenenborgerlaan 171, Antwerp, Belgium

MSc : in Applied Physics (*2005-2008*)

Department of Physics, Amirkabir University of Technology, Tehran, Iran

BSc : in Condensed matter Physics (*2000-2004*)

Department of Physics, University of Guilan, Rasht, Iran

Research fields of interests

- Computational and experimental Nanophysics
- Condensed Matter Physics
- Two-dimensional Materials
- Electonic, Optical, magnetic and Transport properties
- Tuning of materials via defect engeering and external fields
- Modification of materials via functionalization and impuritiy
- Hetrostructures

Programming Skills

- Experience with Parallel programming, high-performance computing, UNIX/Linux, Windows NT/XP, Unix shell scripting, Data Explorer. Parallel programming and Libraries : MPI, OPENMP, (Sca) LAPACK, BLACS, ACML.
- Text processors : Microsoft Office package, LaTeX.
- Graphics software : Good experience on Plotting packages: Gnuplot, XMGrace, VESTA, XCrysDen , Inkscape, Photoshop.

Special Packages

- **OpenMX, Quantum Espresso, SIESTA**
  Familiar with using Atomic simulation packages including ;
- **BoltzTraP , ABINIT , VASP , Wannier90**

Publications

1- Exploring the Emerging of Novel Electronic and Magnetic Properties with Adatom Adsorption, Functionalizations, Electric field, Charging and Strain,
Asadollah Bafekry, Saber Farjami Shayesteh and F. M. Peeters,
Journal of Physical Chemistry C. 123, 19, 12485-12499 , 2019. **(Impact factor: 4.309)**

2- Tuning the electronic and magnetic properties of antimonene nanosheets via point defects and external fields: first-principles calculations,
Asadollah Bafekry, Mitra Ghergherehchi, Saber Farjami Shayesteh,
Journal of Physical Chemistry Chemical Physics, 21 (20), 10552-10566 , 2019. **(Impact factor: 3.567)**

3- Introducing Novel Electronic and Magnetic Properties in C3N Nanosheet by Defect Engineering and Atom Substitution,
Asadollah Bafekry, Saber Farjami Shayesteh and F. M. Peeters.
Journal of Physical Chemistry Chemical Physics, 21 (37), 21070-21083 , 2019. **(Impact factor: 3.567)**

4- Exploiting the novel electronic and magnetic structure of C3N via functionalization and conformation,
Asadollah Bafekry, Catherine Stampfl, Saber Farjami Shayesteh and F. M. Peeters.
Journal of Advanced Electronic Materials, 1900459, 2019. **(Impact factor: 6.312)**

5- Adsorption of molecules on the C3N nanosheet: A first-principle calculations,
Asadollah Bafekry, Mitra Ghergherehchi, Saber Farjami Shayesteh and F. M. Peeters.
Journal of Chemical Physics, 562, 110442, 2019.

6- Band gap and magnetism engineering in Dirac half-metallic of Na2C nanosheet via layer thickness, strain and point defects,
Asadollah Bafekry, Bohayra Mortazavi, F. M. Peeters.
Journal of Magnetism and Magnetic Materials, 491, 165565 , 2019. **(Impact factor:3.046)**

7- Tuning the band gap and introducing magnetism into BC3 nanosheet via stain/defect engineering and adatom/molecule adsorption,
Asadollah Bafekry, Mitra Ghergherehchi, Saber Farjami Shayesteh and F. M. Peeters.
Journal of Applied Physics, 126 (14), 144304, 2019. **(Impact factor: 2.328)**

8- Exploring of novel electronic and magnetic properties in the C2N nanosheet via defect/strain engineering and impurity of atom,
Asadollah Bafekry, Catherine Stampfl, Mitra Ghergherehchi, Saber Farjami Shayesteh.
Journal of CARBON, 157, 371-384 (2020). **(Impact factor: 7.466)**

9- Tunable electronic and magnetic properties of graphene/carbon-nitride van der Waals heterostructures,
Asadollah Bafekry, Berna Akgenc, S. Farjami Shayesteh and Bohayra Mortazavi, Journal of
Journal of Applied Surface Science, 144450, 2019. **(Impact factor: 5.155)**

10- A first-principles study of C3N nanostructures: Control and engineering of the electronic and magnetic properties of nanosheets, tubes and ribbons,
Asadollah Bafekry, Catherine Stampfl and Saber Farjami Shayesteh,
Journal of ChemPhysChem, 2020, 21, 164. **(Impact factor: 3.077)**

11- Two-Dimensional Carbon Nitride (2DCN) Nanosheets: Tuning of Novel Electronic and Magnetic Properties by Hydrogenation, Atom Substitution and Defect Engineering,
Asadollah Bafekry and F. M. Peeters,
Journal of Applied Physics, 126 (21), 215104, 2019. **(Impact factor: 2.328)**

12- Gaphen-like BC6N nanosheet: Tuning of the electronic and magnetic properties via layer thickness, external fields, typical defects and adsorption/substitution of atoms ,
Asadollah Bafekry,
Journal of Physica E: Low-dimensional Systems and Nanostructures, 113850, 2019. **(Impact factor: 3.176)**

13- Dirac half-metallicity of Thin PdCl3 Nanosheets: Investigation of the Effects of External Fields, Surface Adsorption and Defect Engineering on the Electronic and Magnetic Properties,
Asadollah Bafekry, Catherine Stampfl, F. M. Peeters.
Journal of Nature scientific reports, 213 (2020). (Impact factor: 4.122)

14- Control of C3N4 and C4N3 carbon nitride nanosheets' electronic and magnetic properties through embedded atoms,
Asadollah Bafekry, Berna Akgenc, Catherine Stampfl, Mitra Ghergherehchi,
Journal of Physical Chemistry Chemical Physics, 2020,22, 2249-2261. **(Impact factor: 3.567)**

15- Tuning the electronic properties of graphene-graphitic carbon nitride heterostructures and heterojunctions by using electric field,
Asadollah Bafekry, and Mehdi Neek-Amal,
Journal of Physical Review B. , 2020 101 (8), 085417.

16**-** Embedding of atoms into the holey site of the C6N6 and C6N8 porous carbon nitride monolayers with tunable electronic properties,
Asadollah Bafekry, Catherine Stampfl, Berna Akgenc, *Bohayra Mortazavi,* Mitra Ghergherehchi and Ch. V Neguyen,
Journal of Physical Chemistry Chemical Physics, 2020 22 (11), 6418-6433.

17**-** ZnN and ZnP as novel graphene-like materials with high Li-ion storage capacities,
Bohayra Mortazavi, Asadollah Bafekry, Masoud Shahrokhi, Timon Rabczuk and Xiaoying Zhuang,
Journal of Material Today, 16, 2020, 100392.

18- Van der Waals heterostructures of layered Janus transition-metal dichalcogenides (MoS2 and Janus MoSSe) on graphitic boron-carbon-nitride (BC3, C3N, C3N4 and C4N3) nanosheets: A First-Principles study,
Asadollah Bafekry, Mehmet Yagmurcukardes, Berna Akgenc, Mitra Ghergherehchi and Ch. V Neguyen
Journal of Physics D: Applied Physics , 2020 **doi:10.1088/1361-6463/ab876c**

19- Strain, electric-field and functionalization induced widely tunable electronic properties in MoS2/BC3, /C3N and /C3N4 van der Waals heterostructures,
Asadollah Bafekry, Catherine Stampfl and Mitra Ghergherehchi,
Journal of Nanotechnology, 2020 **doi:/10.1088/1361-6528/ab884e**

20- Strain and electric field tuning of semi-metallic character WCrCO2 MXenes with dual narrow band gap,
Asadollah Bafekry, Berna Akgenc, Mitra Ghergherehchi and F. M. Peeters,
Journal of Physics: Condensed Matter, 2020, doi:10.1088/1361-648X/ab8e88

21- Two-dimensional graphitic carbon nitrides: Strain-tunable ferromagnetic ordering
A Bafekry, M Neek-Amal, FM Peeters,
Journal of Physical Review B, 2020**, 101 (16), 101, 165407**

22- The electronic, optical and thermoelectric properties of monolayer PbTe and the tunability of the electronic structure by external fields and defects
A. Bafekry, C. Stampfl, Mitra Ghergherehchi, and F. M. Peeters,
Physica Status Solidi b – Basic Solid State Physics, 2020, doi:10.1002/pssb.202000182

Manuscripts under review:

23- An Unusual Strong Electronic Energy Band in Ti2CO2 MXenes Induced by Oxygen Vacancies and Tunable Band gap and magnetism with electric field and Strain ,
Asadollah Bafekry, Berna Akgenc and Mitra Ghergherehchi and Ch. V. Neguyen
Journal of Physcial Chemisty C, 2020

24- Tunable the electronic properties of the layered mineral Pt2HgSe3 (jacutingaite),
Asadollah Bafekry, Catherine Stampfl, Mitra Ghergherehchi and Mehmet yagmurcukardes,
Journal of Physical Review B, 2020

25- Graphene hetero-multilayer on layered platinum mineral Jacutingaite (Pt2HgSe3): Van der Waals heterostructures with novel optoelectronic and thermoelectric performances
A. Bafekry, M. M. Obeid, Chuong V. Nguye, M. Bagheri Tagani, M. Ghergherehchi,
Journal of Materials Chemistry A, 2020

*26-*Monolayer and Bilayer Zinc antimonide (ZnSb) Honeycomb Structures : A First-Principles Study,
A. Bafekry, M. Yagmurcukardes, M. Shahrokhi, M. Ghergherehchi and D. Kim,
Journal of Physical Review B, 2020

27- Surface Fucntionalization of monolayer honeycomb structure of zinc antimonide (ZnSb): A First-principles calculations,
Asadollah Bafekry, M. Shahrokhi, Mehmet Yagmurcukardes, Berna Akgenc, Mitra Ghergherehchi,
Journal of Physical Review B, 2020

28- Monolayer and bilayer of B-doped C3N carbon nitride: Control the electronic, optic and mechanical properties by atomic doping as well as electric field and strain
Asadollah Bafekry, M. M. Obeid, Chuong V. Nguye and M. Ghergherehchi,
Journal of Applied Surface Science, 2020

29- Monolayer of B doped C3N and bilayer of BN codoped graphene: Tuning the electro-optic properties by atomic doping as well as electric field and strain
Asadollah Bafekry, Mehmet Yagmurkardesh, Masoud Shahrokhi, and Mitra Ghergherehchi
Journal of CARBON, 2020

30- Controlling the band gap of B and N co-doped graphene bilayers by an electrical gating
Asadollah Bafekry, Catherine Stampfl
Journal of Physical Review B, 2020

31 **-** Atomic embedding and strain driven electronic phase transitions in porous carbon nitride monolayers C6N6 and C6N8,
Asadollah Bafekry, Chuong V. Nguye, Abbas Goudarzi, Mitra Ghergherehchi,
Journal of Physica E: Low-dimensional Systems and Nanostructures, 2020

32- Tight-binding model for Double Dirac nodal lines in Cu_2Si monolayer,
Asadollah Bafekry, Berna Akgenc , Mohamad Nakhaee and F. M. Peeters,
Journal of Computational material Science*,* 2020

Manuscripts under Working and preparation:

33- Bismuth based novel two-dimensional honeycomb-like Group IV-Bi monolayers: A first-principles calculations
Asadollah Bafekry, Fatih Ersan, Berna Akgenc, and Mehmet Yagmurcukardes

34- First-principles study of the electronic properties of two-dimensional Silicon Bismotide (SiBi) with a honeycomb-like lattice
Asadollah Bafekry, Fazel Shojaei, Mitra Ghergherehchi,

35- Novel two-dimensional honeycomb-like of XBi (X=Si, Ge, Sn) monolayers: A first-principles calculations
Asadollah Bafekry, FazelShojaei, Masoud Shahrokhi , Mitra Ghergherehchi,

36- Heterostructures of doped graphene on graphene and graphitic boron-carbon-nitride (BC3, C3N and BN) monolayers: Effects of electric field and strain
Asadollah Bafekry, M. M. Obeid, Chuong V. Nguye and M. Ghergherehchi,

Reviewer for international journals

- **The Journal of Physical Chemistry Letters**
- **Applied Physics Letters**
- **Material Chemistry C**
- **Journal of Applied Physic**
- **Physica E: Low-dimensional Systems and Nanostructures**
- **Physical Chemistry Chemical Physics**
- **Diamond & Related Materials**
- **Chemical Physics**
- **Chemical Intermediates**

Advanced Courses Passed

- Many-body quantum theory condensed matter
- Advanced Statistical Mechanics
- Advanced Quantum Mechanics (1&2)
- Electrodynamics
- Advanced Solid State Physics (1&2)
- Computational Physics

Work experience and teaching

- Topics in General physics Lab. course (1,2), University of Guilan. Springs 2016–17
- Topics in Mechanical Physics, Physics of Electricity, Department of Physics, University of Islamic Azad, Rasht Branch. Springs 2015–to the present
- Topics in Mechanical Physics, Electromagnetism Physics, Electronic Physics, Thermal physics, Department of Physics, University of Applied Sciences and Technology Springs 2012–to the present